Faculty of Geosciences

Department of Physical Geography

Mass Movement Hazard in a Changing Climate:

Spatial and Temporal Analysis of Hydrological Triggering at the Rest and Be Thankful Pass, Scotland

Author:
Niels Roland Klaver

Supervisors:
Dr. L.P.H. van Beek
Dr. K.A.P. Barkwith
Prof. Dr. S.M. de Jong

December, 2018

Utrecht University

British Geological Survey
NATURAL ENVIRONMENT RESEARCH COUNCIL

Abstract

The Rest and be Thankful pass is one of the most active sites of the UK considering mass movement. The pass has experienced frequent closure in the past years and large investments are made to secure accessibility. Alterations of the hydrological cycle through climate change will have strong consequences on the frequency, severity and nature of mass movement. Naturally, this has implications for adaptation and mitigation measures to cope with future trends and the corresponding costs. To understand future hazard, the main spatial and temporal implications for mass movement through climate change are addressed. A hydrological threshold, based on the daily precipitation and antecedent precipitation index, is derived from precipitation data of historical mass movement events. This threshold is applied to hydrological forecasts from the United Kingdom Climate Projections to determine future mass movement frequency. Additionally, it is addressed whether daily or antecedent precipitation is determent in various hydrological forecasts. Subsequently, a selection of precipitation realizations is simulated in the CLiDE environmental modelling platform, providing insight in the dominant source areas and the effects of antecedent precipitation regimes on source areas and runout paths of precipitation induced mass movement. In conclusion, 61.3 mm of daily precipitation will likely facilitate mass movement and every mm accounted for in the antecedent precipitation index reduces this threshold with 0.1527 mm when the antecedent precipitation index is based on 8 days. Although an increase of days accounted for in the antecedent precipitation index positively influenced the correlation between displaced mass and antecedent precipitation, the resulting thresholds do not agree with values applied in other studies (Ballantyne, 2004; Pennington et al., 2014). Furthermore, mass movement frequency declines under most hydrological. Nonetheless, severity likely increases as mass movement in dryer scenarios are largely driven by intense daily precipitation, whereas wetter scenarios experience extension of source areas and an increase in material entrainment due to persisting wetting. Additionally, the simulations show that the main source areas, situated between 300 and 500 metres altitude, extend upslope when antecedent precipitation regime has a late peak.

Acknowledgements

I wish to express my gratitude towards several people, who have been essential in the process of writing of this thesis. First of all I wish to thank Rens for his supervision during this process. Not only did his passion and knowledge contribute to my own motivation, also his ability to make complex matter easily understood is something that I really appreciated. I want to thank Dr. Tom Dijkstra for his feedback, especially in the early stages of my research, and for his role creating the possibility for me to spend time at the British Geological Survey. This leads me to thank Dr. Andrew Barkwith and Dr. Claire Dashwood for their supervision and help during this period. While Andy also has been a valuable help with respect to the modelling framework throughout this project. In addition, I want to emphasize my appreciation towards the British Geological Survey for their cooperation and willingness with respect to this research. A significant contribution to this research comes from the Scottish Environmental Protection Agency, especially Ms. Helen James. She has been of great help with respect to obtaining the rainfall data extensively used in this study. Likewise, I wish to thank Prof. Steven de Jong for his remarks and comments during the latter stages of this process. Furthermore I want to emphasize the support of my fellow students Laura and Joyce, who have always been of great help during programming, writing and motivational dips. I can safely say that our motivational shout "Gaan we vlammen?!" is something inseparable of all our projects. Lastly, I wish to thank Aike: on one hand for her support, on the other hand for her to urge me to take a break every once in a while, allowing me to re-evaluate my work.

Contents

1 Introduction

1.1 Relevance and Social Context of Mass Movement

1.1.1 Global

Globally, mass movement has accounted for numerous casualties and socio-economic damage in mountainous regions. Dilley et al. (2005) indicates that 3.7 million km^2 of the world is exposed to landslides. Additionally, this threatens about 5% of the world population (Kjekstad and Highland, 2009). The findings of Petley (2012) show a number 2060 landslides, responsible for 32332 fatalities worldwide over the period 2004-2010. Similarly, Dowling and Santi (2014) denotes numerous fatalities, up to 25000, resulting from debris flows. The results put forward by Dowling and Santi (2014) on the relationship between socio-economic factors and debris flows fatalities emphasize the contrast between advanced and developing countries, where the latter show to be susceptible to fatalities. Nonetheless, in advanced countries mass movements cause huge economic damages. For example, Austria, Switzerland, Italy and France have annual costs related to mass movement ranging from 0.8 to over 4 billion euros (Kjekstad and Highland, 2009). Besides direct economic damage, such as clearance, also indirect consequence can be identified Schuster (1996). Examples of which are: damage to transportation systems and mitigation costs. In perspective of future trends, Schuster (1996) addresses three main reasons for increasing damages and fatalities resulting from landslides:

- Urbanization of susceptible regions.
- Enduring deforestation.
- Increased susceptibility due to changing precipitation patterns.

As shown by Dowling and Santi (2014), debris flows are, similar to landslides, mainly triggered by rainfall. Hence the effects of the aforementioned drivers for landslides can be extrapolated to this type of mass movement as well.

1.1.2 Scotland

Large scale deforestation is an important driver for mass movement in the Scottish Highlands (Ballantyne, 2008; Mather, 2004). In addition, its geological history and climate have made the Highlands very susceptible to mass movement. High annual precipitation, steep slopes and erosion of deglaciated sediment provide extensive hazard to humans, buildings and infrastructure. As a result, the Rest and

Be Thankful pass has experienced frequent closure in the past years, about 11 times since 2007 for a total of 34 days over the period of 2007 to 2012. This road, passing through Glen Croe, is connecting the Kintyre peninsula, Argyll and Bute and the Scottish Highlands to Glasgow and the southern parts of Scotland. Closure of the pass, resulting from mass movement, has had a major impact on communities in this area. Aside from large diversions, communities can get cut off from emergency services. Moreover, the closures have a daily cost of approximately 52 thousand GBP according to Macklin (2013).

Figure 1: Rest and Be Thankful hillslope with indications of past mass movement flowpaths (BGS Landslide Team, 2018b).

The hillslope of the Rest and Be Thankful pass has been subject to various adaptation measures over the past couple of years as shown in figure 1. From 2007 to 2015 over 50 million GBP was invested to keep the A83 open. Measures such as catch pits, boulder stabilizers and extra barriers were put into practice in 2012, 2013, 2014 and 2015, followed by 13.5 million GBP added in 2016. Although these adaptation measures have proven to be successful to some extent, more sustainable measures were put forward by Macklin (2013). These measures, including constructing a viaduct

or a tunnel, ranged from 10 million GBP to 520 million GBP in costs. The constant implementation of new measures, evidently shows that current measures are still not sufficient or require constant maintenance. In light of climate change, this raises the question whether such measures can be considered both sustainable and suitable. Consequently, the effects of various climate change scenarios, as specified by the United Kingdom Climate Change Projections (Murphy et al., 2007; Christierson et al., 2012), on mass movement activity at the Rest and be Thankful pass should be evaluated. This will yield a better understanding of landscape dynamics in the pass and its implications for local communities, governments and other stakeholders in the near future.

1.1.3 Research Objectives

This study will evaluate the implications of changing precipitation patterns on the spatial and temporal characteristics of mass movement hazard at the Rest and be Thankful pass. Subsequently, this study is divided in multiple sub-questions:

- Which hydrological thresholds should be met to facilitate mass movement at the Rest and be Thankful pass?
- How does the frequency of mass movement at the Rest and be Thankful pass respond to climate change as described by United Kingdom Climate Projections?
- Is mass movement hazard in various climate change scenarios driven by daily precipitation or antecedent precipitation?
- What are the main potential source areas for the dominant mass movement types?
- Do different precipitation regimes activate different flow paths or source areas?

1.1.4 Research Approach

To determine what hydrological circumstances are able to facilitate mass movement at the study site, the daily precipitation patterns preceding recorded mass movement events are analyzed. Using a continuous precipitation dataset various mass movement events from the period 2007 to 2015 are evaluated. Subsequently, a daily precipitation threshold will be defined. This threshold is based on the precipitation occurring on the day of the mass movement event as well as the precipitation in a specified amount of days preceding the mass movement event.

Consecutively, the derived threshold will be applied to various scenarios of daily precipitation ranging to 2050, based on United Kingdom Climate Change Projections and calculated by the HadRM3 regional climate model under various model configurations. This allows the recurrence time of mass movement facilitating hydrological conditions at the Rest and be Thankful pass to be calculated, which yields insight in future mass movement frequency. Additionally, it is aimed to distinguish whether the analyzed precipitation scenarios mainly facilitate mass movement by stand-alone days or rather by days of consecutive precipitation.

A selection of threshold exceeding days, and the days considered influential preceding the day of interest, are simulated in the CLiDE environmental modelling platform. This modelling platform allows to quantify the hydrological dynamics, resulting from the precipitation selections, that govern mass movement such as soil water levels and overland flow. Consequently, the resulting hydrological dynamics reveal where dominant source areas and runout paths for mass movement are situated in the pass. In addition, by simulating selected day series from a wide range of mass movement facilitating circumstances, the response of the dominant source areas and subsequent runout paths to changing precipitation patterns can be determined.

To generate meaningful results, the modelling platform should be extensively parameterized. Consequently soil depths and soil textures at the study site are obtained from literature and past field studies. The originating soil textures will serve as input for various pedotransfer functions to compute hydrological and mechanical properties of the soil, which are required as input for the modelling platform

1.2 Theoretical Framework

1.2.1 Definitions of Mass Movement

To place the geomorphic processes within perspective, the widely applied classification by Varnes (1978) and Cruden and Varnes (1996) as shown in table 1 is considered. As indicated in table 1, the study area is characterized mainly by flow- and slide-type mass movement of unsorted and varying compositions that are commonly triggered by excessive precipitation, especially in the study area. When considering the slide-type mass movement in the area, it possible to focus mainly on translational slides. As the study area consists of mostly shallow soils situated on steep bedrock, rotational slides are hence uncommon as those generally have a deeper and curved sliding plane (figure 2).

TYPE OF MOVEMENT		TYPE OF MATERIAL		
		BEDROCK	ENGINEERING SOILS	
			Predominantly coarse	Predominantly fine
FALLS		Rock fall	Debris fall	Earth fall
TOPPLES		Rock topple	Debris topple	Earth topple
SLIDES	ROTATIONAL	Rock slide	Debris slide	Earth slide
	TRANSLATIONAL			
LATERAL SPREADS		Rock spread	Debris spread	Earth spread
FLOWS		Rock flow (deep creep)	Debris flow (soil creep)	Earth flow (soil creep)
COMPLEX		Combination of two or more principal types of movement		

Table 1: Classification scheme of mass movement, adapted from Cruden and Varnes (1996). Red marked section indicate the predominant types of mass movement in the study area.

Translational slides occur mainly along rather straight failure planes (figure 2 B). These planes can be defined by distinct features such soil-bedrock boundaries, pre-existing faults or soil horizons. Furthermore the displaced material often shows little deformation during movement such as rotation or backward tilting (Cruden and Varnes, 1996). Failure along these planes is mainly a result from the reduction of gravity-driven stabilizing forces due to wetting and subsequent buoyant effects on the potentially mobilized soil. This destabilizing process is in need of a continuous supply

of water that exceeds the outflux of water from the soil, thus increasing the pore pressure that contributes to the buoyant forces. Consequently, slides are commonly induced by either prolonged periods of precipitation or high intensity precipitation, both exceeding the soils drainage capacity. The length of these periods is mainly dependent on the characteristics of the soil.

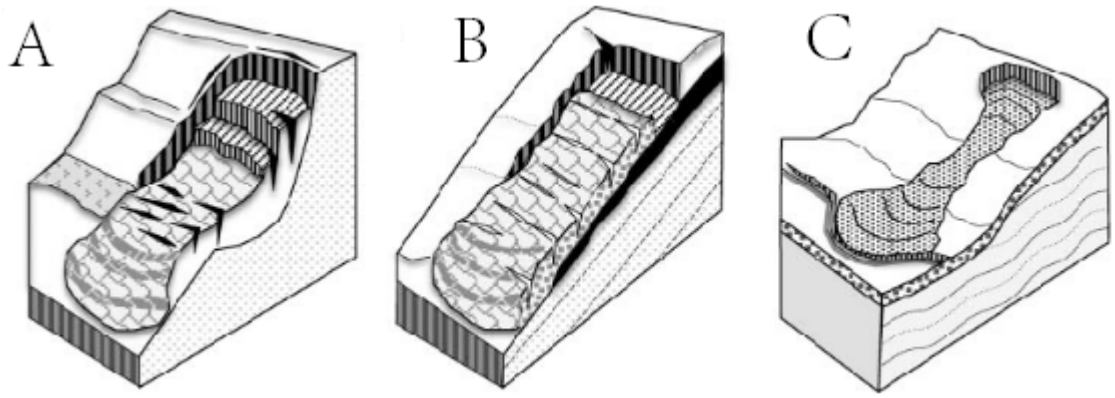

Figure 2: Types of mass movement. Note the distinction between the uncommon rotational slide, A, and the common translational slide, B. C denotes the commonly present debris flow. Adapted from United States Geological Survey (2004).

As mentioned, debris flows are a complex interplay between sediment and water. Consequently, they differ from fluid flows and avalanches or falls as these are governed by either water or solids. Debris flows can merely exist due to a combination of the two, but with at least 50 % sediment (Iverson, 1997). Due to this interplay, debris flows can transport extremely large boulders at high speeds. The suspension of smaller particles in the fluid prevents larger particles to settle, as shown in figure 3, emphasizing the importance of both fluids and solids. Furthermore, debris flows can either emerge from rigid sediments that get increasingly saturated with water (Iverson, 1997) or from overland flow entraining material (Coe et al., 2008; Berti and Simoni, 2005).

When applying the aforementioned classifications it already becomes apparent that flow- and slide-type mass movements are not autonomous phenomena. They can have similar sources and triggering mechanisms. Therefore, falls, topples, slides and spreads can be converted into, or initiate, slide- or flow-type movements if enough water is involved or entrained (Crozier, 1986). Explanatory for this complex interplay are the findings of Pierson and Costa (1987) on rheologic behaviour of sediment-water flows and their associated flow velocities. These show that water and sediment

interact in a continuous spectrum of movement types, depending on the ratio of water and sediment, which can vary over the flows' trajectory.

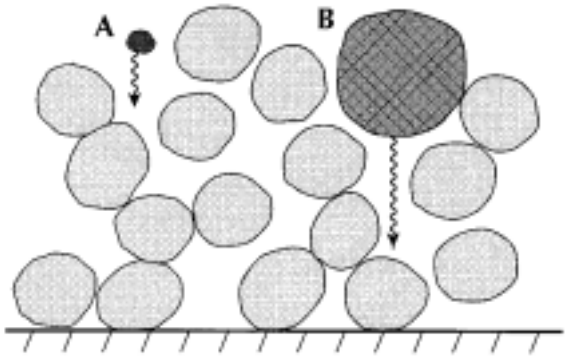

Figure 3: Particle-fluid interaction (A) and particle-particle interaction (B) in suspension within a debris flows. From Iverson (1997).

1.2.2 Mass Movement and Hydrology

As shortly introduced in section 1.2.1, hydrological factors largely govern the type of mass movement and are responsible for the initiation of mass movement. As discussed by Van Asch et al. (1999), various types of mass movement are triggered by different hydrological mechanisms. Debris flows are mainly triggered by surface runoff increasing the debris internal pore pressure. The water influx is resulting from high intensity precipitation on rather short timescales, minutes to hours. Shallow landslides are mainly triggered by infiltration and subsequent increasing pore pressures or weakening of the soil strength. Similarly, deep-seated landslide are mainly triggered by rising groundwater levels and the subsequent increase in pore pressure, thus acting on larger timescales, days to months, as groundwater often responds relatively slow to hydrological trends.

The summarized mass movements are mainly triggered by increasing pore pressure at their failure planes. Shown in figure 4 are the effects of this process when considering its relation to the normal stress and shear stress on a portion of soil.

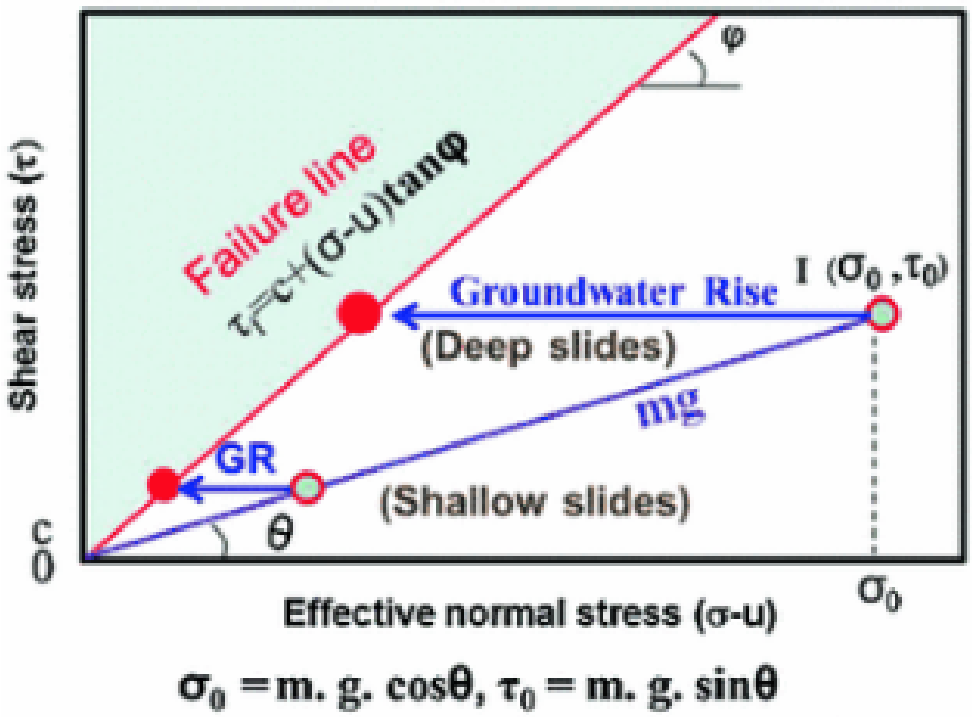

Figure 4: Effect of pore pressure on failure mechanisms in landslides, adapted from Sassa et al. (2017).

Climate change often implicates hydrological changes as well. Consequently, the process depicted in figure 4 can either be enhanced when climate change imposes persistent wetting of a catchment or be diminished when continual drying occurs. Additionally, changes in precipitation patterns can influence the frequency of different mass movement types. More intense precipitation patterns would imply more debris flows and shallow landslides whereas prolonged precipitation will likely trigger more deep-seated types of mass movement. Therefore, climate change can alter the nature of mass movements both though long-term and short-term processes.

1.3 Geomorphological Setting

The current geomorphology and climatic conditions are considered key in the current mass movement activity at the Rest and Be Thankful pass. Consequently, the parameterization of the proposed modelling framework CLiDE should resemble the study site properly. Thus, insight in the geological history and current geomorphology is essential in understanding the current landscape dynamics and the associated mass movement.

The study site is characterized by glacigenic sediments, overlaying the Beinn Bheula Schist Formation. This formation consists of well bedded metagreywacke of Neoproterozoic origin, which is somewhat feldspathic and includes bands of phyllitic metamudstone and metasiltstone. The material is ought to be deposited as strata of siliciclastic turbidites on submarine fans (Tanner et al., 2013). The original structures responsible for the relief of the area are mainly extensive nappe folds which were subsequently reformed by upright folding in various directions (Stephenson and Gould, 1995). The present geomorphology is mainly governed by a recent history of glaciation. During the late Devensian, Scotland was largely covered by ice-sheets, extending to the Atlantic shelf. The subsequent retreat, mainly between 12.9-11.5 kyr, resulted in the onset of extensive reworking and redistribution of the remaining sediments by strong erosion, as shown in figure 5. Consequently, little amounts of the original drift can be traced back in such valleys as different sediment transport processes superseded glacial transport, such as debris flows (Ballantyne, 2002, 2004). These sedimentary processes caused the present geomorphology to be mainly characterized by extensive gully systems, incising the sediments.

Figure 5: Development of valleys after deglaciation. Left: the onset of gullies formation. Middle: the deposition of eroded material at gully outlets. Right: established drainage patterns that expose bedrock. From Ballantyne (2002).

These processes often result in a complex and poorly sorted stratigraphy as presented in figure 6. Accordingly, these stratigraphies can comprise of sediments that can vary strongly in their characteristics over short distances, including texture and

sorting. These factors are influenced by the origin of the glacier, its path and glacial remnants such as moraines. Consequently, glacial history has a significant impact on the current geomorphological dynamics.

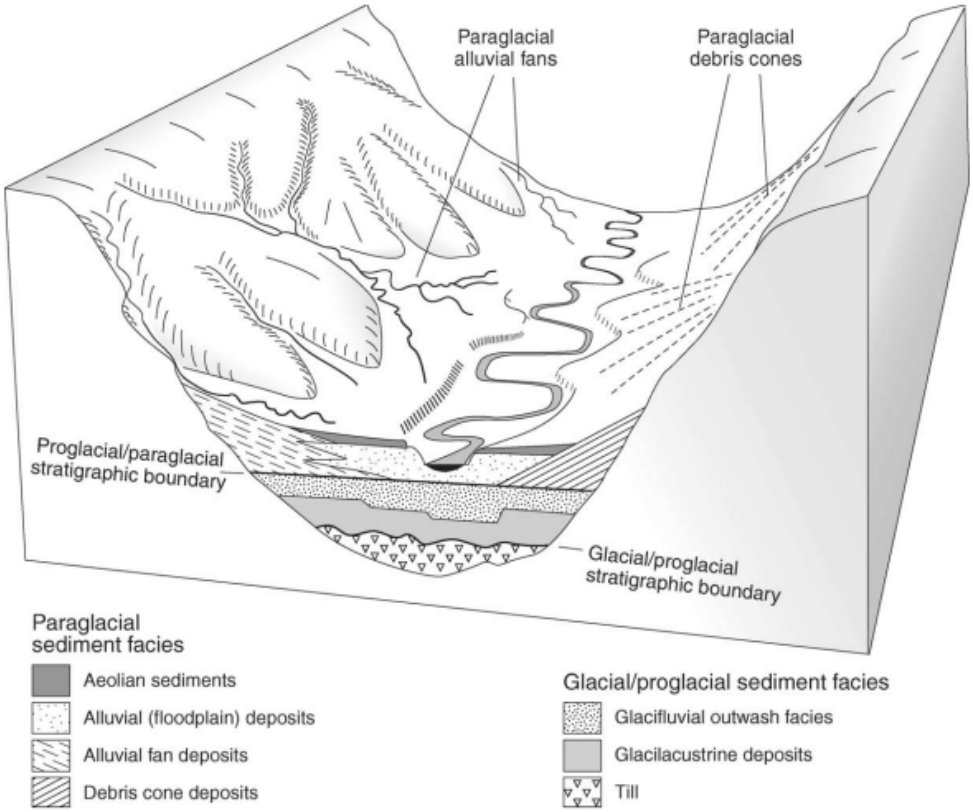

Figure 6: Schematic overview of a possible composition of a valley subject to various geomorphological effects attributed to glaciation. From Ballantyne (2002).

Aside from the nature of the sediments, excessive precipitation is the main driver for geomorphological dynamics and is hence a major contributor to the increased susceptibility of the area to mass movement. Figure 7 indicates that the Rest and be Thankful pass is among the wettest parts of Scotland, experiencing over 2000 mm of precipitation per year or more.

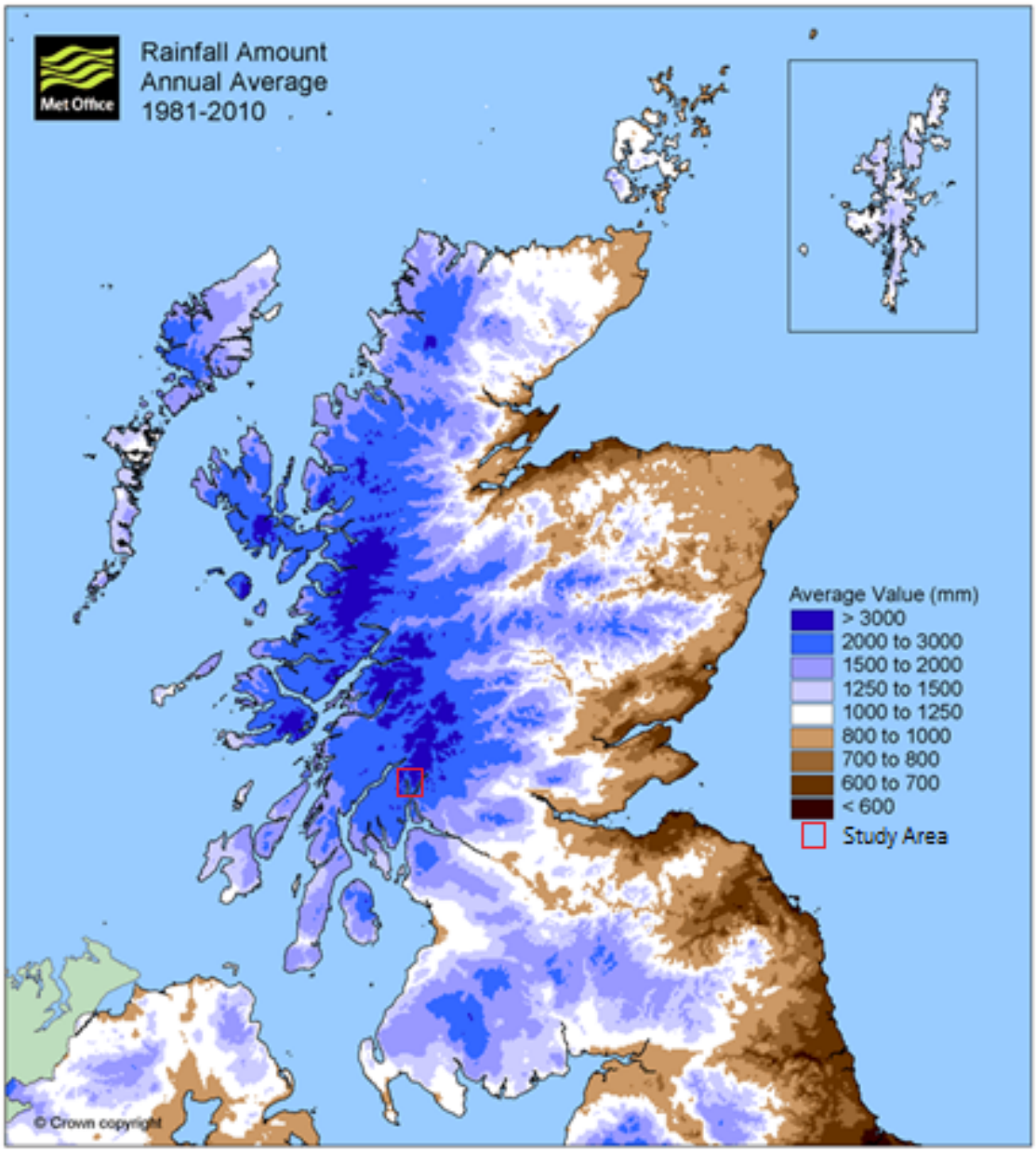

Figure 7: Annual average precipitation (MetOffice, 2018).

2 Methods

2.1 Hydrological Analysis

2.1.1 Threshold: Antecedent Precipitation Index

As discussed in sections 1.2.1,1.2.2 and by Iverson (2000), mass movement is largely initiated by excessive precipitation. Following catchments characteristics, such as soil- and lithological properties, topography, landuse and meteorology, the water entering the system has a certain residence time in the catchments stores. Consequently, it is estimated to what extent the antecedent precipitation and daily precipitation influence mass movement initiation using the antecedent precipitation index (Bruce and Clark, 1966; Glade et al., 2000). Following Bruce and Clark (1966), the antecedent precipitation index (API) is defined as:

$$API_0 = \sum_{i=1}^{n} k^i \cdot r_i \tag{1}$$

Where API_0 represents the antecedent precipitation index on day 0, k is an iteratively found decay factor representing the water outflux from the regolith and n indicates the amount of antecedent days accounted for in the API. The next aim is to deduct a hydrological threshold line using the combinations of daily rainfall and the API that are known to have initiated mass movement in the study area. Hence the calculated API, for $n = 4$, $n = 8$ and $n = 12$, are plotted against the daily precipitation data of the study area, which includes days of known mass movement events. Subsequently, the line fitting through the lowest data points that have experienced mass movement is considered to be threshold. This will result in a threshold in the from of equation 2.

$$T = -\alpha \cdot API_0(n) + R_0 \tag{2}$$

Where T is the daily rainfall needed to initiate mass movement in mm as function of the API_0 in mm on the day on interest based on n days and R_0 being the rainfall in mm needed to induce mass movement when no antecedent precipitation has been present. Furthermore, the unitless decay factor α accounts for the reducing need of daily precipitation to initiate mass movement when the API increases.

2.1.2 Forecasting: United Kingdom Climate Projections

In order to draw conclusions with respect to the frequency and severity of mass movement activity at the Rest and be Thankful pass under climate change, the

aforementioned threshold value, T, is applied to realizations of daily rainfall from the United Kingdom Climate Projections (UKCP) spanning to 2050, based on SRES A1B emission scenario.

Subsequently, a selection is made from threshold exceeding events, which will be simulated in the modelling framework CLiDE to gain insight in the spatial dynamics of mass movement following various precipitation patterns. The selection of events should be representative for the largest possible variation in rainfall and API that can trigger mass movement at the study site. Consequently, the selection is based on the convex hull (Weisstein, 2018) of all events exceeding the calculated threshold line T. This method narrows the scenarios to be evaluated down to a comprehensive selection realized extremes.

To quantify the impact of climate change on mass movement, the recurrence time of exceedance of threshold T in all scenarios is calculated by dividing the number of days that exceed the established threshold by the total amount of days. Furthermore, when deriving the recurrence times, the recurrence times for the associated APIs and daily precipitation, grouped in 10 millimeter intervals, are also calculated. When plotting these independently their relative spread indicates the principal driver of mass movement within this realized RCM scenario. Additionally, applying an one-way ANOVA (Daniel, 1990) to the API values and daily precipitation of the days from each RCM scenario that meet the established threshold, allows to differentiate between the RCM scenarios, based on either the daily precipitation or the associated API.

2.1.3 Hydrological Correlation to Mass Observations

As mass approximations of the cleared material from the recorded events are available, it is possible to find a correlation between displaced mass, rainfall and antecedent precipitation of historic mass movement events. The relationship between those factors is useful to determine in what situations more mass can be expected to be displaced and thus in the identification of scenarios that will experience more severe mass movement, based on the amount of antecedent- or daily precipitation. Moreover, it allows to test whether the statistics of the simulated run out is an accurate resemblance of the observed run out. Hence, the hypotheses of significant correlation will be tested for two types. Firstly, Pearson's linear correlation coefficient, which is given by:

$$P_\rho(p,r) = \frac{\sum_{i=1}^{n}(p_i-\overline{p})(r_i-\overline{r})}{\left(\sum_{i=1}^{n}(p_i-\overline{p})^2(r_i-\overline{r})^2\right)^{\frac{1}{2}}} \tag{3}$$

Where n is the amount of observations, p is the predictor variable and r the response variable. However, the linearity of both variables might not be of the same magnitude. Consequently, Spearman's ρ, based on the rank of the observations, is calculated as well using:

$$S_\rho(p, r) = 1 - \frac{6 \sum d^2}{n(n^2 - 1)} \tag{4}$$

Where d is the difference between the ranks of the predictor variable and its corresponding response variable. Furthermore, the significance level can be tested using:

$$P_{val} = \frac{r\sqrt{n-2}}{\sqrt{1 - C_r}} \tag{5}$$

Where C_r defines the correlation coefficients retrieved from either equation 3 or 4.

2.2 CLiDE Framework

2.2.1 Modelling of Mass Movement in CLiDE

To study the patterns in mass movement emerging from hydrological drivers, the CLiDE modelling platfrom is used. Originally, the development of the CLiDE modelling platform aimed to integrate various well established models that all quantify different parts of geomorphological and hydr(geo)logical systems and their interactions through models based on cellular automata. However, modelling landscape dynamics acting on different temporal scales often face challenges concerning model complexity, the extent of inter-connectivity of different components and the nature of the applied model (Mulligan and Wainwright, 2004). Hence, driven by the DESC (Dynamic Environmental Sensitivity to Change) project, the Cellular Automaton Evolutionary Slope and River(CAESAR) model (Coulthard and Van de Wiel, 2006) and Lisflood-FP (Coulthard et al., 2013; Bates et al., 2010) were integrated, forming CAESER-Lisflood-DESC. According to Barkwith et al. (2015), the mere integration of CAESAR and Lisflood-FP was not satisfactory in all aspects as it remains to simplify some hydrological and hydrogeological phenomena. Barkwith et al. (2015) specifically addresses the absence groundwater flow and the contribution of groundwater to river discharge. Consequently, an additional hydrological module is implemented in CLiDE, covering groundwater flow and governing the surface hydrology that CAESAR neglects. The conceptual outline of CLiDE is depicted in figure 8

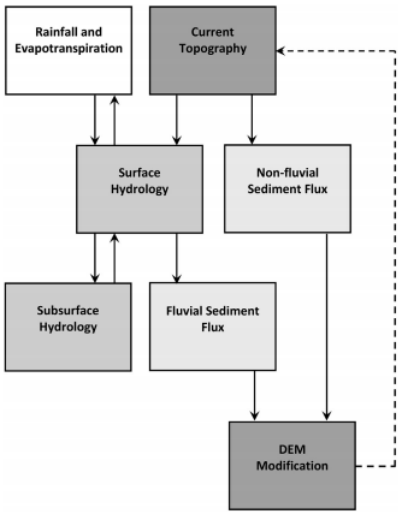

Figure 8: Schematic overview of the covered processes in CLiDE from Barkwith et al. (2015). Note that the dashed line represents the start of a new timestep.

2.2.2 CLiDE Setup

In CLiDE, water and material are redistributed through a von Neumann neighbourhood scheme using interactions between adjacent cells that represent physical phenomena, as shown in figure 9.

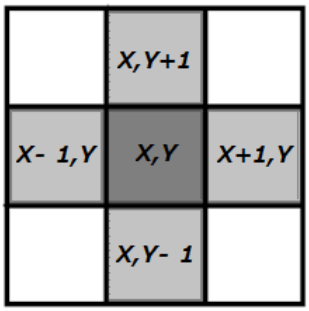

Figure 9: von Neumann neighborhood.

As shown in figure 10, rainfall that is not evaporated or contributes directly to runoff and thus reaches the soil surface is partitioned through the systems stores. Firstly, the influx from rainfall into the soil contributes to the near soil surface storage and the reduction of the soil moisture deficit. When field capacity is reached, soil moisture drains towards the soil-bedrock interface and is able to percolate into the bedrock or form a saturated layer. Any excessive water reaching the soil, $E_w[m^3]$, is now partitioned between runoff, R_o, and recharge to the ground water, R_e, using equations 6, 7 and the baseflow index parameter, BFI. This empirical parameter is based on the classification of hydrological properties of soils by Boorman et al. (1995).

$$R_o = E_w \cdot (1 - BFI) \qquad (6) \qquad\qquad R_e = E_w \cdot BFI \qquad (7)$$

Though the BFI partly accounts for the catchments slopes, equations 6 and 7 are specified to account for local slope angles, S, and the average slope angle, $\overline{S}$. This leads to equations 8, 9 and 10.

$$R_o = \frac{E_w \cdot (1 - BFI) \cdot S}{\overline{S}} \qquad (for : S \leq \overline{S}) \qquad (8)$$

$$R_o = \frac{E_w \cdot BFI \cdot (S - \overline{S})}{90 - \overline{S}} \qquad (for : S \geq \overline{S}) \qquad (9)$$

$$R_e = E_w - R_o \qquad (10)$$

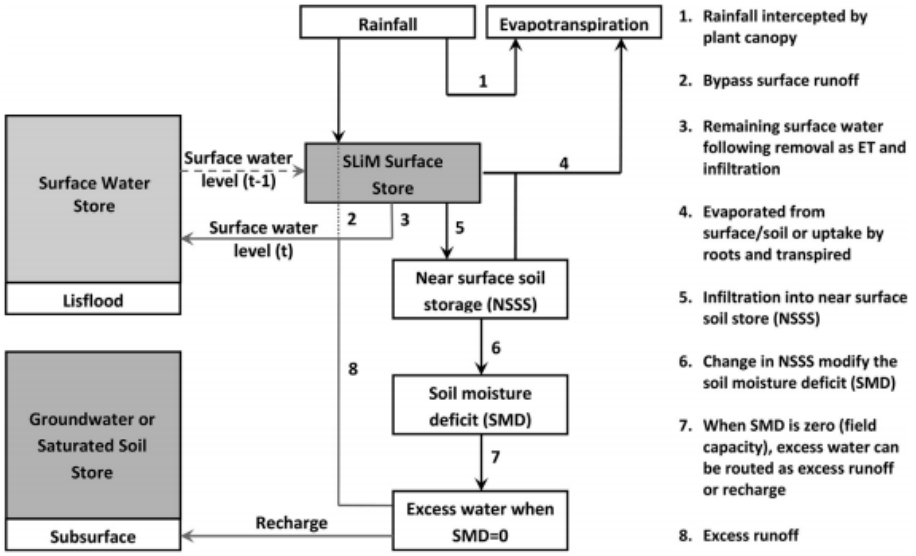

Figure 10: Schematic overview of the partitioning of water through hydrological processes at the soil surface within CLiDE, from Barkwith et al. (2015).

The subsequent runoff is redistributed through the system using Lisflood-FP (Coulthard et al., 2013). Here the flow between adjacent cells is defined as:

$$Q_{sw}^{x,y} = \frac{Q_{sw}^{x,y}(t-1) - g \cdot w_{hf}^{x,y} \Delta t (\Delta (w_h^{x,y} + Z^{x,y}) / \Delta S_g)}{(1 + g \cdot w_{hf}^{x,y} \Delta t n^2 |q_{sw}| / w_{hf}^{x,y^{10/3}})} \Delta S_g \tag{11}$$

Where Q_{sw}(t-1) is the flux from the previous timestep in $m^3\ t^{-1}$, g the acceleration by gravity in m t^{-2}, n Mannings n, w_h is the local water depth in m, Z is the elevation in m, w_{hf} is the absolute difference between adjacent cells' water depth in m, S_g the gridsize in m and t being time as specified by the user. Following equation 11 it is possible to calculate the new w_h for each cell, using equation 12:

$$\frac{\Delta w_h^{x,y}}{\Delta t} = \frac{Q_{sw}^{x-1,y} - Q_{sw}^{x,y} + Q_{sw}^{x,y-1} - Q_{sw}^{x,y}}{\Delta S_g^2} \tag{12}$$

The subsurface redistribution of water occurs both in a saturated layer at the soil-bedrock interface and in a saturated layer at the bedrock base. Subsurface flow is simulated similar in both these layers, which are considered unconfined. The subsurface flow is governed by:

$$\nabla T r \nabla w_{ssh} + W = 0 \tag{13}$$

Where W is a lumped source/sink term and transmissivity, Tr in $\mathrm{m}^2 \cdot \mathrm{t}^-1$, is assumed to be equal to the saturated hydraulic conductivity of the layer of interest times the thickness of the saturated layer. Consequently, when considering flow in the x-direction $Q_{gw}^{x,y}$ in $\mathrm{m}^2 \cdot \mathrm{t}^-1$ is approximated by:

$$Q_{gw}^{x,y} = -\overline{Tr}^{x,y} \frac{w_{ssh}^{x,y} - w_{ssh}^{x-1,y}}{\delta S_g} \tag{14}$$

Where $\overline{Tr}$ is the harmonic mean of the transmissivity of neighbouring cells, defined by:

$$\overline{Tr} = \frac{2Tr^{x,y}Tr^{x-1,y}}{Tr^{x,y} + Tr^{x-1,y}} \tag{15}$$

Finally, the subsurface water head in a central cell is defined each timestep using the discrete mass balance equation:

$$w_{ssh}^{x,y}(t + \Delta t) = w_{ssh}^{x,y}(t) + \frac{1}{Sy^{x,y}} \frac{Q_{gw}^{x,y}}{S_g^2} \Delta t \tag{16}$$

Change in the saturated water height in the bedrock, w_{gsh} is calculated similarly to equation 16 and using the corresponding tranmissivity and specific yield. Figure 11 shows an summarized overview of the aforementioned hydrological processes.

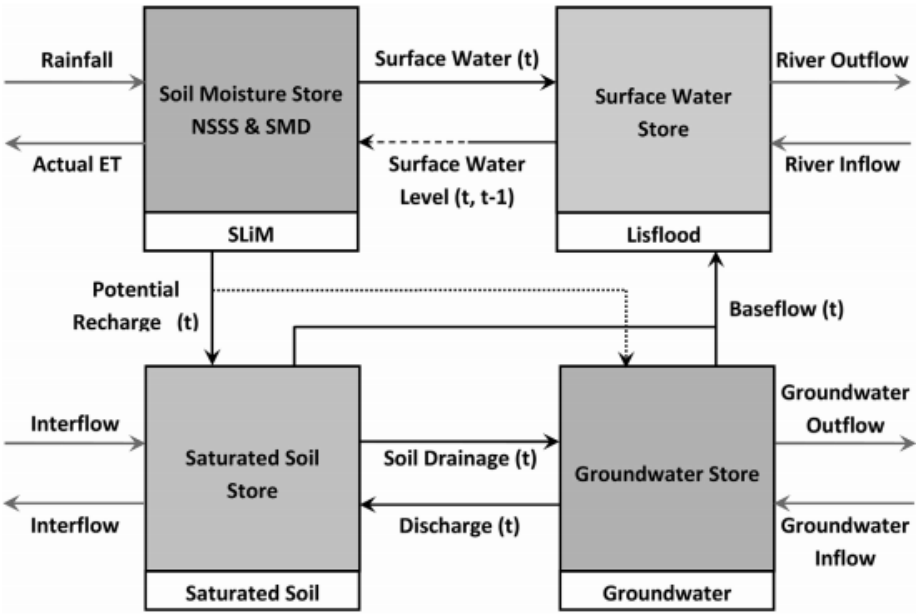

Figure 11: Schematic overview of the covered hydrological processes in CLiDE from Barkwith et al. (2015). Note that non-linking arrows depict nodal interaction.

Table 2 presents an overview of the input parameters for CLiDE, which are used in the aforementioned equations.

Table 2: Relevant input parameters within CLiDE

Parameter:	**Property:**
Z	Elevation
B_i	Bedrock depth
$K1_{sat}$	Saturated hydraulic conductivity of the soil
$K2_{sat}$	Saturated hydraulic conductivity of the bedrock
$Sy1$	Specific yield of the soil
$Sy2$	Specific yield of the bedrock
w_{ssh}	Soil saturated water height
w_{gsh}	Bedrock saturated water height
SMD_i	Initial soil moisture deficit
$NSSS_i$	Initial near soil surface storage
PE	Potential evapotranspiration
$HOST$	Hydrology of soil type

2.2.3 SCIDDICA-Module Setup

Various studies (Shroder et al., 2011; Korup et al., 2010; Claessens et al., 2007) address the role of mass movement as a key process in both short term and long term geomorphological dynamics in a wide range of environments, including Scotland (Ballantyne, 2018). Consequently, shallow landsliding and debris flows have been included in CLiDE to improve the modelled geomorphological dynamics. On the basis of the infinite slope model (Selby, 1982) shallow landslides and debris flows are initiated. Subsequently, the transport of the mobilized mass is quantified using the SCIDDICA-model as presented by D'Ambrosio et al. (2003) and Di Gregorio et al. (1999). The CLiDE modelling framework links hydrological conditions to mass movement through the infinite slope model (Selby, 1982). This model assumes slope failure when the shear stress, τ, of a portion of soil above a failure plane exceeds the shear strength, S_s, of that designated portion of soil. The shear stress is defined by:

$$\tau = \rho_s \cdot g \cdot h \sin\beta \cos\beta \tag{17}$$

Where ρ_s is the soil density in g$\cdot$ cm^{-3}, g is the acceleration due to gravity in m$\cdot$ s^{-}2, h the soil depth in m and β the slope angle in degrees. Subsequently, the shear

strength is defined as:

$$S_s = C + (\rho_s \cdot h - \rho_w \cdot w_{ssh}) g \cos^2 \beta \tan \phi \tag{18}$$

Where, C is the cohesion of the soil in Pa, ρ_w the density of water in g$\cdot$ cm^{-3}, w_{ssh} the saturated soil water depth in m and ϕ the internal friction angle in degrees. Substituting equations 17 and 18 in $\tau > S_s$ yields:

$$\tan \beta > \frac{C}{\rho_s g w_{ssh}} + (1 - \frac{\rho_w \cdot w_{ssh}}{\rho_s \cdot h}) \tan \phi \tag{19}$$

This condition is linked to the hydrological component of CLiDE through the soil moisture deficit, resulting in:

$$\tan \beta > \frac{C}{\rho_s g w_{ssh}} + (1 - \frac{\rho_w}{\rho_s \cdot h} \frac{P_s - SMD}{P_s}) \tan \phi \tag{20}$$

Where P_s is the total pore space. Figure 12 shows a schematic overview of the forces and effects described above.

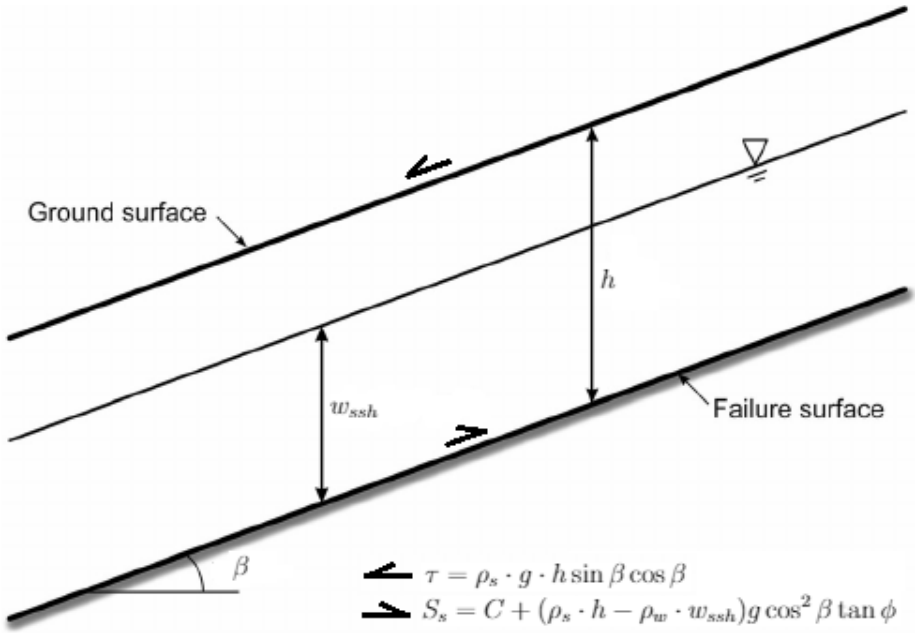

Figure 12: Forces acting on a slope and the incorporation of hydrological effects.

When the aforementioned condition is met, the SCIDDICA-module is activated for that cell. In the SCIDDICA-module, the conservation of energy of a failing cell is the result of various parameters and cell states, shown in tables 3 and 4.

Table 3: Cell states within SCIDDICA$_{3-hex}$ from D'Ambrosio et al. (2003)

Cell State:	**Property:**
Q_a	Cell elevation
Q_{th}	Thickness of potentially mobilized material
Q_e	Potential energy of potentially mobilized material
Q_d	Soil depth
Q_o	Outflow to neighbouring cell

Table 4: Parameters within SCIDDICA$_{3-hex}$ from D'Ambrosio et al. (2003)

Parameter:	**Property:**
P_a	Cell apothem
P_t	Timestep
P_{adh}	Adhesion of potentially mobilized material
P_f	Height threshold, based on internal friction angle
P_r	Relaxation rate (internal timestep)
P_{rl}	Energy loss due to frictional effects
P_{mt}	Soil mobilization threshold
P_{er}	Progressive erosion factor

Consequently, mass movement within SCIDDICA can be defined by equation 21. Where R defines the cellular area, X defines the geometrical characteristics of neighbouring cell, T being a transition function for the interaction between the cells over time defined in R and both P and Q as previously defined.

$$MassMovement(R, X, T, Q, P) \tag{21}$$

Following the considerations opted by D'Ambrosio et al. (2003) regarding hydraulic behaviour, it is possible to calculated the kinetic head of a flow within a cellular automaton environment (equation 22). The energy a flow can be quantified using the supposed run-up, or height of the incoming flow, r.

$$h_k = \frac{v^2}{2g} \tag{22}$$

$$r = h + \frac{v^2}{2g} = h + h_k \tag{23}$$

Considering a cell, with soil depth h, area A_c and mass m, the potential energy

is is calculated by formula 24:

$$U = \rho g A_c \int_0^h z dz = \rho g A_c \left[\frac{z^2}{2}\right]_0^h = \frac{\rho g A_c}{2} \cdot h^2 \tag{24}$$

Consequently, h is increased by r. Conservation of mass results in a new expression of ρ:

$$\rho_n = \frac{h}{r}\rho \tag{25}$$

Hence, ρ_n and r are substituted in equation 24, forming:

$$U_n = \frac{\rho_n g A_c}{2} r^2 = \left(\frac{h}{r}\rho\right)\frac{g A_c}{2} r^2 = \frac{\rho g A_c}{2} hr \tag{26}$$

From table 3, equation 26 and the assumption that $\rho g A_c$ it is derived that r is proportional to the potential energy of the material and its thickness by $2/\rho g A_c$:

$$r = \frac{2Q_e}{\rho g A_c Q_{th}} \tag{27}$$

Table 5 shows overview of how the conservation of mass, momentum and energy is achieved through the model framework.

Table 5: Transition functions, applied in SCIDDICA (D'Ambrosio et al., 2003)

Transition Function:	**Local Interaction**:
1. Debris outflow to adjacent cells:	$Q_a^0 \cdot Q_{th}^0 \cdot Q_e \cdot p_{adh} \cdot p_r * p_f \rightarrow Q_0^4$
2. Calculating debris thickness and energy:	$(Q_{th}^0 \cdot Q_e \cdot Q_0^4)^0 \rightarrow Q_{th} \cdot Q_e$
3. Calculation of soil erosion and entrainment:	$Q_a \cdot Q_e \cdot Q_{th} \cdot Q_d \cdot p_{er} \cdot P_{mt} \rightarrow Q_a \cdot Q_{th} \cdot Q_e \cdot Q_d$
4. Calculation energy losses due to friction:	$Q_{th} \cdot Q_e \cdot p_{rl} \rightarrow Q_e$

1. The outflow of debris to adjacent cells is computed by the algorithm as described by Di Gregorio and Serra (1999), which eliminates neighbouring cells, based on the angles between the central cell and the adjacent cells, β_i, between $Q_a^0 + r$ and $Q_a^i + Q_{th}^i$. When $\beta_i < p_f$, the cell is eliminated from the possible flow path. Subsequently, the flow to a non-eliminated cell i is given by $f(i) = A_a - q(i)$, where A_a is the average value of the non-eliminated cells. As a result, the normalized outflow is $Q_o(0 \to i) = \frac{2}{\rho g A_c} \frac{(Q_{th}^0)^2}{Q_e^0}$

2. The updated thickness and energy are based upon the exchange of mass with the adjacent cells through the flow, which is calculated in transition function 1. Consequently, the new thickness in a cell is defined as $nQ_{th}^0 = Q_{th}^0 + \sum_{i=1}^{6}(Q_o(i,0) - Q_o(0,i))$. A similar method applies to the newly computed energy: $nQ_e^0 = (Q_{th}^0 + \sum_{i=1}^{6}(Q_o(0,i) \cdot \frac{Q_e^0}{Q_{th}^0}) + (\sum_{i=1}^{6} Q_o(i,0) \cdot Q_o(i,0) \frac{Q_e^i}{Q_{th}^i})$

3. Soil erosion due to the moving mass occurs when $Q_e^0 > p_m t$, the amount of entrained is defiend by $\Delta_d = (Q_e^0 - p_m t) p_e r$. Other substates are updated accordingly: $nQ_d^0 = Q_d^0 - \Delta_d$; $nQ_{th}^0 = Q_{th}^0 + \Delta_d$; $nr^0 = r + \Delta_d$ and $nQ_e^0 = Q_e^0 + Q_e^0 \frac{\Delta_d}{Q_{th}^0} + \frac{2}{\rho g A_c}(Q_{th}^0 \Delta_d + \Delta_d^2)$.

4. Energy losses due to friction are applied through a reduction of the run up height, thus the energy of the moving material Q_e. Mathematically this results in $\Delta_r = p_r l$ when $\frac{2}{\rho g A_c} \frac{Q_e^0}{Q_{th}^0} - p_r l > Q_{th}^0$ otherwise $\Delta_r = \frac{2}{\rho g A_c} \frac{Q_e^0}{Q_{th}^0} - Q_{th}^0$. Finally, the energy of the moving material is updated by: $nQ_e^0 = Q_e^0 - \frac{2}{\rho g A_c} \Delta_r Q_{th}^0$

Originating from the framework described above, prior identification of potential source areas reduces computational time as less nodes require evaluation. Consequently, potential source area are identified using the infinite slope model, applied to the soil water levels originating from the simulated scenarios.

2.3 Parameterization

As depicted in section 2.2, the CLiDE modelling framework requires extensive parameterization, including mechanical and hydrological properties of the soil as well as its depth, SCIDDICA-module parameters and initial hydrological conditions. Consequently, the soil depth is derived from a small logging transect and subsequently scaled over the study area. Furthermore, the soil texture is derived literature and the results used as input for pedotransfer functions, which produce the required soil properties.

2.3.1 Bedrock Depth

Limited borehole data is available from a relatively small logging transect performed by the BGS in 2009, summarized in table 6. These boreholes cover only an elevation range of approximately 7.5 metres. As detailed modelling of long term hillslope evolution is not the aim of this research, the measured values are averaged in order to serve as input for a simplified linear function. As discussed by Roering (2008); Pelletier and Rasmussen (2009a); Heimsath et al. (2001) hillslope gradient is critical in modelling hillslope evolution. Combining this with the assumption of downslope transport of material and the measured soil depths, it is possible to extrapolate the measured soil depth over the area of interest and generate a reasonable initial bedrock depth.

$$B_i(x,y) = Z(x,y) - \frac{D_1 \cos\beta(x,y))}{Z(x,y)^{D_2}} \tag{28}$$

Where B_i is the initial bedrock depth, Z is the elevation in metres, D_1 and D_2 are empirical scaling parameters and β is the slope angle. The empirical parameter D is derived from solving 28 for the averaged values of the borehole measurements as presented in 6. Consequently, during this study a value of 1257.9 metres is applied for D_1. Including parameter D_2 is ought necessary as without this term, the soil thickness tends to be overestimated. Moreover, this parameter causes a stronger decrease of the soil cover upslope. Hence, this parameter is set at 1.12.

To make the generated bedrock more representative of an irregular bed overlaid by soil, spatially correlated noise is applied to the generated bedrock depth, using equation 29.

$$B_{n(x,y)} = B_i(x,y) + r_n(x,y) \tag{29}$$

Where $B_{n(x,y)}$ is the newl bedrock, $B_i(x,y)$ the originally derived bedrock and $r_n(x,y)$, a random number from a normal distribution with mean 0 and standard deviation 2.

Table 6: Borehole Data

Borehole Code:	**Soil Depth:**	**Angle:**	**Elevation:**
NN20NW15	7.0 m	23°	225.3 m
NN20NW16	5.6 m	25°	222.5 m
NN20NW17	2.5 m	25°	224.2 m
NN20NW19	5.7 m	30°	220.3 m
NN20NW20	6.2 m	22°	217.9 m
NN20NW22	3.8 m	29°	217.8 m
Average	5.13 m	26°	221.3 m

To make the noise spatially correlated, the numbers in r are filtered using the moore grid and fractional contributions shown in equation 30.

$$r_n(x,y) = \sum \begin{bmatrix} r(x_{-1},y_{-1}) & r(x,y_{-1}) & r(x_{+1},y_{-1}) \\ r(x_{-1},y) & r(x,y) & r(x_{+1},y) \\ r(x_{-1},y_{+1}) & r(x,y_{+1}) & r(x_{+1},y_{+1}) \end{bmatrix} \odot \begin{bmatrix} 0.0251 & 0.1453 & 0.0251 \\ 0.1453 & 0.3183 & 0.1453 \\ 0.0251 & 0.1453 & 0.0251 \end{bmatrix} \tag{30}$$

The new bedrock is used to redistribute material through the system and generate new soil on the basis of the model proposed by (Pelletier and Rasmussen, 2009a) that aims to quantify soil thickness over time, whilst neglecting transport.

$$\frac{\partial h}{\partial t} = \frac{\rho_b}{\rho_s} \frac{P_0}{\cos\beta} \exp\left(\frac{-h\cos\beta}{h_0}\right) \tag{31}$$

Where t is time, ρ_b is the mineral bedrock density in g$\cdot$ cm^{-3}, ρ_s is the soil density in g$\cdot$ cm^{-3}, h_0 is characteristic soil depth of 0.5 metres after Heimsath et al. (1997, 1999, 2001), β is the slope angle in degress and P_0 is the maximum potential production rate of the bedrock in m$\cdot$ t^{-1}. Based on the findings of Pelletier and Rasmussen (2009b) for the maximum production rate for granite, shown in figure 13, combined with a mean annual temperature of 9.5 °C and a mean annual precipitation assumed at 2 metres would yield a value of approximately 0.00025 m$\cdot$ yr^{-1}. However, due to its schistosity, the bedrock likely weathers more easily. The schistosity causes water to intrude more easily in microstructures, enhancing weathering and thus production rates (Marui and International Research Society Interpraevent, 2006). This leads to the assumption of a maximum potential production rate of 0.0003 m$\cdot$ yr^{-1}.

To generate a representative soil cover, equations 32 and 33 are introduced to initiate transport of soil over the area.

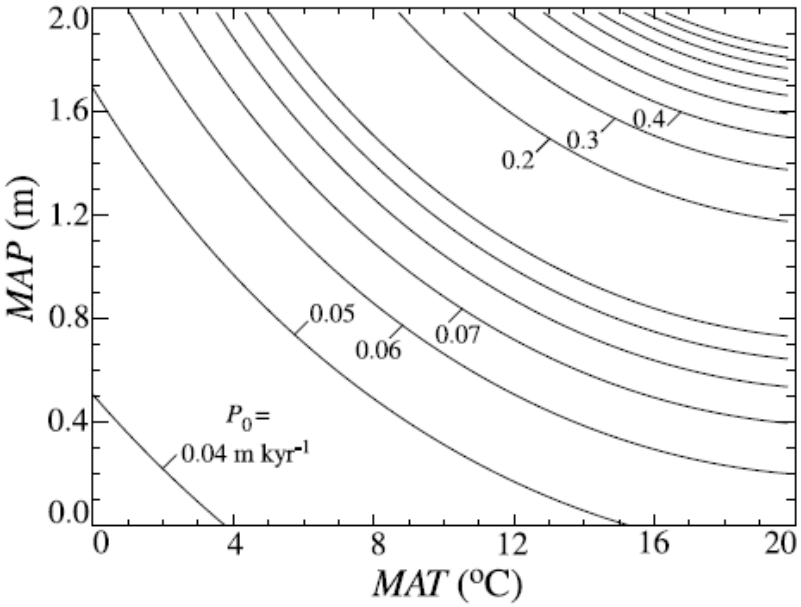

Figure 13: Relationship between maximum potential production rate from granite and mean annual temperature and mean annual precipitation by (Pelletier and Rasmussen, 2009b)

$$Q_s(x) = -D_e \frac{\mathrm{d}Z}{\mathrm{d}x} \qquad (32) \qquad\qquad Q_s(y) = -D_e \frac{\mathrm{d}Z}{\mathrm{d}y} \qquad (33)$$

Where Q_s is the soil flux in $\mathrm{m}^3 \cdot \mathrm{t}^{-1}$, D_s is the erosive diffusion in $\mathrm{m}^2 \cdot \mathrm{t}^{-1}$ and $\frac{\mathrm{d}Z}{\mathrm{d}x,y}$ the change of elevation in the x- and y-direction. Within this study, the erosive diffusion is based on the rate of soil creep as discussed by Kirkby (1967) and a rate based on frequent landslide activity by Martin (2000) yielding an erosive diffusivity of $0.1002\ \mathrm{m} \cdot \mathrm{yr}^{-1}$. Following, the net flow of soil is calculated using forward integration (equation 34).

$$Q_n(x,y) = \frac{Q_s(x,y) - Q_s(x+1,y) + Q_s(x,y) - Q_s(x,y+1)}{C_a} \qquad (34)$$

$$h_n(x,y) = Q_n(x,y) + h(x,y) \qquad (35)$$

Where Q_n is the net flow per cell in metres and C_a the cell area in m^2 and h_n is the new soil depth. Equations 31, 32,33, 34 and 35 are applied to the initial soil cover and bedrock depth every timestep in a spin up time of 1 kyr. The resulting soil cover and bedrock depth are used in this research.

2.3.2 Soil Texture

Similar to the data availability regarding soil depth, indications of soil texture were also very limited in their support to this research. However, based on findings of Bown et al. (1982) and Rayner and Nicoll (2012) a representative soil texture can be realized. Bown et al. (1982) classify the area, referred to as 'the area between Loch Fyne and Loch Lomond', as loam to silty loam with occasional sandy loam. Furthermore, where relatively high silt contents are observed, 35% to 50%. Rayner and Nicoll (2012) classifies the predominant soils as sandy silt to silt loam. in conclusion, the soil should have high sand and silt contents with strong variations in their ratio, caused by the reworking of moraines. Shown in table 7 and figure 14 are initial fractions of soil textures that are likely to be found in the area. These are used to generate a realization of the soil texture, encompassing all these classes.

Table 7: Realizations of soil textures.

Soil Classification:	**Sand:**	**Clay:**	**Silt:**
Sandy Loam	50 %	5%	45%
Silt Loam	20 %	15%	65%
Silt Loam	35 %	10%	55%

Based on the NRCS-USDA classification system, a standard deviation is defined that allows the soil texture to vary within designated range that cover the aforementioned soil textures or their close proximity. Together with the predefined fraction and a random number from the standard normal distribution, the assumed standard deviation serves as input for equation 36.

$$T_{f,i}(x,y) = \mu_i(x,y) + (\sigma_{f,i} \cdot r_n(x,y)) \tag{36}$$

Where $T_{f,i}(x,y)$ is the fraction of texture class i, $\mu_i(x,y)$ is the predefined fraction of texture class i, $\sigma_{f,i}$ is the standard deviation of texture class i and $r_n(x,y)$ a random number from the standard normal distribution. The values applied to generate the soil textures marked in figure 14 are depicted in table 8.

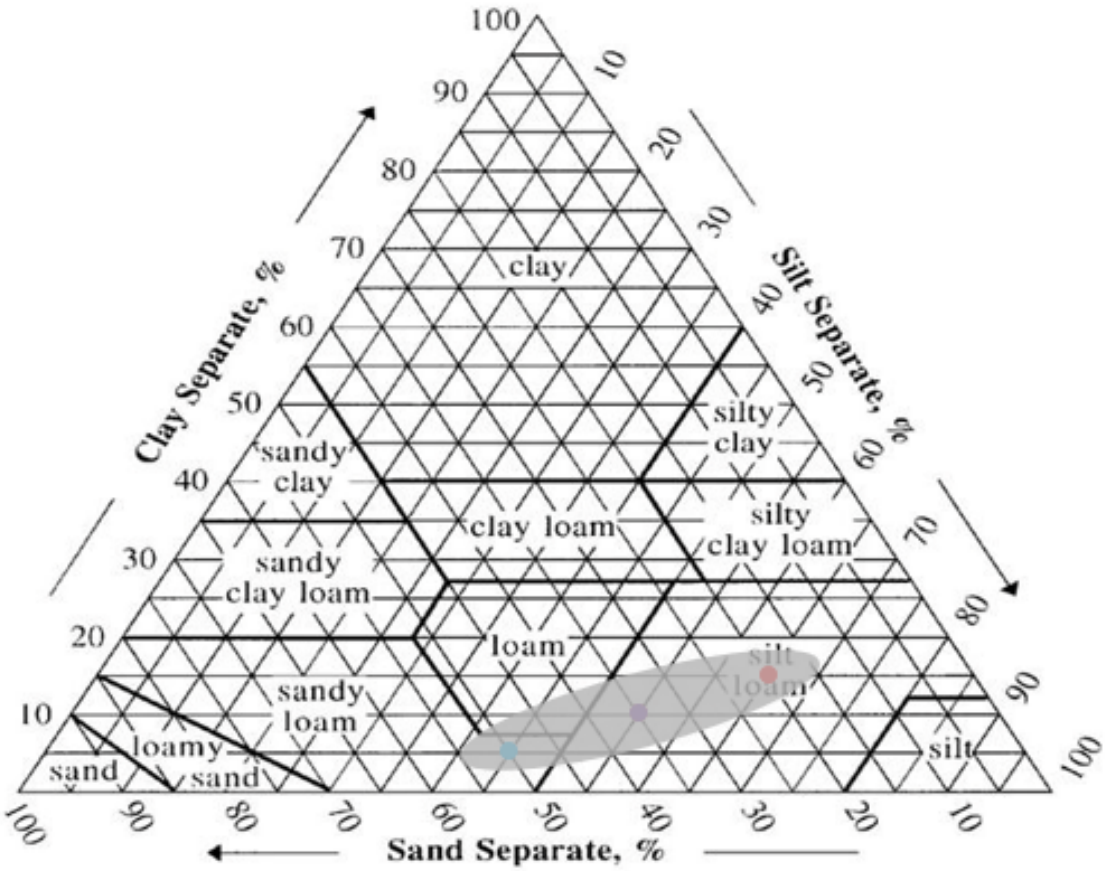

Figure 14: NRCS-USDA soil texture triangle. The oval mark indicates the range in which the majority of the soil texture should vary.

Table 8: Parameters applied in equation 36.

Soil Texture:	**Sand:**	**Clay:**	**Silt:**
μ_i	35 %	10%	55%
$\sigma_{f,i}$	15 %	5%	15%

Similar to the soil depth, in the case of soil texture spatial correlation can be assumed. Therefore, a similar disk-shaped filter is applied as shown in equation 37.

$$r_n(x,y) = \sum \begin{bmatrix} r(x_{-2},y_{-2}) & r(x_{-1},y_{-2}) & r(x,y_{-2}) & r(x_{+1},y_{-2}) & r(x_{+2},y_{-2}) \\ r(x_{-2},y_{-1}) & r(x_{-1},y_{-1}) & r(x,y_{-1}) & r(x_{+1},y_{-1}) & r(x_{+2},y_{-1}) \\ r(x_{-2},y) & r(x_{-1},y) & r(x,y) & r(x_{+1},y) & r(x_{+2},y) \\ r(x_{-2},y_{+1}) & r(x_{-1},y_{+1}) & r(x,y_{+1}) & r(x_{+1},y_{+1}) & r(x_{+2},y_{+1}) \\ r(x_{-2},y_{+2}) & r(x_{-1},y_{+2}) & r(x,y_{+2}) & r(x_{+1},y_{+2}) & r(x_{+2},y_{+2}) \end{bmatrix} \odot \begin{bmatrix} 0.0 & 0.0170 & 0.0381 & 0.0170 & 0.0 \\ 0.0170 & 0.0784 & 0.0796 & 0.0784 & 0.0170 \\ 0.0381 & 0.0796 & 0.0796 & 0.0796 & 0.0381 \\ 0.0170 & 0.0784 & 0.0796 & 0.0784 & 0.0170 \\ 0.0 & 0.0170 & 0.0381 & 0.0170 & 0.0 \end{bmatrix} \quad (37)$$

2.3.3 Soil & Bedrock Properties

To estimate the soil properties considered crucial in the analysis of the study area, pedo-transfer functions formulated by Balland et al. (2008) are applied. An overview of the properties that are to be computed and their corresponding functions is shown below. The relevant bedrock properties are derived from literature.

$$\rho_B = \frac{1.23 + (\rho_s - 1.23 - 0.75 \cdot T_{f,s}) \cdot (1 - \exp\{-0.0106 \cdot h_s\}}{1 + 6.83 \cdot T_{f,om}} \tag{38}$$

$$\log_{10}(K_{sat}) = -0.98 + 7.94 \log_{10}(\rho_s - \rho_b) + 1.96 \cdot T_{f,s} \tag{39}$$

$$FC = n(1 - \exp\left\{ \frac{-0.588(1 - T_{f,s}) - 1.73 \cdot T_{f,om}}{n} \right\} \tag{40}$$

$$PWP = FC(1 - \exp\left\{ \frac{-0.511 T_{f,cl} - 0.865 \cdot T_{f,om}}{FC} \right\} \tag{41}$$

$$SP_v = 1 - \frac{\rho_b}{\rho_s} \tag{42}$$

$$WHC = FC - PWP \tag{43}$$

The properties shown above are calculated for three defined soil layers. These range from 0 to 30cm, which includes organic matter, from 30 to 100cm, where an exponential decrease in organic matter is applied and from 100 to 150 cm where little to no organic matter is present. Note that these layers are absolute and thus will not occur at locations where the soil depth is not sufficient. Additional soil properties are relevant for slope stability analysis. These concern the angle of internal friction and cohesion. Prellwitz (1981) constructed a function that yields the internal friction angle on the basis of soil texture, as presented in equation 44.

$$\cot \phi' = k_{\phi 1} - k_{\phi 2} \cdot D_r \tag{44}$$

Where ϕ is the internal friction angle, $k_{\phi 1}$ and k_2 are adjustment parameters, whilst D_r is the relative density of the soil. D_r is computed from equation 45 using the void ratios following from equation 46, the porosity originating from equation 42, with a minimum porosity of 0.26 and a maximum porosity of 0.6.

$$D_r = \frac{E_{max} - e}{E_{max} - E_{min}} \quad (45) \qquad e_i = \frac{n_i}{1 - n_i} \quad (46)$$

Table 9: Parameters resulting in the effective angle of internal friction from equations 44 and 46 (adapted from Prellwitz et al. (1994))

Soil Texture:	$\phi'(D_r = 100\%)$	$\phi'(D_r = 0\%)$	$k_{\phi 1}$	$k_{\phi 2}$
Sand	33°	43°	1.54	0.0043
Silt	26°	36°	2.05	0.0067
Clay	15°	37°	3.73	0.0240

The parameters, shown in table 9, serve as input for equations 44 and 45. Consequently, the weighed average from the soil texture classes is the resulting effective friction, ϕ'. Though the soils effective cohesion might be a result of interplay between the texture and geological history (consolidation, cementation and particle attraction), for fine-grained soils, it can be assumed that the occurring cohesion can mainly be attributed to the present clay particles. This results in the application of equation 47.

$$C = 21.27 \cdot T_{f,c} \quad (47)$$

Where 21.27 kPa is an optimized value derived from the EUROSEM-model (Morgan et al., 1998) and $T_{f,c}$ is the clay fraction. Note that the mechanical parameters are calculated for the soil the complete soil column. As some of the model parameters in the proposed framework do not allow for distributed vallues, some of these are applied in CLiDE and SCIDDICA using their weighed averages, where the layer thickness determines the partitioning between the values.

2.3.4 Initial Hydrology

The hydrological conditions that require input are the initial soil moisture deficit, the initial near soil surface storage, the potential evapotranspiration, the hydrology of the soil type and the saturated water layers in both the soil and bedrock. Based on the prevailing hydrological conditions in the study area, wet conditions are most likely to occur. Hence, the soil moisture deficit is assumed to be 0 initially, indicating that the soil is at field capacity. Similarly, the near soil surface storage is assumed to be 0 too. This allows for some storage in the soil before drainage will cause a saturated water layer to occur at the soil-bedrock interface. Furthermore,

the potential evapotranspiration will be derived from FAO standard values. The hydrology of the soil type will be classified according to Boorman et al. (1995). The initial thickness of saturated water in the bedrock is derived by running a available timeseries of rainfall of 180 days from 1960 with a completely saturated bedrock. It is aimed to find a balance point where little change occurs in the groundwater levels, which subsequently will serve as the initial saturated water layer in the bedrock. The saturated water layer in the soil is assumed to be zero following the assumption of the soil being at field capacity.

2.3.5 SCIDDICA

The input parameters used in the SCIDDICA-module are derived from the calibration as performed by D'Ambrosio et al. (2003). As this calibration is done for a different catchment, some input parameters are expected to be altered iteratively in an attempt to simulate the 2015 mass movement event, during which the amount of mass displaced serves as a tool of comparisson. The values shown in table 10 are therefore used as a starting point.

Table 10: Values calibrated by D'Ambrosio et al. (2003)

Parameter:	**Value:**
P_{adh}:	$0.001m$
P_f	$0.1m$
P_r	1
P_{rl}	$0.6m$
P_{mt}	$3.5m^2$
P_{er}	0.015

3 Datasets

3.1 Historical Data

The historical data available for this study spans from 2007 to 2017. This data concerns 15 minute rainfall measurements, obtained by the Scottish Environmental Protection Agency (James, 2017). However, measurement sites were only installed in late April 2012 at the Rest and be Thankfull pass. Data prior to then, from 2007 to 2012, is measured at an operational site at Inveruglas which was the closest site to the Rest and Be Thankful, approximately 10 km northwest of the pass. As the CLiDE modelling framework operates on a daily time scale and the realizations of the UKCP are generated on a daily basis, the 15 minute values are summed to daily values to yield both adequate values for comparison and a proper data format.

Estimates of the amount of displaced mass during historical events, recorded at the Rest and be Thankful pass, are derived from the BGS National Landslide Database (BGS Landslide Team, 2018a) and summarized in table 11.

Table 11: Overview of the recorded historical events, available for this study.

Mass Movement Event Date:	Displaced Mass (kg):
30-12-2015	250000
05-12-2015	1000000
28-10-2014	2000000
01-10-2013	100000
01-08-2012	1000000
01-02-2012	40000
08-09-2009	730000
28-10-2007	400000

3.2 United Kingdom Climate Projections

The realizations of future daily precipitation originate from 11 atmospheric parameterizations of the HadRM3 regional climate model (RCM), which aim to quantify the implications of climate change for the United Kingdom, following a SRES A1B emission scenario (Murphy et al., 2009). This has resulted in various datasets of

hydrometeorological time series on a daily time scale and a 25 km^2 resolution. The climate sensitivity, the average temperature rise resulting from a doubling of the atmospheric carbon stock, of the configurations are summarized in table 12 (Christiersson et al., 2012; Murphy et al., 2007; Hadley Centre for Climate Prediction and Research, 2008).

Table 12: RCM identifications and corresponding resulting climate sensitivity in HadRM3, adapted from Hadley Centre for Climate Prediction and Research (2008).

RCM ID:	Resulting Climate Sensitivity (K):	Average Daily Precipitation (mm):
x:	3.53	7.76
a:	2.53	7.77
c:	2.82	7.61
h:	3.44	7.87
i:	4.40	7.83
j:	3.90	7.56
k:	4.44	7.53
l:	4.88	7.85
m:	4.54	7.50
o:	4.80	7.35
q:	7.11	7.73

4 Results

4.1 Hydrological Analysis

4.1.1 Hydrological Thresholds

Three realizations of the API for the Rest and be Thankful pass are calculated. Within these realizations, a value of 0.92 for the decay factor, k, is applied. Here the APIs for n=4, n=8 and n=12 and the forthcoming thresholds are shown respectively for all months in which mass movement was recorded from 2007 to 2017.

When n=4, n=8 and n=12 are applied to the months in which mass movement is recorded, it is evident that the applied method is able to largely separate the data. However, the movement event from October 2007 fails to meet the established criteria. On the contrary, the hydrological conditions considered sufficient for mass movement are met several times without any recorded movement. Namely in October 2014 and August 2012.

Logically, n=8 and n=12 yield a wider spread of data points due to higher values for the API. However, higher values of n seemingly cause slightly stronger grouping, which is mainly evident in the December 2015 and October 2013 data . Furthermore, it can be observed that increasing n from 8 to 12 causes less drastic change compared to the shift from n=4 to n=8.

Furthermore, the intercept with the y-axis denotes the daily rainfall needed to meet hydrological conditions that could initiate mass movement. These allow for comparison with existing analyses of the study area. These values for n=4, n=8 and n=12 are 71.2 mm, 61.3 mm and 57.1 mm respectively. When these values for n are fitted to equation 2, they result in:

$$R = -0.3014 \cdot API_0(n = 4) + 71.2 \tag{48}$$

$$R = -0.1527 \cdot API_0(n = 8) + 61.3 \tag{49}$$

$$R = -0.0981 \cdot API_0(n = 12) + 57.1 \tag{50}$$

As n =8 agrees best with the findings of Ballantyne (2004) and Pennington et al. (2014), it will be applied in further analysis. Consequently, the hydrologic threshold for mass movement is deducted from data presented in figure 15.

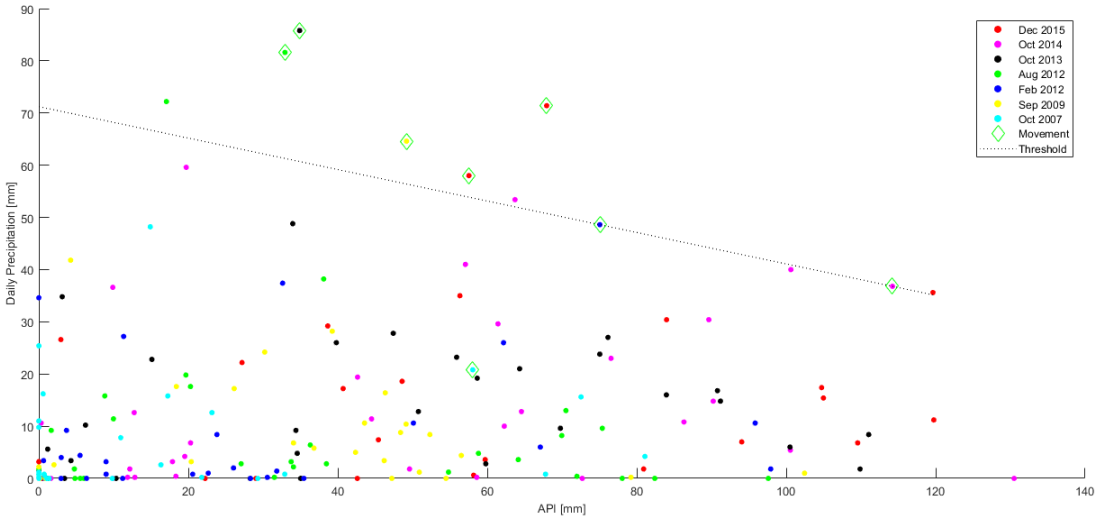

(a) $n = 4$

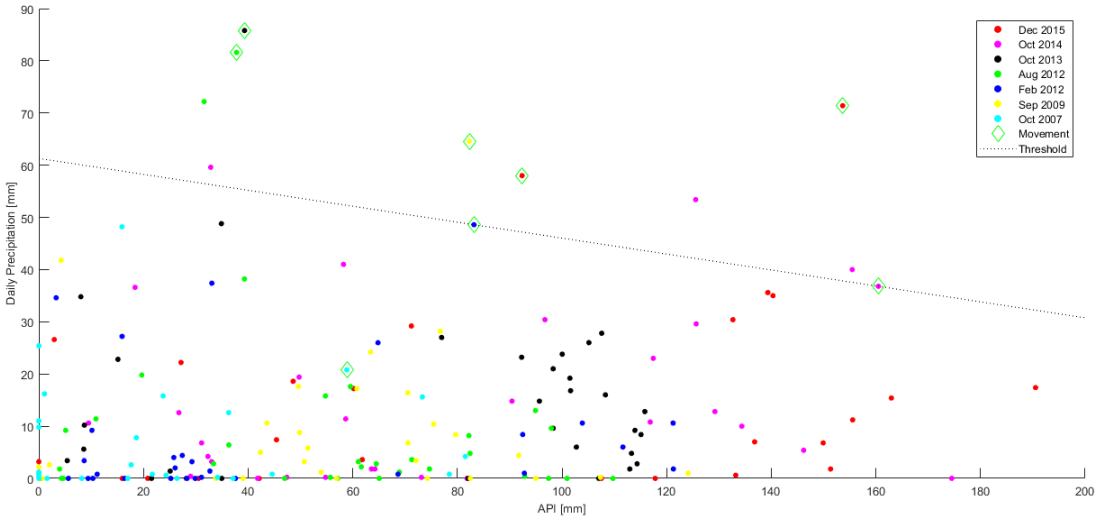

(b) $n = 8$

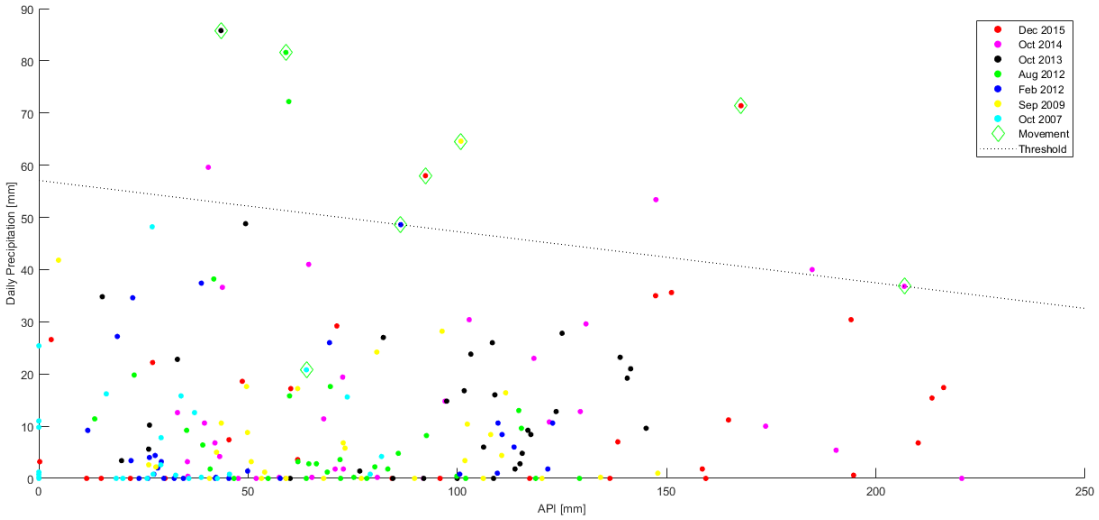

(c) $n = 12$

Figure 15: Antecedent precipitation index, based on $n = 4$, $n = 8$ and $n = 12$ respectively, for all recorded mass movement events from 2007 onward.

Figure 16 shows the application of the threshold to the continuous time series of daily rainfall data from 2007 to 2017. Henceforth, the recurrence time of the hydrological conditions that are able to facilitate mass movement is substantially higher than the recorded mass movements as it is found to be 51 days. When this threshold is applied only to the time series, measured closer to the pass over the period of 2012 to 2017, the recurrence time is 67 days. Furthermore, it is evident that the hydrological conditions are met more frequently than would appear from figure 15 compared to the application the derived threshold to the continuous dataset. Consequently, when the hydrological conditions are met, the mass movement probability is 7.46 % when considering the data from 2012 to 2017.

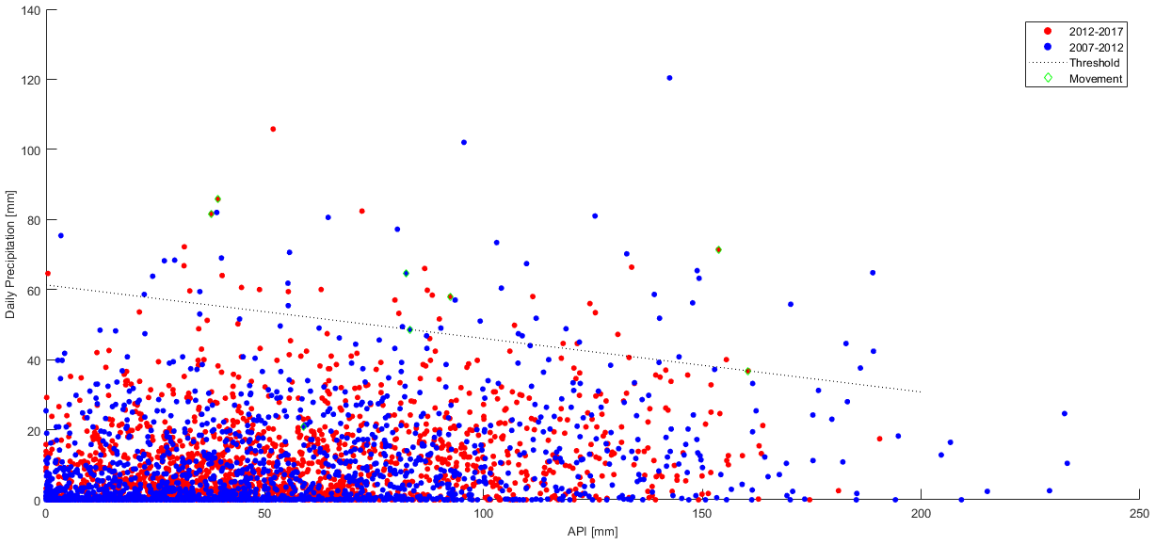

Figure 16: Overview of daily rainfall and corresponding APIs for $n = 8$ from the 2007-2017 record relative to the threshold

4.1.2 Hydrological Forecasting

Using equation 49, the RCM realizations are analyzed. As shown in figure 17, the realized RCM datasets show a wide variation in how they respond to climate change and inherently the forthcoming hydrological conditions. Especially RCMs i, j and l show a vast reduction in recurrence time. The other RCMs mainly show an increase in recurrence time, presumably reducing mass movement hazard in terms of frequency.

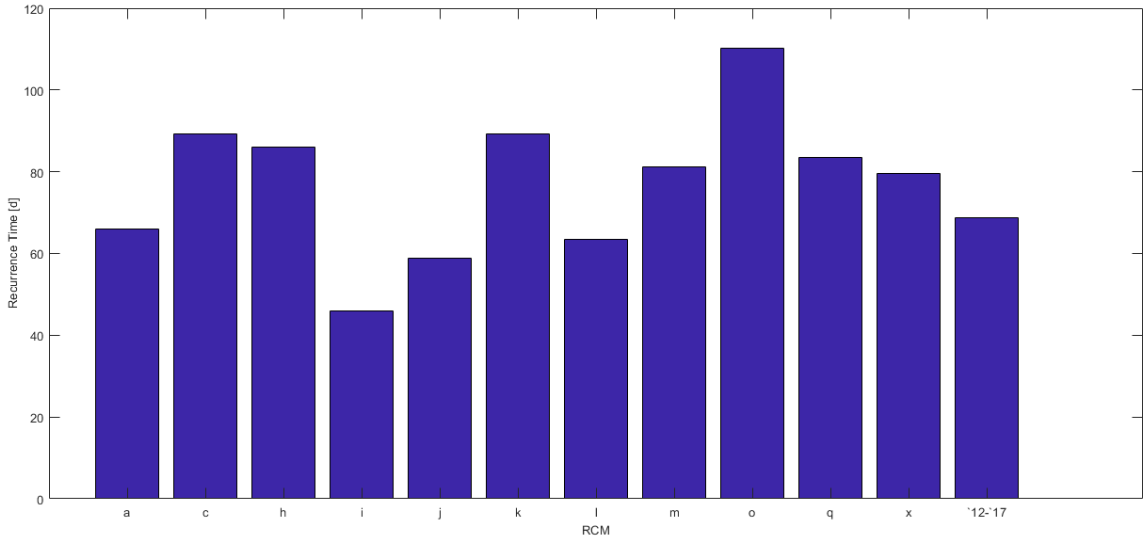

Figure 17: Recurrence times for all RCM realizations and the records from 2012 to 2017 for the exceeding of the hydrological threshold.

Aside from the recurrence times, the variation in spreading of the one-way ANOVA (Daniel, 1990) on the APIs and daily precipitations that exceed the threshold, shows whether significant changes in mass movement triggering and subsequent intensity will occur. According to figure 18, the realizations of daily rainfall from the RCMs do differ significantly from observations of daily rainfall over 2007-2017. However, it is evident that the observations show a bigger spread. Furthermore, the average daily rainfall during exceeding of the threshold is relatively high with respect to the RCMs. Furtermore, it seems that mainly RCM scenarios o, q and m are governed by daily precipitation.

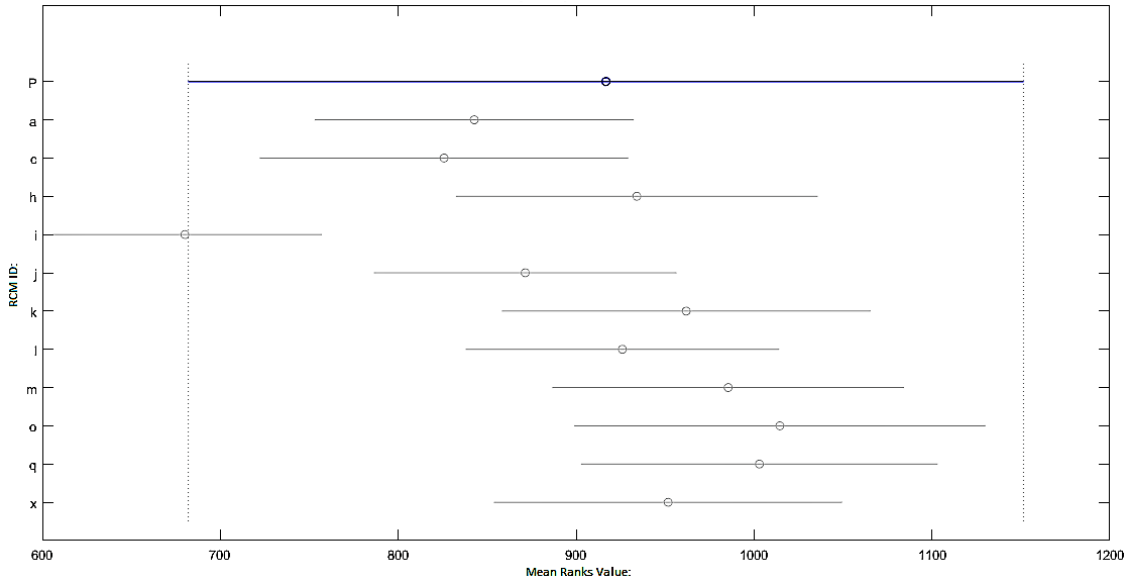

Figure 18: Comparison of the mean ranks of daily rainfall for the RCMs with respect to the 2007-2017 time series (indicated by P).

Figure 19 shows that the reciprocal differences considering the API are very similar to those observed in figure 18. However, in case of the API the are substantially more datasets significantly different from each other. Nevertheless, the observations from 2007-2017 only show significant differences with those realized in RCM i. Additionally, it becomes evident that also RCM scenarios i, j and to some extent a and h are mainly driven by antecedent precipitation.

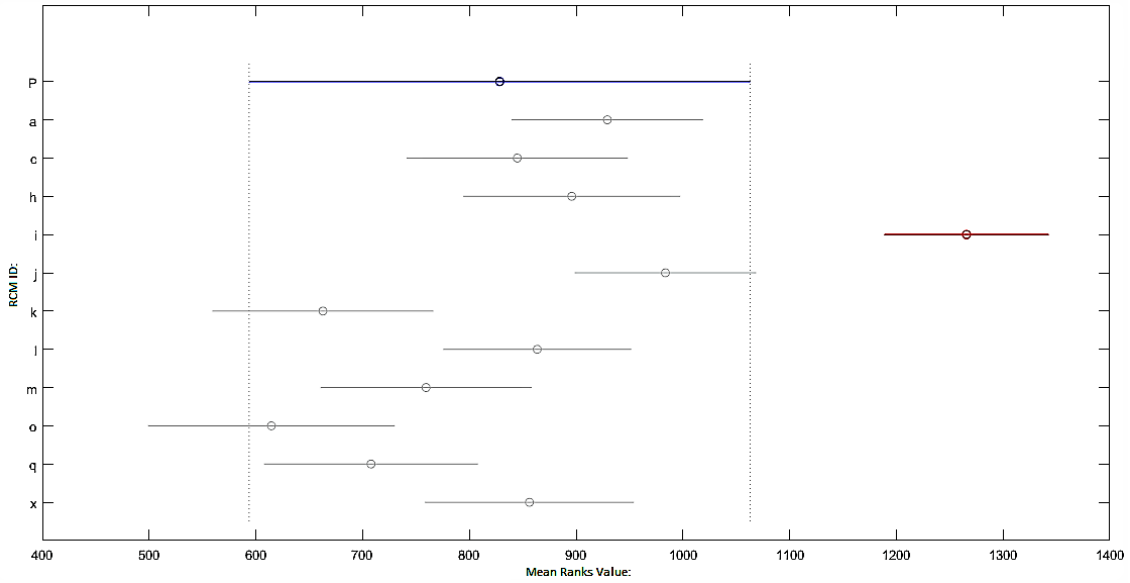

Figure 19: Comparison of the mean ranks of the $API(n = 8)$ for the RCMs with respect to the 2007-2017 time series (indicated by P).

However, these results should be viewed in relation to the recurrence times shown in figure 17 but also in relation to the interplay in the recurrences times of the antecedent precipitation and daily precipitation. Shown in figure 20 are the recurrence times for all threshold exceeding as subtracted from the RCM scenarios. Here the daily precipitation is grouped using 5 mm intervals to discretize the limited amount of data. Similarly, the API is discretized using 10 mm intervals. These results indicate that under the different RCM scenarios, mass movement can either be largely facilitated by the daily precipitation or antecedent precipitation. Distributions with high recurrence times for low daily precipitation values imply that mass movement in this scenario is largely initiated by antecedent precipitation, such as RCM i. On the contrary, distributions with low recurrence for low daily precipitation values imply that mass movement will mainly be driven by daily precipitation, such as RCM o.

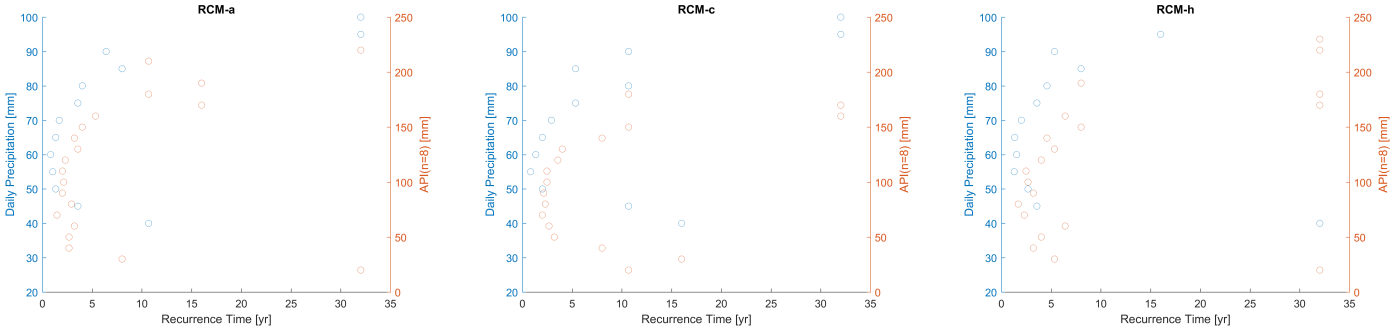

(a) RCM-a **(b)** RCM-c **(c)** RCM-h

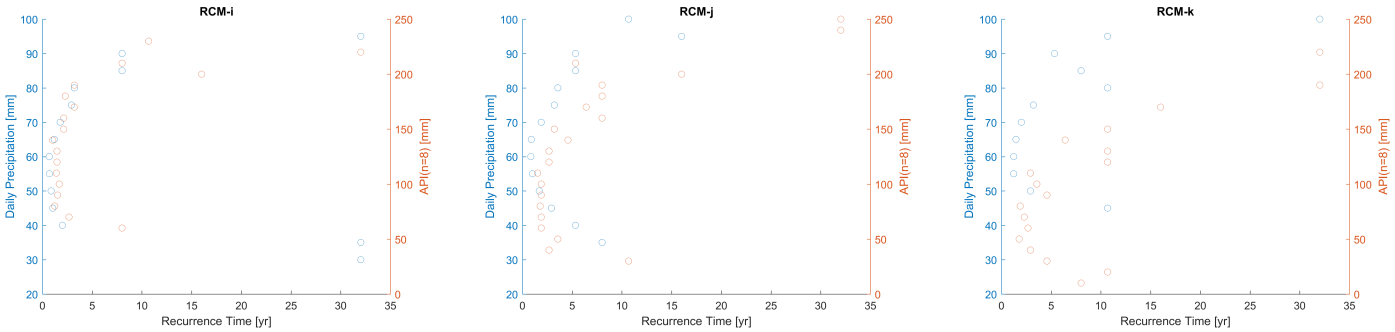

(d) RCM-i **(e)** RCM-j **(f)** RCM-k

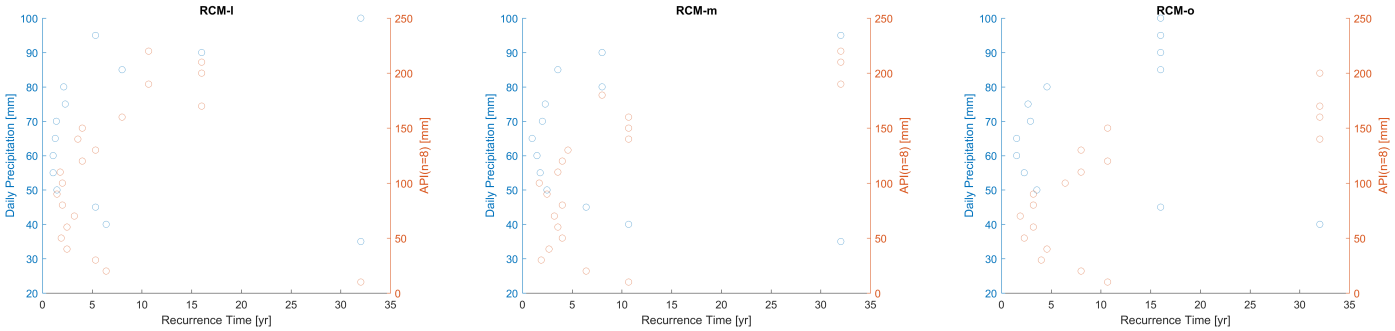

(g) RCM-l **(h)** RCM-m **(i)** RCM-o

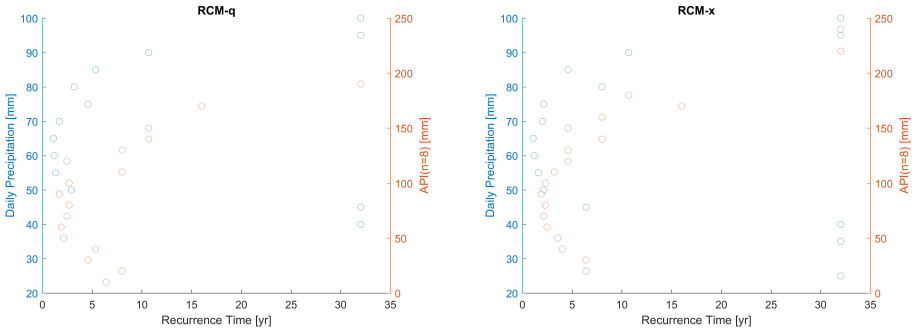

(j) RCM-q **(k)** RCM-x

Figure 20: Recurrence times for all RCM scenario with consideration of the hydrological driver.

Based on the convex hull of the plotted data, shown in figure 21 b, 10 scenarios are compiled from the realizations. The indicated scenarios are selected as they cover most of the possible spread and extremes in hydrologic conditions, occurring in the RCM realizations. Table 13 shows the selected events and their hydrological characteristics.

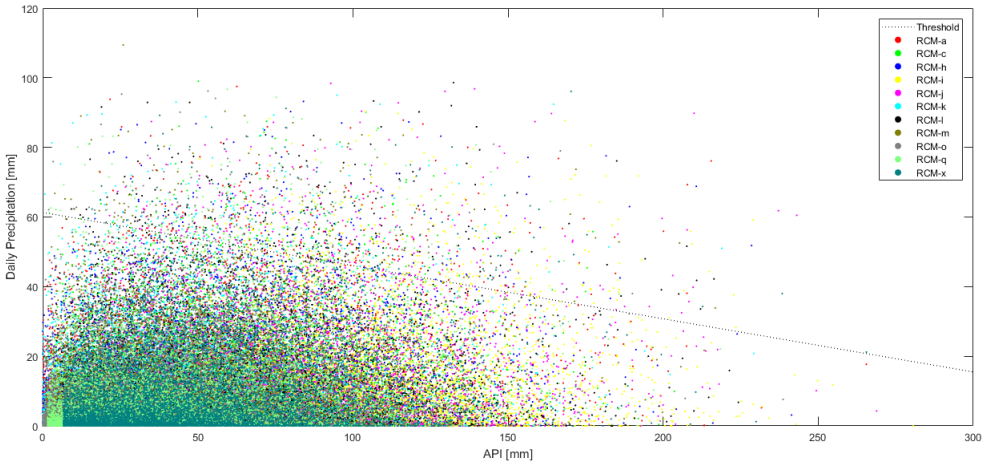

(a) Overview of daily rainfall and corresponding APIs for $n = 8$ from the RCM realizations and the computed threshold

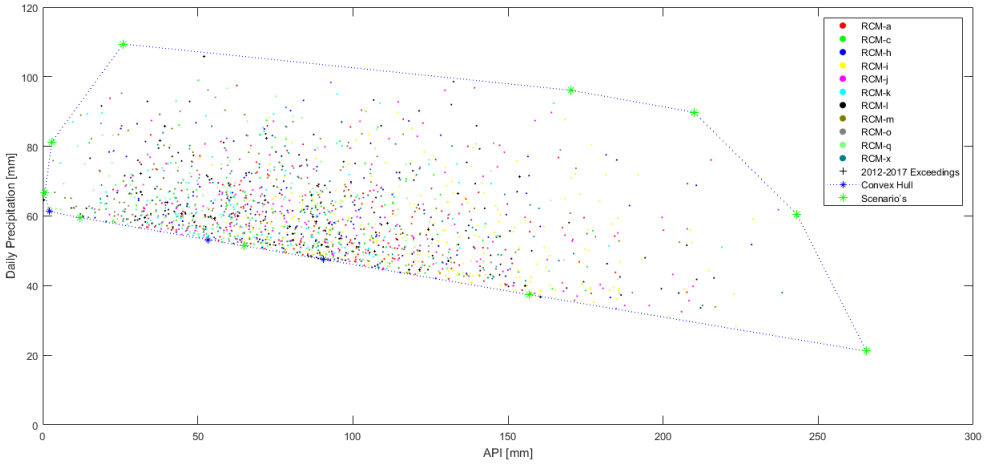

(b) Overview of daily rainfall and corresponding APIs for $n = 8$ from the RCM realizations and the selected scenarios

Figure 21

Table 13: Overview of selected scenarios and their hydrological characteristics.

RCM:	r_8**:**	r_7**:**	r_6**:**	r_5**:**	r_4**:**	r_3**:**	r_2**:**	r_1**:**	**API:**	**Precipitation:**	**Date:**
K	0.1 *mm*	0.1 *mm*	0 *mm*	0 *mm*	0 *mm*	0.1 *mm*	0 *mm*	3 *mm*	2.94 *mm*	81.30 *mm*	23-11-2019
K	0.4 *mm*	0.9 *mm*	0 *mm*	0 *mm*	0.1 *mm*	0 *mm*	0 *mm*	0 *mm*	0.71 *mm*	66.60 *mm*	05-03-2022
M	12.4 *mm*	0 *mm*	0.1 *mm*	6.3 *mm*	20.8 *mm*	12.9 *mm*	0.7 *mm*	3.9 *mm*	25.95 *mm*	109.40 *mm*	23-01-2024
I	5.8 *mm*	26.7 *mm*	17.2 *mm*	68.6 *mm*	25.2 *mm*	14.7 *mm*	15.5 *mm*	12.9 *mm*	156.87 *mm*	37.40 *mm*	24-09-2028
J	52.6 *mm*	46.2 *mm*	4.3 *mm*	1.5 *mm*	2.3 *mm*	6.4 *mm*	48.2 *mm*	96.8 *mm*	209.97 *mm*	89.80 *mm*	21-11-2032
X	4.1 *mm*	3.6 *mm*	36.7 *mm*	14.9 *mm*	27.2 *mm*	68.3 *mm*	7.8 *mm*	73.6 *mm*	170.35 *mm*	96.10 *mm*	18-12-2036
X	36.7 *mm*	14.9 *mm*	27.2 *mm*	68.3 *mm*	7.8 *mm*	73.6 *mm*	96.1 *mm*	34.3 *mm*	265.52 *mm*	21.20 *mm*	20-12-2036
M	12.9 *mm*	43.8 *mm*	9.7 *mm*	18.8 *mm*	58.5 *mm*	10.4 *mm*	4.8 *mm*	2.5 *mm*	64.93 *mm*	51.40 *mm*	27-10-2037
J	22.5 *mm*	12.8 *mm*	31.3 *mm*	25.6 *mm*	49.6 *mm*	47.5 *mm*	89.7 *mm*	61.8 *mm*	243.07 *mm*	60.50 *mm*	21-10-2038
K	0.1 *mm*	0 *mm*	0 *mm*	0.4 *mm*	15 *mm*	0.7 *mm*	3.7 *mm*	3.6 *mm*	12.10 *mm*	59.50 *mm*	31-12-2044

4.1.3 Mass Correlation

In figure 22 some similarities in shown trends for mass, API and rain can be distinguished. Especially the API and recorded displaced mass show a resembling trend, whereas the daily rainfall only little similarities to the trend of recorded displaced mass.

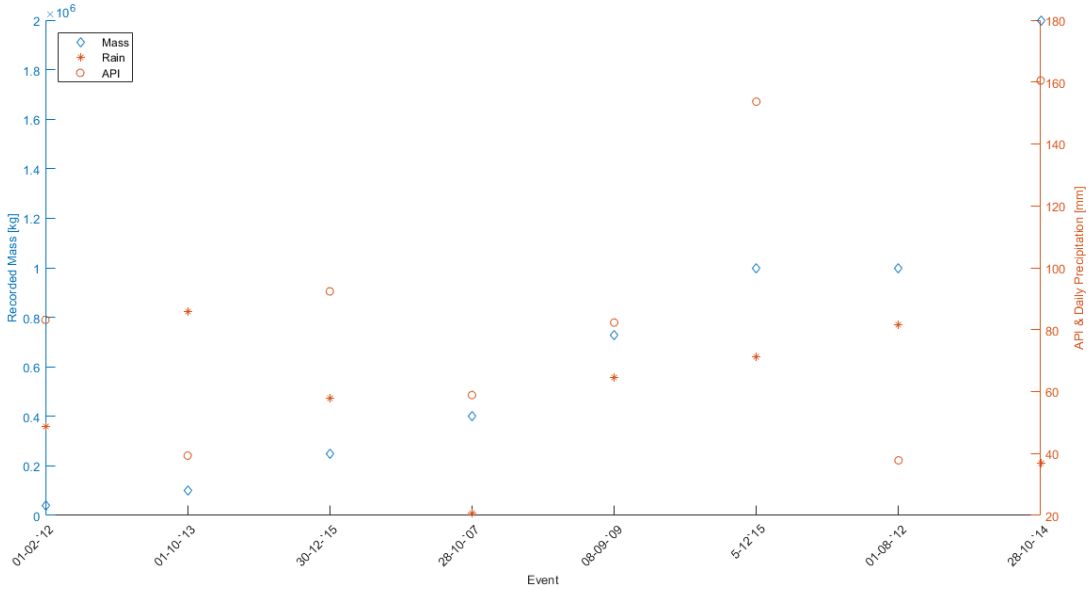

Figure 22: Correlation between mass, API and daily rainfall

Hypotheses were tested for linear correlation and linear rank correlation. As shown in table 14, the Pearson type correlation between daily rainfall and recorded displaced mass is rather negative. However, as $P_{val} > 0.05$, the hypothesis that the correlation is significant can confidently be debunked. Similarly, this is the case for the Spearman type correlation between daily rainfall and recorded displaced mass as well. A weaker negative correlation is found, whereas the p-value is even higher. Undoubtedly leading to rejecting the hypothesis of correlation. In the case of the API and recorded displaced mass, the rather high Pearson type correlation coefficient indicates a strong relationship. Moreover, the low p-values for n=8 and n=12 lead to conclude that the correlation between the API and recorded displaced mass is stronger and more significant with respect to daily rainfall and recorded displaced mass under increasing values of n. Even though the p-value would imply stronger and more significant relationship at n=12, for further analysis n=8 is applied, as this is

more in line with the previously discussed findings of Pennington et al. (2014); Berti et al. (2012); Ballantyne (2004).

Table 14: Correlation coefficients of different types, based on equations 3 and 4

Type:	Pearson		Spearman	
	Mass			
	P_ρ	P_{val}	S_ρ	P_{val}
Rainfall:	-0.1533	0.7170	-0.0359	0.9453
API($n = 4$):	0.6045	0.1124	0.1317	0.7605
API($n = 8$):	0.6465	0.0832	0.3114	0.4505
API($n = 12$):	0.7940	0.0186	0.5629	0.1539

4.2 Parameterization

4.2.1 Soil Depth

The initial soil depth computed for the area using 28 is shown in 23a.This soil depth serves as the initial condition within the soil production and transport module. Initially soils in the valley bottom range from as thin as $2m$ to an initial thickness of $10m$. Considering the hill slope, bare outcrops of bedrock to soils as thick as $6m$ can be observed. Furthermore, 9.2% of the soils are rankers.

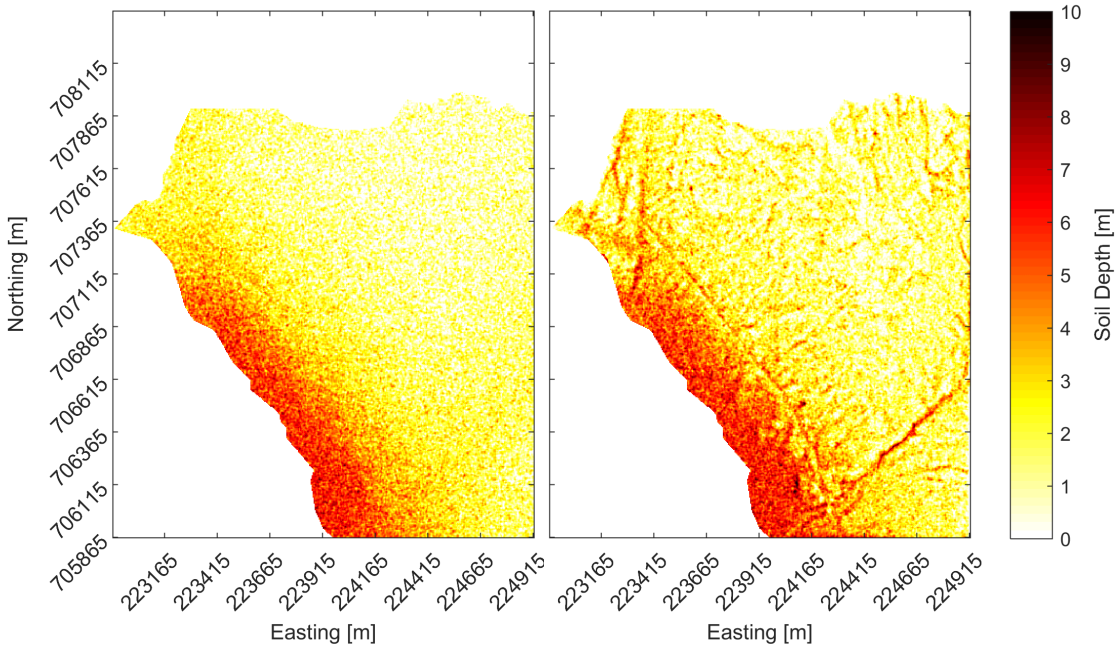

(a) Initial soil depth, using equation 28

(b) Soil depth after $1kyr$, using equations 32, 33 and 31.

Figure 23: Overview of soil development over time.

The resulting soil depth after $1kyr$ of soil production and redistribution is show in figure 23b. It is clear that material accumulates in the gullies on the hill slope and in the valley bottom. Furthermore, subsequent formation of bedrock outcrops occurs up slope. The calibration of parameter D_2 to 1.12, has increased the occupation of the hill by shallow soils to 12.27%. The realization, shown in figure 23b was used during the calibration process for CLiDE and for further analysis of the area of interest. In addition, figure 24 shows a cross-section of the area in a SW-NE orientation, which is

parallel to the slope inclination. The cross-section shows the effects of the correlated noise, applied to the calculated bedrock.

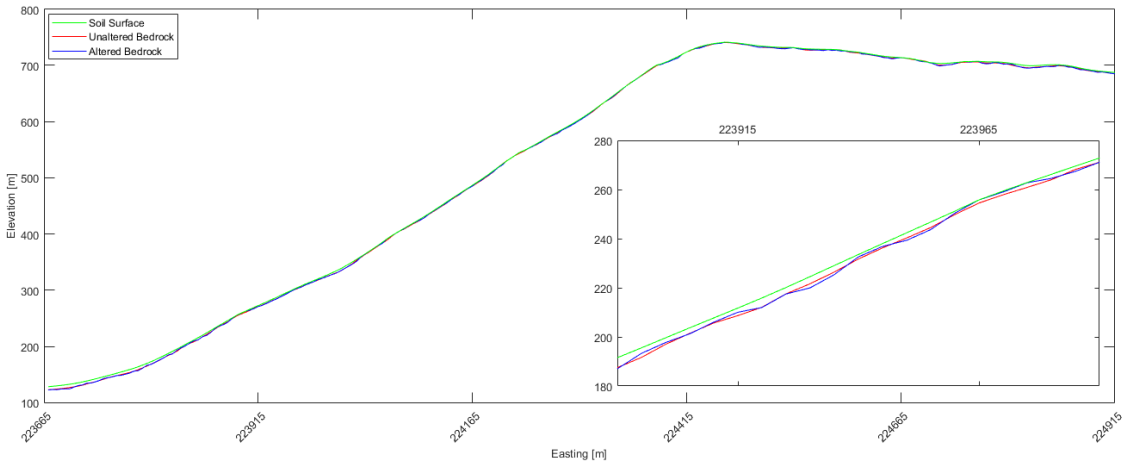

Figure 24: SW-NE transect showing the effects of noise application.

4.2.2 Soil Texture

Figure 25 shows the spatial distribution of the realized soil textures in the topsoil, 0 to 30 cm, including organic matter. Shown in figure 26 is the realization of the subsoil, in which organic matter exponentially decreases over depth. As a result of the applied methods, no clear patterns in the distribution of a soil textural class can be observed. The realized variation in percentage of the matrix is shown in table 15.

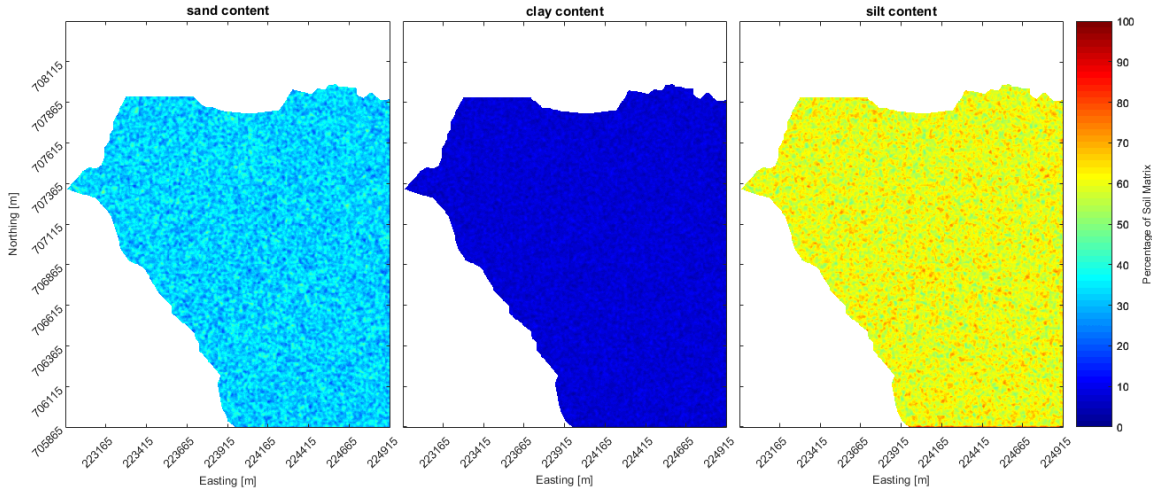

Figure 25: Realization of the topsoil texture used during this analysis, based on equations 36, 37 and 7.5% organic matter .

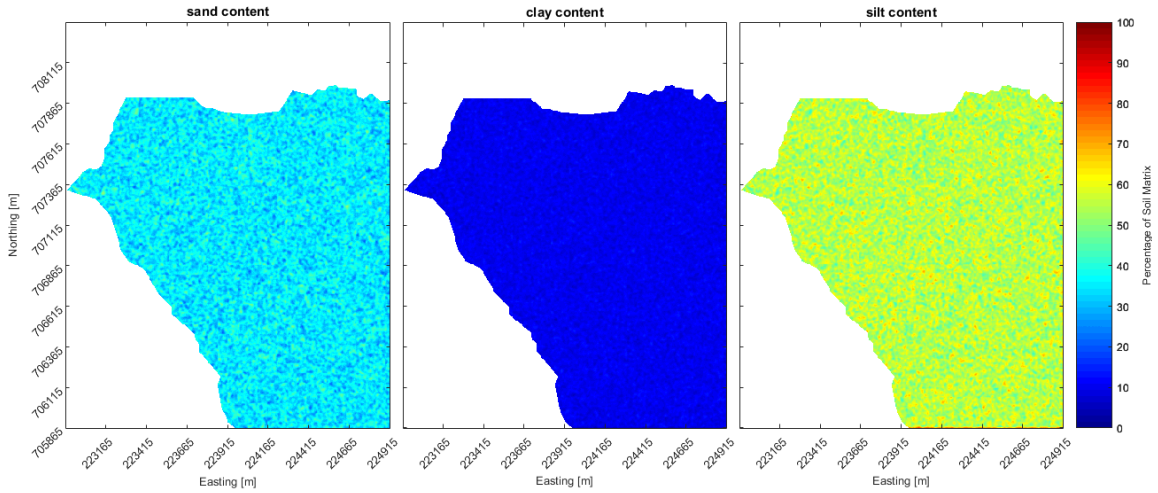

Figure 26: Realization of the subsoil texture used during this analysis, based on equations 36 and 37 .

Table 15: Maximum and minimum realized percentages of the soil textural classes, found in the study area

Soil Textural Class:	Minimum:	Maximum:
Sand:	12.53%	52.41%
Clay:	3.75%	15.26%
Silt:	36.81%	80.58%

As the figures indicate, strong heterogeneity in the spatial distribution of the soil textural classes is realized. Moreover the table shows that a strong heterogeneity in the numerical distribution occurs as well, resulting in wide variations of soil matrices.

4.2.3 Soil & Bedrock Properties

Figures 27, 29, 30, 31, 32 and 33 show the realizations soil properties that are used in the analysis. Note that the blank spots denote areas where either bedrock is present at the surface or where the soil thickness is not sufficient for the depicted layer.

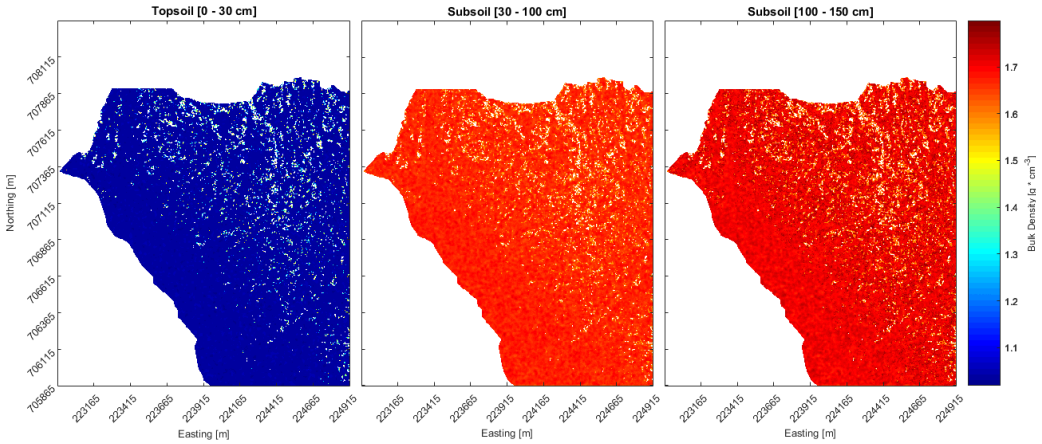

Figure 27: Realization of the bulk density used during this analysis, based on equation 38.

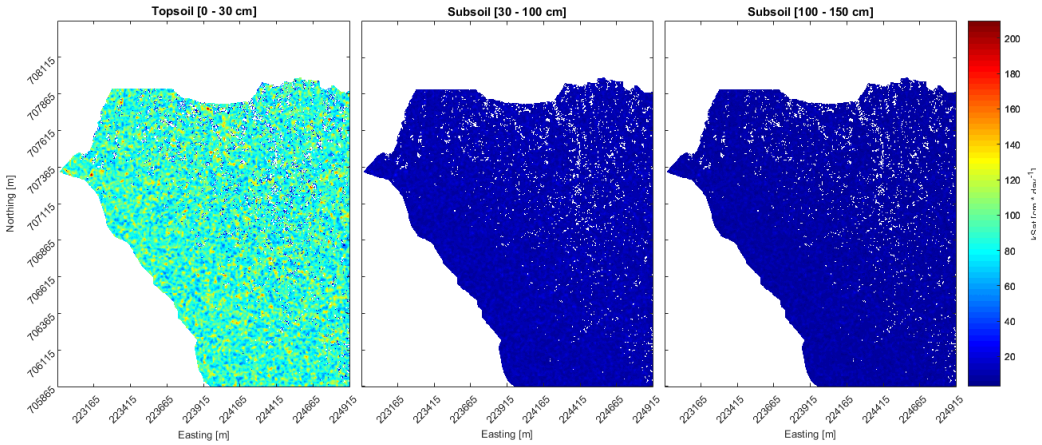

Figure 28: Realization of the saturated hydraulic conductivity used during this analysis, based on equation 39.

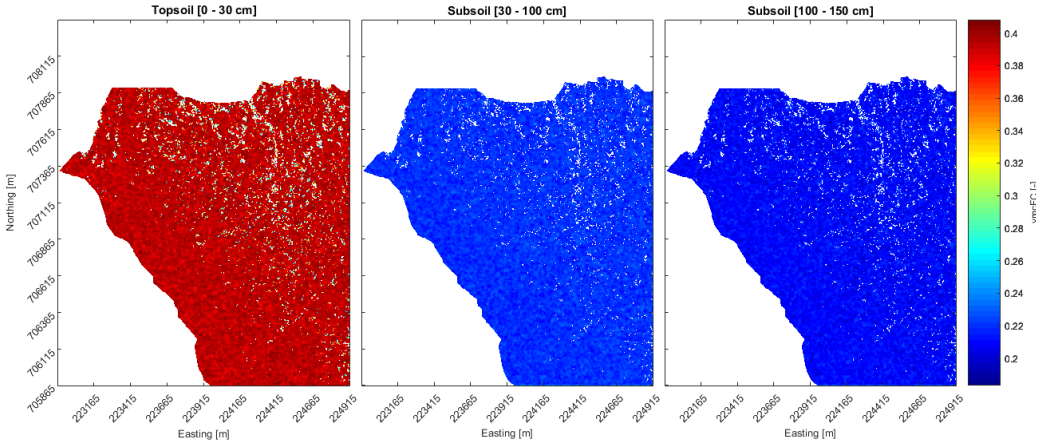

Figure 29: Realization of the volumetric moisture content at field capacity used during this analysis, based on equation 40.

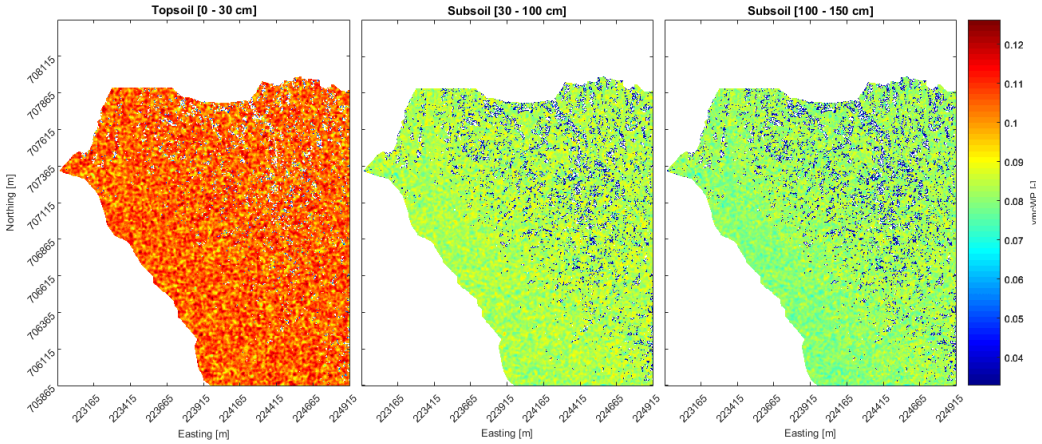

Figure 30: Realization of the volumetric moisture content at wilting point used during this analysis, based on equation 41.

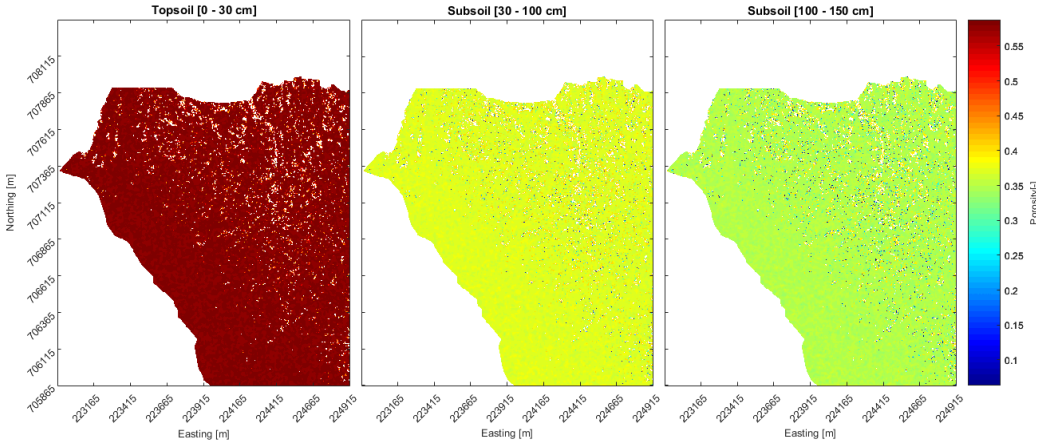

Figure 31: Realization of the volumetric moisture content at saturation used during this analysis, based on equation 42 (note that the volumetric moisture content at saturation is per definition equal to the porosity of the soil).

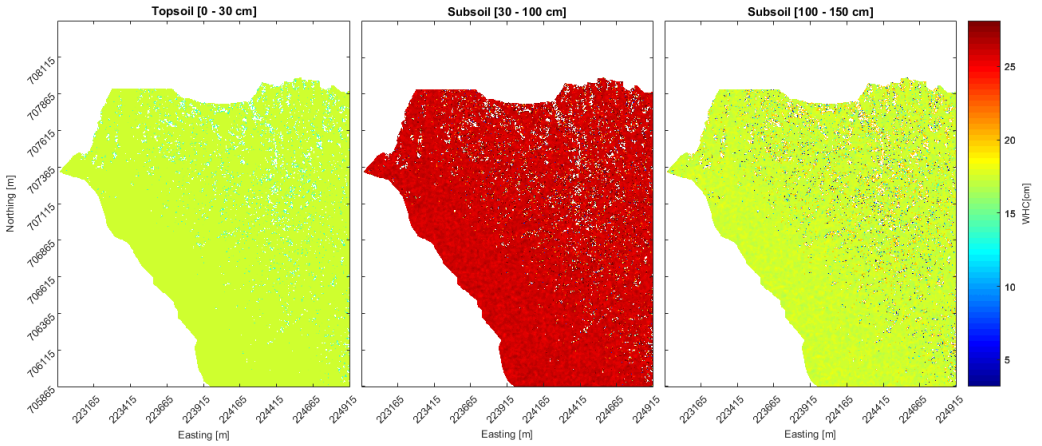

Figure 32: Realization of the water holding capacity used during this analysis, based on equations 41 and 42. Note that the water holding capacity is conditional to the thickness of the layer. Consequently, the water holding capacity depicted should be viewed in relation to the defined thickness.

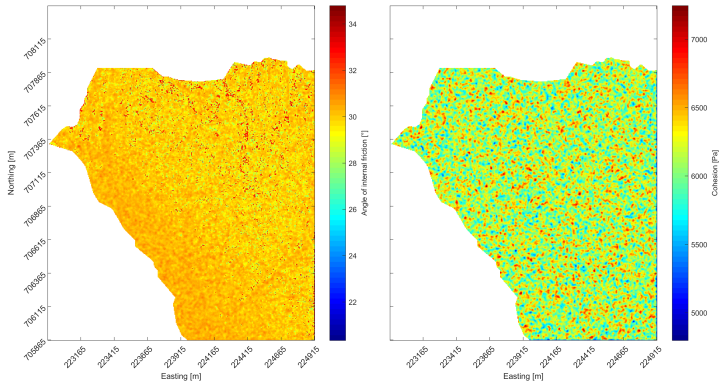

Figure 33: Realization of the internal friction angle and cohesion, used during this analysis, based on equations 44, 45. 46 and table 9.

When considering the soil properties, it is evident that the water holding capacities and conductivity decrease over depth as a result of decreased organic matter and lower porosity. This also implies an increase in bulk density. The friction angle shows some patterns, mainly at higher altitudes. This can mainly be attributed to bare bedrock, which is assigned the highest value observed in the study area. Contrarily, the cohesion shows no patterns as its origin lays only with the random distribution of the soil texture. In addition to the parameterization of the soil, the bedrock is characterized by a hydraulic conductivity of 0.001 mm d^{-1} and a specific yield of 0.34 mm (Heath, 1983; Morris and Johnson, 1967).

4.2.4 Initial Hydrology

Following the FAO standards for potential evapotranspiration (Allen et al., 1998) for temperate regions with annual mean temperatures around 10°C, a standard potential evapotranspiration of 1 mm d^{-1} is applied. For the hydrology of the soil type class 6 is opted in this study as it is mainly assigned to colluvium, loamy drift and coverloam, according to the classification of Boorman et al. (1995). This class is generally characterized by being unconsolidated, being microporous and experiencing bypass flow frequently. The results of the spin-up for the initial saturation of the bedrock showed that little drainage occurred from the bedrock. The observed decrease in groundwater levels was in the order of centimeters which can be attributed to the low conductivity and specific yield of the aquifer. Consequently, a saturated bedrock is used in the initial hydrological conditions.

4.2.5 SCIDDICA

Table 16 shows the parameterization of the SCIDDICA-module as used during the simulation of the scenarios selected in section 4.1.2.

Table 16: Parameterization of the SCIDDICA-module compared to the values calibrated by D'Ambrosio et al. (2003).

Parameter:	**Applied Value:**	**Value (D'Ambrosio et al., 2003):**
P_{adh}:	$0.01m$	$0.001m$
P_f:	$0.1m$	$0.1m$
P_r:	0.1	$1m$
P_{rl}:	$9m$	$0.6m$
P_{mt}:	$5m^2$	$3.5m^2$
P_{er}:	0.25	0.015

Evidently, most parameter differ an order of magnitude in their values. This is necessary as the values calibrated by D'Ambrosio et al. (2003) did not result in anticipated runout distances as they initiated extreme amounts of displacement and entrainment.

4.3 Mass Movement Simulations

From figure 34a it becomes apparent that the critical soil water depth is rather uniform but tends to increase downslope as a result of thicker soils and gentler slopes. Nonetheless, figure 34b shows that critical soil water depths are appearing more frequently in the areas below 500 m altitude in the centre of the slope. Moreover, the time series of the simulations, presented in the appendix, show that the majority of the source areas is situated below 500 m as well. This can be attributed to a small concave to convex shape of the bedrock, see figure 24. As the slope angle decreases, drainage slows down and water starts to accumulate. In addition, the strong confinement of these critical zones and their propagation upslope already indicate that gully formation and subsequent drainage patterns play a vital role in triggering mass movement in the study area. However, the occurrence of some hotspots at higher altitudes suggests that subsurface drainage patterns and accumulation in bedrock hollows can potentially mobilize material.

Subsequently, figures 34c and 34d show the average erosion and deposition and its variance respectively, resulting from the simulated scenarios. Similar to the observed drainage patterns, debris sources and subsequent runout of mobilized material is largely restrained to gullies. Furthermore, zones with high variance indicate that either only extreme events affects these zones or that a zone is experiencing highly variable amounts of erosion and/or deposition. For instance, areas that are unaffected during less extreme events are heavily eroded or serve as source areas during more extreme events. This is clearly exhibited in the time series of the simulated scenarios, included in the appendix. Additionally, when considering the complete time series of the simulated events with respect to the corresponding daily precipitation, it is evident that different precipitation patterns during antecedent days of similar absolute amounts of water can mobilize different zones or alter runout paths in the study area. This effect is clear when comparing the simulations for 21-11-2032 and 18-12-2036. Although they have similar displaced masses and precipitation, longer runout paths can be observed in the 18-12-2036 scenario, despite its lower API. Examining the precipitation pattern and soil water depths of simulations 23-01-2024 and 27-10-2037 (Appendix figure 49) is another example of how the antecedent precipitation pattern can influence the spatial distribution of potentially mobilized material. The antecedent precipitation is concentrated in the first 5 days for both scenarios. However, the higher peak precipitations in the 27-10-2037 simulation caused more water to drain downslope through the soil. Subsequently, the identified source areas are relatively low due to accumulation and stagnation in bedrock irregularities.

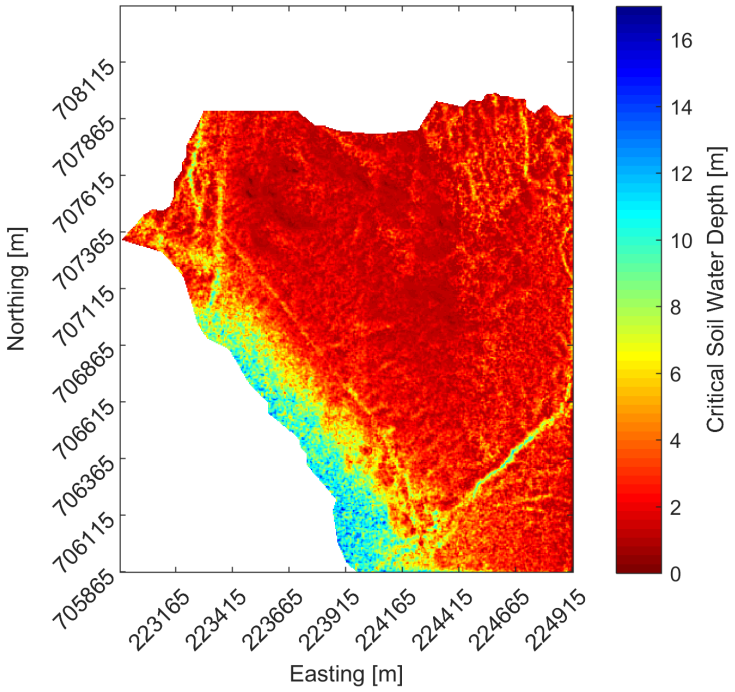

(a) Critical soil water depth, derived from the infinite slope model.

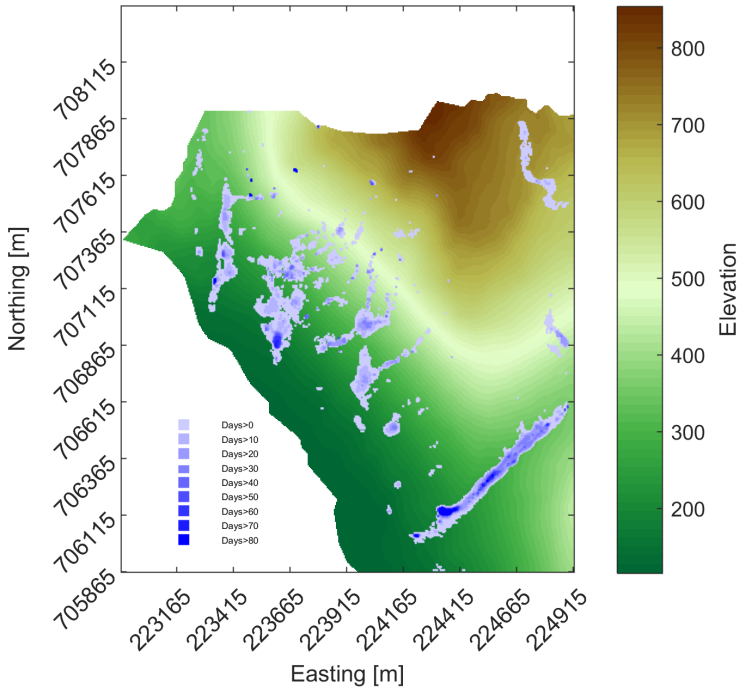

(b) Amount of days during which the critical soil water depth is exceeded during 90 simulated days.

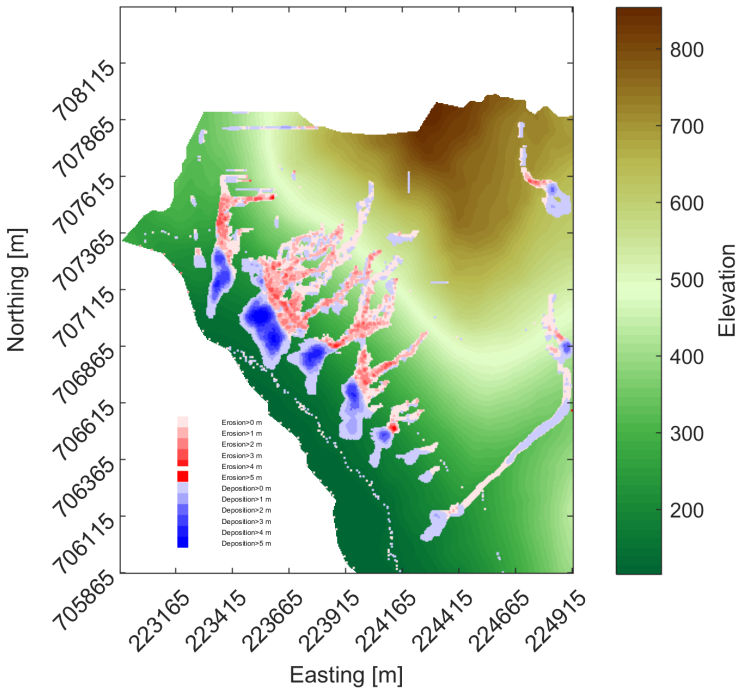

(c) Average erosion and deposition, resulting from the simulated scenarios.

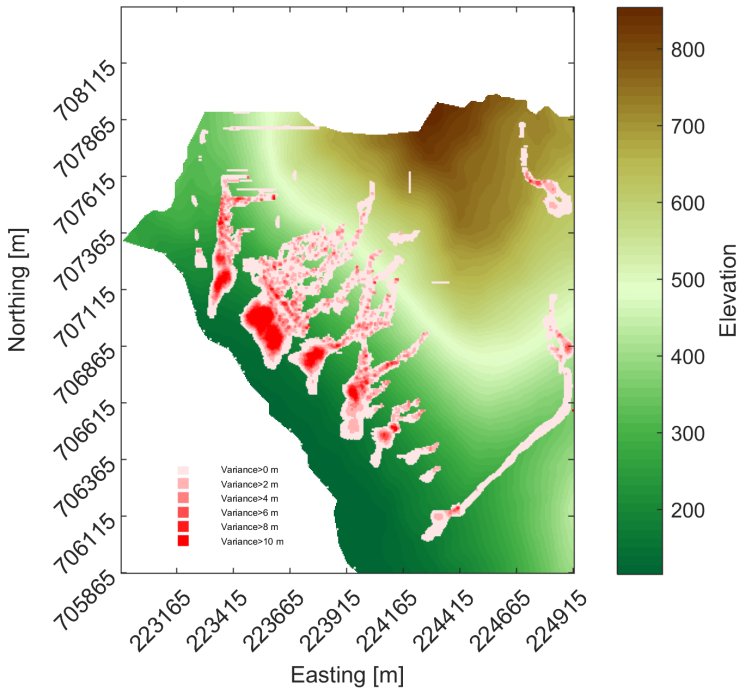

(d) Variance of erosion and deposition, resulting from the simulated scenarios.

Figure 34: Summary of the simulated scenarios.

Figure 35 shows similarities to the historical events depicted in figure 22. Both graphs indicate a strong correlation between the API and the amount of displaced mass, whereas the daily precipitation seems to negatively influence the amount of displaced mass. However, it is obvious that both correlations are stronger in the simulated scenarios when compared to the historic events and their associated hydrological conditions.

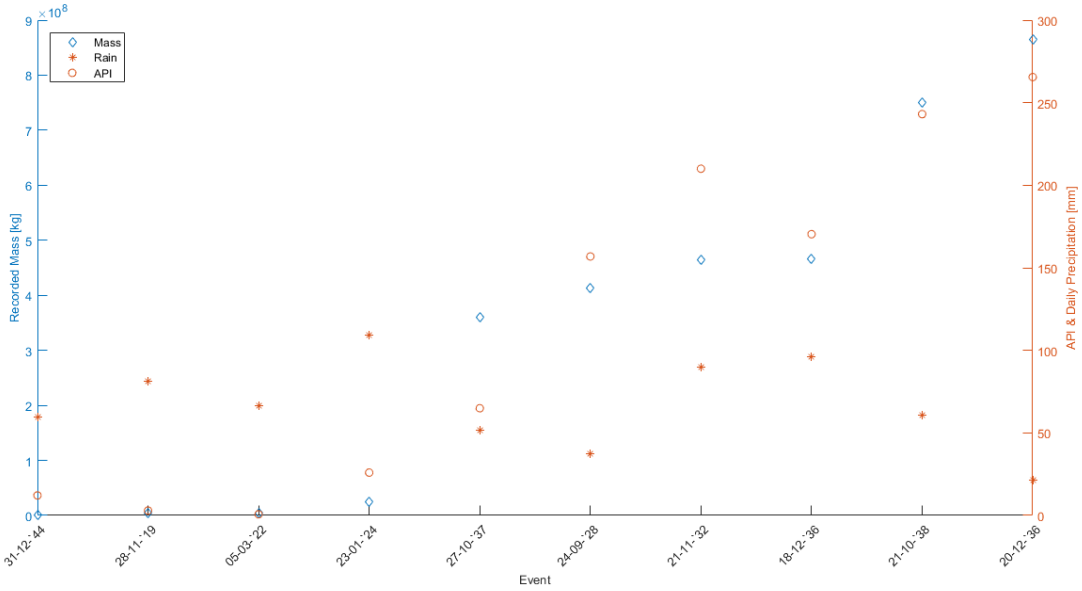

Figure 35: Correlation between mass, API and daily rainfall for the simulated scenarios.

These findings are confirmed by the derived correlation coefficients, as presented in table 17. This suggests either that in the simulations the both the influence of the antecedent precipitation as well as the direct precipitation is overestimated or that effects tampering mass movement hazard are underestimated.

Table 17: Correlation coefficients of different types, based on equations 3 and 4

Type:	Pearson		Spearman	
	Mass			
	P_ρ	P_{val}	S_ρ	P_{val}
Rainfall:	-0.4862	0.1542	-0.2	0.5835
API($n = 8$):	0.9692	0.0	0.9394	0.0

5 Discussion

The aim of this study was to evaluate how mass movement at the Rest and be Thankful pass will be affected by climate change. In a temporal sense, it was aimed to establish a hydrological threshold based historic events at the pass, which was subsequently applied to precipitation scenarios originating from the UKCP, realized by 11 configurations of the HadRM3 regional climate model. Additionally, the principle hydrological driver for mass movement, either the daily- or antecedent precipitation, and recurrence time were identified for these scenarios. Furthermore, the main source areas for mass movement were identified and it was assessed how their location is influenced by antecedent precipitation patterns. To do so, a selection of day series was simulated in the CLiDE modelling framework to monitor the hydrological conditions and possible mass movement runout during periods in which mass movement is expected, based on the established thresholds.

5.1 Hydrological Analysis

5.1.1 Hydrological Thresholds

The hydrological conditions that are able to facilitate mass movement at the Rest and be Thankful Pass strongly depend on the amount of days accounted for in the API. An increase in the amount of days accounted for in the API yields stronger correlation coefficients between the API and the displaced mass in the historical events. However, as shortly introduced in section 4.1.1, the intersect with the y-axis was considered essential in evaluating the applicability of either n=4, n=8 or n=12, as these are the daily precipitation values that should activate mass movement without any antecedent precipitation. These values are 71.2 mm, 61.3 mm and 57.1 mm and have associated decay factor based on the API of approximately 0.30, 0.15 and 0.1 respectively. In light of the findings of Ballantyne (2004), stating 24 hour thresholds of 60 mm to 80 mm initiating mass movement, this leads to the assumption that $n = 4$ $n = 8$ and the corresponding threshold seem more representative for the study site. Moreover, the results of Pennington et al. (2014); Chen et al. (2018) state strong correlation between mass movement in these environments for antecedent precipitation based on $n = 7$. Hence, $n = 8$ and the associated formulation of the threshold line, T, were considered representative for further analysis the study site. In addition to the application of the threshold to calculate recurrence times for the hydrological forecasts from the UKCP, these results can be considered when designing low-demand early warning systems which can easily identify hazard based on weather forecasts. Moreover, this method can easily be applied over a number

of temporal scales (Dahal and Hasegawa, 2008) and has been applied widely in numerous environments (Glade et al., 2000), which emphasizes its efficiency.

When $n = 4$, $n = 8$ and $n = 12$ are applied to segregate the mass movement events from the continuous precipitation dataset based on the daily precipitation and the API, it is evident that the recorded mass movement events can be separated properly from the other data, as few other dates meet the established criteria. However, the mass movement event from October 2007 fails to meet the established threshold in all variations of n. A possible explanation for this could that the closest weather station from 2007 until and including February 2012 was approximately 10 kilometers away. Due to the localized nature of precipitation and the rugged terrain surrounding the study site, meteorological differences could be substantial on small spatial scales (Cosma et al., 2006; Faurès et al., 1995). On the contrary, the hydrological conditions considered sufficient for mass movement are met several times without any recorded movement. Namely in October 2014 and August 2012. For October 2014 the occurrences with threshold exceedance but without mass movement can be explained by the fact that rainfall intensities were lower that day compared to the mass movement occurrence on October 28th (Sparkes et al., 2017). Considering the occurrence of threshold exceedance but without mass movement in August 2012, these particular circumstances occurred posterior to the mass movement that month. Consequently, it is plausible that material that, under these circumstances, would have been mobilized, was already redistributed by mass movement earlier that month.

Though methods of deducting the decay factor, applied in the calculation of the API, from regional hydrographs exist (Klaassen and Pilgrim, 1975; Smakhtin and Masse, 2000), these are not applied as this falls out of the scope of this research and requires a gauged catchment for calibration purposes, which is not available for the study site. Therefore, the decay factor is found by iteration. Additionally, segregation of the data by an exponential or polynomial is possible as well. However, the spread of the very limited data available would still cause those functions to form a relatively straight line. This is due to the rather small difference in daily precipitation of the two lowest points that indicate mass movement. Moreover, the limited amount of data points would initiate errors, mainly when dealing with very low and very high values for the API as the scarcity of data is most distinct here. Moreover, extension of the available data would greatly improve the significance of the conclusions that can be attributed to the derived correlation coefficients. Hence, data availability regarding mass movement events and the associated precipitation patterns will significantly improve establishment of threshold values for the Rest and be Thankful pass.

Furthermore, little information is available regarding the morphological characteristics of the mass movement events at the pass, such as failure plane depth and the initial type of mass movement. Even though the study experiences mostly shallow mass movements their hydrological triggering mechanisms may differ significantly and a threshold based on daily precipitation values might overlook events which are induced by high intensity precipitation. Moreover, when putting this in perspective of the statement by Van Asch et al. (1999) that finding one threshold for mass movements initiated at varying failure plane depths is very unlikely, it is clear that regardless of the method, thresholds can only be extrapolated to nearly identical situations. Nonetheless, to be able to identify hazard, for instance in early warning systems, the least amount of precipitation and antecedent precipitation should be applied.

When the defined threshold for $n = 8$ is applied to the continuous dataset, the occurrences of threshold exceedance without any mass movement show that meeting the established hydrological criteria is not the only factor in the identification of mass movement hazard. This suggests that the availability of mass and rainfall intensity are likely to have a considerable impact. However they are not accounted for. Determining the availability of mass is rather impossible without extensive field studies. Although, the rainfall intensity could have been determined, the rainfall regimes from the predicted hydrological forecasts are realized on a daily scale. Consequently, the defined threshold should function on the same temporal scale. Aside from discrepancies in mass availability and precipitation regimes, the lack of recording of mass movement in the area might be influential. Not all mobilized material will interfere with human activities. This might leave some of these events unnoticed and thus unconsidered in this research.

5.1.2 Hydrological Forecasting

As reported in figure 17, the found recurrence time for data available for the Rest and Be Thankful pass is low for the hydrological conditions, likely of facilitating mass movement, when compared to the recurrence times originating from the hydrological forecasts. Only four hydrological forecasts yield lower recurrence times than the observed 67 days for the historical data. This result indicates that the hydrological conditions that are able to induce mass movement will occur more frequently under forecasts i, a, l and j. The remaining forecasts show various extents of declination, which suggests that a declining trend is more likely.

When examining figure 20, depicting the independent recurrence times, the closer the the daily precipitation and API are in their distribution of recurrence times, the

more mass movement in the area can be considered driven by antecedent precipitation. This shows that mainly RCM forecasts i, a and j are largely driven by antecedent precipitation. RCM forecasts q, m and o show to be mainly governed by daily precipitation, whereas the remaining forecasts c, h, k, l and x show less expressive differences. Additionally, the positive correlation between antecedent precipitation and displaced mass observed at the pass and the calculated recurrence times, which is in line the findings of Iverson et al. (2011) and Freer et al. (2002) on the effects of antecedent precipitation on material entrainment, suggest that under the forecasts i, a and j mass movement hazard at the pass will likely increase, whereas the other forecasts tend show less frequent hazard when compared to the historical data. These results emphasize the fact that future mitigation and adaptation measures should account for the hydrological regimes that are associated with likely climate change scenarios.

The ANOVA-test on the distributions of the APIs, associated with mass movement events, indicate similar results. although they are not significant, the results suggest a decline in hazard due to lower mean ranks values for the API for six out of eleven forecasts. Namely forecasts k, l, m, o, q and x. Additionally, the results of the ANOVA-test on the daily precipitation associated with mass movement events show that seven out of eleven forecasts show increased mean ranks values. Namely forecasts h, k, l, m, o, q and x. This suggests that under these forecasts, mass movement hazard will decrease as they are more driven by daily precipitation rather than antecedent precipitation with respect to the historical data. When evaluating the significant differences of the APIs, a smaller spread can be observed for the recorded datapoints. Contrary to the precipitation spread, the mean ranks of the datasets are largely reversed. This can be attributed to the climatological differences in the simulations, which define the precipitation regimes. These climatological differences also cause the APIs to show a somewhat stronger spread and thus more significant differences, implying stronger differences in rainfall regimes rather than daily precipitation.

The general reduction in mass movement hazard in the majority of the forecasts coincides with drying of the study area and subsequent lowering of the observed APIs. This is supported by trends that have been observed for other hydrological applications using the UKCP datasets (Christierson et al., 2012; Sanderson et al., 2012; Kay and Jones, 2012). The main findings of these studies additionally emphasize the aggravating hydrological differences between the seasons as shown in figure 36.

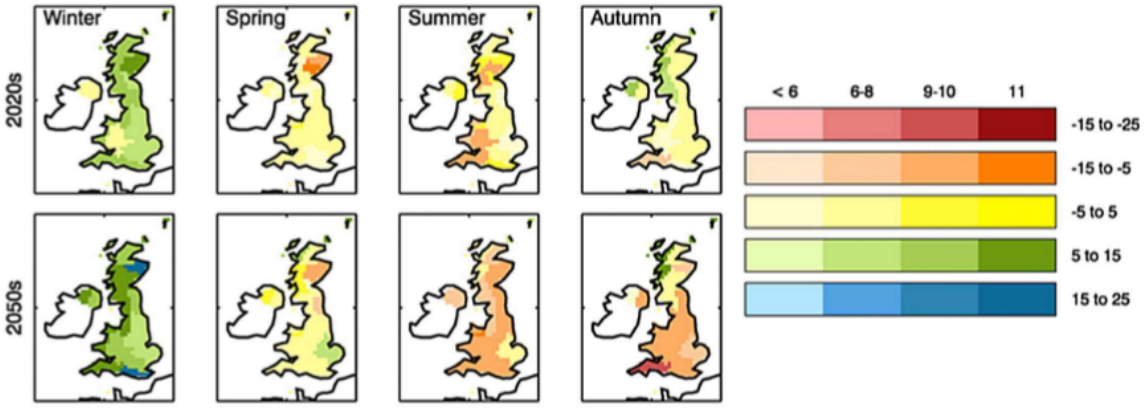

Figure 36: Projections for the percentual change in mean runoff up to the 2050's compared to 1961-1990, following from the UKCP. Note that the four possible shadings of the colour indicate the extent of agreement between the RCM realizations and the multimodel mean. Adapted from Sanderson et al. (2012).

Specifically for the study area, figure 36 depicts that, apart from winter, all season experience drying under most hydrological forecasts. This will not directly imply that mass movement hazard should decline in this period. As showed by Sanderson (2010), extreme precipitation events will clearly increase, especially during winter. For summer periods the outcomes are less certain. However the suggestion is made that precipitation will get more concentrated during the summer, implying more extreme events but with a lower recurrence time Chan et al. (2018). Therefore, even when the recurrence time of hydrological conditions meeting the established threshold might decrease, the severity of mass movement might still increase as a result of higher rainfall intensity, which is currently not considered in this study, over the summer. In addition to the changing precipitation regimes and its aforementioned implications, prolonging droughts can have significant effects on slope stability. As discussed by Chertkov (2002) and Morris et al. (1992), extensive drying of soil can alter its hydrological- and structural properties thoroughly, causing preferential flow through formed fissures and cracks; additional driving force through water accumulation in fissures; and facilitation of potential slip surfaces. As emphasized by Van Asch et al. (2009), flow through fissures can be essential in identifying mass movement hazards. Even though the occurrence of large fissures is not expected, microstructures can have similar effects (Sun and Cui, 2018) and thus can be enhancing mass movement hazard as a consequence of drought.

The wide spread depicted in figures 18 and 19 for the 2007-20017 time series, when compared to the hydrological forecast, limits the possibilities of drawing strong

conclusions on strong differences between forecasts and historical data as little significant results are observed. This can possibly be attributed to large storms such as Desmond and Frank in 2015, who were both initiators for threshold exceedance and subsequent mass movement occurring in the study area (Sparkes et al., 2017) and are included in the historical data. Consequently, a significant portion of the limited amount data points likely originates from rather extreme events, either by events including high APIs or by events concerning massive downpours. As shown in figure 16, the dataset from the newly installed station at the Rest and Be Thankfull pass contributes less to the spread as all major outliers are mainly the datapoints obtained from the old station. This could imply that the spread and average, based on merely the Rest an Be Thankful station, would be lower.

Even though using the convex hull of the datapoints for the selection of the scenarios is highly effective for the inclusion of a wide spread in combinations of antecedent precipitation and daily precipitation, this criterion does not account for any other characteristics that might influence the further analysis such as the spread of precipitation over the days accounted for in the API. This limits the comparability, based on the antecedent precipitation regime, of the selected events. Consequently, effects of antecedent precipitation regimes on mass movement hazard could benefit from the analysis of the effects of artificial regimes. Furthermore, this method selects datapoints regardless of their temporal spread. This results in the selection of both 18 December 2036 and 20 December 2036, which are both very extreme datapoints. Consequently, the simulation of the second event, preceding the day of interest, already includes a major event. Although both events experience relatively different amounts of antecedent and daily precipitation it is questionable if the interplay between these two events can considered representative for dual events of smaller magnitude.

5.2 Mass Movement Simulations

The simulations of the mass movement events, selected from the hydrological forecasts, show that mobilization of material mainly occurs in areas between 300 and 500 metres altitude. Two major causes are identified, which cause the dominant source areas to be largely restricted to this zone. Firstly, small concavity-convexity transitions can cause water either to stagnate in the convex hollows or to be forced through thinner soils, as shown in figure 37 b. Both processes are likely to increase pore pressure and cause subsequent slope instabilities. Secondly, the confinement of water by the present gullies and the coinciding subsurface drainage channels contribute to the concentration of water, as depicted in figure 37 a, and the ensuing triggering of mass

movement in this zone. Moreover, oversteepening of gully sidewalls and their resulting collapse, yields additional sources for erosive processes, including mass movement (Istanbulluoglu et al., 2005).

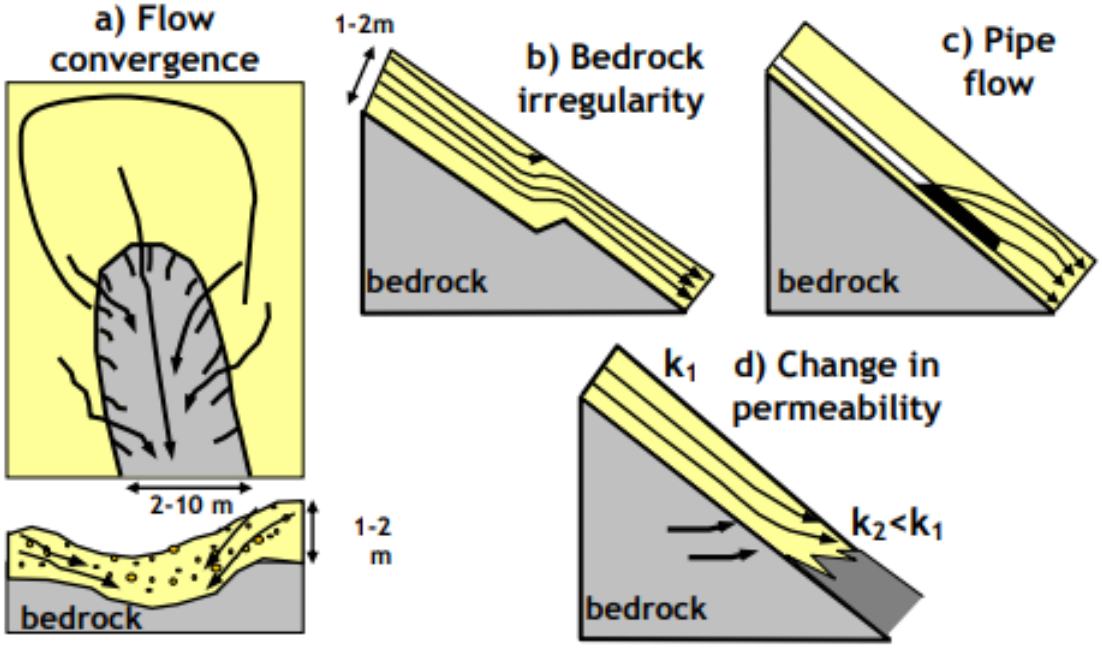

Figure 37: Overview of the main causes of mass movement through surface and subsurface flow on hill slopes covered by shallow soils. Adapted from Crosta and Frattini (2001).

Furthermore, the simulations suggest that the spatial distribution of dominant source areas is influenced by the precipitation patterns which mobilize them. Peak precipitation in the first half of the antecedent regime resulted in mobilization in the aforementioned zone between 300 and 500 metres altitude, whereas later peak precipitation in the antecedent precipitation regime, combined with an API well above 200 mm, mobilizes material above this zone as well, up to 800 metres. Under such precipitation regimes only limited drainage can occur and the subsequent saturation of the sediment can trigger mass movement. Hence not only the effects of antecedent precipitation on the amount of mobilized material should be emphasized (Freer et al., 2002), antecedent precipitation regimes should be considered, as they are influential in mobilizing different sources areas, as discussed by Ng et al. (2001) and by Tsai (2008). Consequently, wetter climate change scenarios, which will experience higher APIs, are likely to mobilize more material further upslope than is currently the case

at the Rest and be Thankful pass.

These findings can contribute to the cost-effective implementation of various adaptation and mitigation practices. Especially environmental engineering practices, such as revegetation, barrier placement and the installation of early warning systems McQuaker et al. (2014); Bainbridge et al. (2018); Rayner and Nicoll (2012), can benefit significantly from the identification of the main source areas. When viewed in light of the hydrological forecasts used in this study and the found implications of wetter climates for source areas, precautionary measures can be taken when the expected implications of climate change for the Rest and be Thankful pass get more indisputable through the improvement of climatological models. Furthermore, the results could be utilized to bridge the gap between studies that focus on different components of mass movement hazard such as: direct observations of the Rest and Be Thankful pass and quatification of specific events (Sparkes et al., 2017; Bainbridge et al., 2018; Balzano et al., 2016); the implications of climate change on hydrological trends in the United Kingdom (Christierson et al., 2012; Murphy et al., 2007, 2009); and adaptation and mitigation practices (Macklin, 2013; Rayner and Nicoll, 2012; McQuaker et al., 2014).

Within this study, the landscape development in between the simulated events and the run out of previous simulations is not accounted for in the subsequent simulation. Studies from Brayshaw and Hassan (2009) and Whipple and Dunne (1992) indicate the importance of channel avulsion through past events for the future flow paths. However, as established from the results and literature, climate and thus hydrology are highly influencing such processes. As the simulated scenarios are the extremes originate from different realizations of possible climate projections, they all have differing precipitation patterns and thus different landscape dynamics. Hence, the output from one simulation is not a suitable starting point for the subsequent simulation. Therefore, the simulations should be regarded independently and their implications of anterior events cannot accounted for. In a similar manner, the accumulation of material in the gullies during the spin-up of the simulations, may cause overestimation of soil depth in these gullies. As a consequence, large amounts of material can easily entrained due to the accumulation and large grid size.

From a hydrological perspective, the infinite slope model might not be an accurate predictor for one of the dominant mass movement types, namely debris flows. The initiation of debris flows is not necessarily attributed to groundwater level rise. However, initiation largely depends on surface runoff that entrains material following high intensity rainfall peaks (Van Asch et al., 1999; Kean et al., 2013). Consequently, mobilization and entrainment of material resulting from high intensity precipitation, is currently overlooked. However, as the hydrological forecasts are on a daily basis,

accounting for rainfall intensities would have required additional downscaling techniques. Although this might have considerable advantages for the identification of area that are prone to mass movement hazard, CLiDE does not allow for precipitation input other than daily. Consequently, temporal dynamics on smaller scales cannot be accounted for.

The initial hydrological conditions are assumed to be equal in all simulations. This narrows down the amount of factors that could possibly influence the simulation outcome, which allows for a valid comparison between the simulated mass movement events. However, this also imposes disregarding several climatic circumstances that could be influential. Especially the soil moisture deficit, near soil surface storage and potential evaporation, will be effected by changing meteo-hydrological trends in the Scottish Highlands (Thompson, 2012; Brown et al., 2011) and could influence mass movement hazard. However, these implications vary strongly among the scenarios Hence, accounting for these changes would imply substantially longer simulations and a more segregated approach with respect to the different scenarios would be beneficial.

5.3 Limitations of CLiDE and its Implications

As the CLiDE modelling framework is merely an approximation of reality, various components, that are important for the analysis of mass movement hazard, are not sufficiently covered. In addition to those influential in the evaluation of the research questions, as covered in section 5.2, other important factors and their implication are discussed in this section.

A factor that could improve the simulation is the interaction between cells in terms of load redistribution following failure and subsequent restabilization through lateral bonds with adjacent soil columns. As shown by Fan et al. (2015), Fan et al. (2016) and Lehmann and Or (2012), the interaction between soil columns is key is sudden releases of mass on slopes through progressive failure of adjacent cells. This could reduce the overestimation of source areas that originates from the application of the infinite slope model. Moreover, incorporation of this method might prevent premature mobilization of material during the simulations (as presented in the appendix). These studies show that such mechanisms have a strong impact on the timing of slope failure. The issues regarding timing are reflected clearly in the time series shown in the appendix as it becomes apparent that the simulations generate untimely mobilization of material. It should be noted that some of the depicted events contain antecedent days that on themselves should generate mass movement according to the criteria established in this study. Nonetheless, similar errors are observed during simulations in which the antecedent days not include such events, indicating that this cannot fully be attributed to such causes. Besides the lateral effects, premature mobilization could partly originate from the errors resulting from the previously discussed lumped variables that are input for CLiDE. Such disparities might combine underestimation of the internal friction angle with underestimation of the specific yield, resulting in a very susceptible cell.

Although the drainage and runout patterns of the simulations coincide well, as expected, with the gully patterns, prudence is required when considering the resulting deposition. The calculated deposited masses show little resemblance with the values shown in figure 22. As indicated in section 4.3, the material deposited due to mass movement in the area can accumulate to over 10 metres thick. When related to the recorded mass movements with the similar APIs, as shown in figure 22, the simulations clearly overestimate the deposited material by one or two orders of magnitude throughout the simulations. This discrepancy can attributed to various causes. Firstly, the grid size causes one grid cell to comprise 25 m^2, which can have serious implications for the analysis of the study area. For instance, mobilization of one cell with an average soil depth of 1 metre would already cause 40 tonnes of material to be displaced. When compared to the amounts of mass shown in figure

22 it becomes apparent that this amount of mass already represents large portion of the material deposited on the road during some of the historical events.

5.4 Limitations of CLiDE's Parameterization and its Implications

Similar to the CLiDE modelling framework, its parameterization and the associated methods are approximations of reality, which imposes discrepancies when attempting to simulate natural systems. The most important limitations, discrepancies and their implication are discussed in this section.

5.4.1 Soil Depth

The bedrock depth calculated in this study yields a fair representation of the average soil depth on the hill slope if compared to the findings of Rayner and Nicoll (2012) and Bown et al. (1982). Both denote a strong decrease in soil depth upslope and identify numerous areas where soils are not deeper than 50 cm. Furthermore, the increase in extent of rankers to 12.7 % after the spin up is a fair result as they are predominantly established above 400 metres altitude, in line with statements by Rayner and Nicoll (2012). However, based on the comments made on valley fill accumulation in similar environments by Ballantyne (2002) and Edwards and Whittington (2001), the soil thickness in the valley bottom is slightly underestimated, as sedimentation rates of 4.5 m over the last 8000 years would imply that thicker soil should be expected. Nonetheless, the valley bottom is not considered critical within in the analysis of mass movement hazard in the study area.

The application of equation 29 to the calculated initial soil depth effectively mimicked some of the ruggedness of the underlying bedrock, as would be expected following Lowe and Walker (1997) and Ballantyne (2002) notes on the implications of glacial scouring for the abutting bedrock. However, a pitfall lays with the spatial scales of the localities such as gullies, bedrock ruggedness, outcrops and topographic hollows. These features can appear at a variety of scales, ranging from tens of centimetres to tens of metres, whereas the available digital elevation model had a grid spacing of 5 metres. Although, the application of noise may produce are more representative soil thickness, it is merely one of many representations of the bedrock and, more importantly, the noise works on a larger spatial scale than localities would normally occur. Consequently, features with a smaller spatial extent might be overlooked or underestimated, having implications for the redistribution of water and material through the system.

Considering the soil depth after a spin up time of 1000 years, it is evident that the gullies in the study area allow for colluvial and alluvial avulsion, predominantly in low laying areas, such as the south-eastern channel. However, these accumulation zones do not accurately represent the redistribution of sediment in the study area. Both of these accumulation zones are larger drainage channels of their respective watersheds, the south-eastern channel being the Croe Water, draining into the valley. As continuous fluvial erosion is not accounted for in the soil module, the avulsion of these areas is not in line with the field circumstances. On a smaller scale, similar processes occur in gullies, causing the accumulation of material up slope of the road, causing thick soils in topographic hollows and the accumulation of potentially unstable material. As the transport of material in soil module is based on the erosive diffusivity, it is unable to deal with transport on spatial scales larger than the grid size and temporal scales smaller than the timestep taken. Even though the proposed value for erosive diffusivity should account for frequent mass movement, it is unable to reactivate gullies once they are have experienced severe accumulation.

5.4.2 Soil Texture

When considering the soil texture, Balzano et al. (2016) apply $T_{f,sa} = 20\%$, $T_{f,c} = 35\%$ and $T_{f,si} = 37.5\%$ in their analysis of the study area, this seems an overestimate of the clay content as this would imply the occurrence of clay loam in the area, contrary to the observations discussed by Rayner and Nicoll (2012) and Bown et al. (1982). However, the proposed value of organic matter, 7.5%, is considered representative and in line with Rayner and Nicoll (2012), which identified limited heath vegetation and subsequent podzolization along the hill slope.

Due to Pleistocene glacial activity (Bickerdike et al., 2018; Bromley et al., 2018), a strong variation in the soil textures was expected and was tried to generate by means of the described methods. Although the glacial impact on the soil texture is represented properly in the numerical distribution, the spatial distribution is prone to some simplification due to its random distribution, which neglects possibly vital spatial features. This includes the presence of lenses of aberrant materials, which can have a significant influence on subsurface flow and thus mass movement hazard (Kessler, 2012; Shao, 2017). The textural characteristics of these lenses logically determine either enhanced or stagnating flow occurs with respect its surrounding. These lenses develop as deglaciated areas received poorly sorted sediments and aberrant materials get deposed through glacial meltwater and debris flows, as discussed by Easterbrook (1982); Bertran and Texier (1999); Eyles (2006); Evans et al. (2006); Hart and Boulton (1991) and Boulton (1996). An overview of which, from Kessler

et al. (2012), is shown in figure 38. In conclusion, the localization and characterization of lenses might be valuable in the identification of potential mass movement source areas.

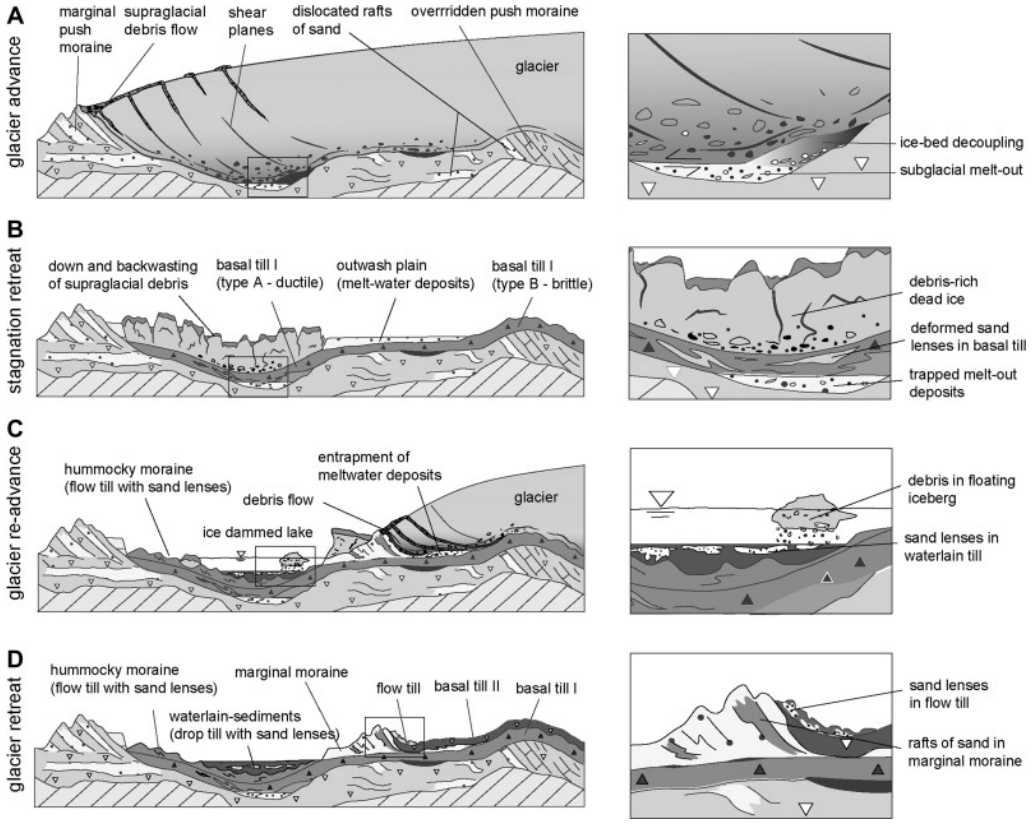

Figure 38: Overview of the influence of glacier dynamics on possible deposition of specific sediments that create lenses of deviating textures. From Kessler et al. (2012).

5.4.3 Soil Properties

The increase in bulk density over depth in the realization is attributed to the absence of organic matter at lower depths (Adams, 1973). Similar trends could be caused by the gravitational compaction of the soil under its own weight or glacial pressure (Hedberg, 1936). However, the effects of compaction are not expected to have a major impact as the study area consists mainly of strongly reworked shallow soils, implicating relatively low gravitational effects and deteriorating of paraglacial effects because of extensive weathering. Furthermore, the relatively high densities

in the subsoil can be ought representative as the aforementioned limited amount of organic matter and strong weathering of the bedrock.

As CLiDE does not allow for distributed values in the xyz-directions with respect to soil properties, the assigned weighted averages reduce the effects caused by distinct soil layers. This influences drainage rates. Especially at locations having shallow soils, which would normally have a high hydraulic conductivity, the hydraulic conductivity is strongly reduced to the average for the whole study site. Comparing the weighed average of the soil, being 0.258 m day^{-1}, to values observed in cells with shallow soils with relatively high organic matter content and high sand content of 2 m day^{-1} reflects this discrepancy. Nonetheless, Bear (2013) suggests that the realized average values are in fair agreement with generally applied values. The volumetric moisture content is affected in a similar fashion, resulting from the decreasing organic matter content and its effects on pore space and water accommodation (Gupta and Larson, 1979; Boyle et al., 1989). Hence similar issues occur with respect to the multi-dimensional distribution.

When evaluating the cohesion used in the infinite slope model, the calculated values were extremely low, ranging from 0.80 kPa to 3.25 kPa. These values normally should vary between 5 kPa and 25 kPa Lambe and Whitman (2008). However, as the cohesion was solely a function of the clay content, the abundant low clay contents initiate low cohesion values. Consequently, the slope stability of the study area was heavily underestimated. Accordingly, 4 kPa was added to make the cohesion values meet the aforementioned range. Although the additional cohesion did reduce the extent of unstable areas, the cohesion values might still be underestimated as high over-consolidation ratios can be expected, following glacial retreat (Skempton, 1984). Additionally, the over-consolidation of sediments can cause significant changes in hydrogeological properties as well (Boulton, 1996), which suggests that the values calculated from the applied pedo-transfer functions should be adjusted accordingly, as they are merely based on the soils texture.

5.4.4 SCIDDICA

The calibration of the parameters of the SCIDDICA-module proved to be rather complicated. To establish a representative parameterization, various simulation attempts with increasing P_{rl}, P_{mt} and P_{er} by one or two the order magnitude were performed, in attempt to accurately simulate the 2015 mass movement event. However, overestimation of mass deposited kept occurring. Hence, the parameterization which yielded the best resembling amount of displaced mass was applied further. Furthermore, the value for P_{er} is substantially higher when compared to D'Ambrosio

et al. (2003). When examining the results for lower APIs, this does not seem to produce large discrepancies. However, during events with more potential source areas, the amount of mobilization causes extreme amounts of material to be deposited in the valley bottom. This suggests that additional information is necessary for calibration of the parameters as well as the degree and extent to which physical characteristics of the study area are influencing these conceptual parameters. These include for instance additional information on adhesive properties, soil entrainment and frictional processes at the base of mobilized material. Only some information was available regarding the source areas of the recorded events. Additionally, detailed calibration, using an event with proper records of source areas and initial soil thickness, would extensively improve the parameterization of the SCIDDICA-module.

Aside from the difficulties in runout parameterization, it can be argued that the infinite slope model is prone to other misconceptions about the study area. As previously stated, the cohesion values based on the clay fraction did not yield representative results. However, another possible cause of the overestimation of source areas is the disparity of the internal friction angles and bulk densities. Within CLiDE the internal friction angle and bulk density are lumped variables, applied to the whole study area, whereas in the calculations for the factor of safety and thus the identification of source areas, a distributed grid is used. Consequently, this might cause cells to remain inactive although they should have been mobilized and vice versa.

6 Conclusion

Hydrological conditions are the main driver for mass movement in many environments. Consequently, the alterations of the hydrological cycle through climate change will have strong consequences on the frequency, severity and nature of mass movement. Naturally, this has implications for adaptation and mitigation measures to cope with future trends and the corresponding costs. To understand current and future hazard, it is necessary to understand, quantify and evaluate the hydrological components essential in mass movement hazard. Hence, this study addresses the main spatial and temporal implications for mass movement through climate change at the Rest and be Thankful pass.

The aim to define a hydrological threshold that is able to facilitate mass movement hazard at the pass, resulted in a threshold formula, yielding the required daily precipitation based on an API. Based on historical data for known mass movement events over the period of 2007-2017, it became apparent that a daily precipitation above 61.2 mm is likely capable of mobilizing material. Additionally, for every millimeter calculated in the API, based on 8 antecedent days, this threshold value reduces with 0.1527 mm. Although the API calculated from the historical data and the associated displaced mass estimates showed stronger correlation when 12 days were accounted for in the API, the findings of Ballantyne (2004) and Pennington et al. (2014) suggested that accounting for 8 days in the API was more suitable. Nonetheless, this emphasizes the important role of antecedent precipitation in mass movement hazard. Furthermore, the correlation between antecedent precipitation and mobilized mass implies that increasing antecedent precipitation positively influences the mass displaced following mass movement. In conclusion, the construction of this threshold serves as a low demand tool to identify potentially hazardous precipitation regimes and to some extent the expected severity.

The application of the threshold to hydrological forecasts, based UKCP scenarios, shows that only 3 of the 11 forecasts result in lower recurrence times. Generally, this implies that in terms of frequency, mass movement hazard is expected to decrease under climate change as predicted by the UKCP. However, this is mainly due to aggravating differences between seasons. Moreover, various studies emphasize the concentration of precipitation in less events as a result of climate change. Hence, recurrence times might imply ceasing mass movement facilitating hydrological conditions, their severity might increase.

The evaluation of the one-way ANOVA on the daily precipitation and antecedent precipitation associated with mass movement events, combined with the independent recurrence times of these two hyrdrological drivers, allowed to roughly identify which

one could be considered dominant in triggering mass movement at the Rest and be Thankful pass. It appears that hydrological forecasts h, i and j are largely driven by antecedent precipitation. As they show low recurrence times and high mean ranks values for their APIs with respect to the other scenarios and the historical data. Contrarily, in hydrological forecasts m, o and q mass movement is largely driven by daily precipitation. They show, relative to the other forecasts and the historical data, high recurrence times and a high mean ranks value for daily precipitation. The remaining forecasts, a, c, k, and l, show could not be classified accordingly. Evidently, these results show that the implications of climate change for mass movement hazard are rather complex and can vary strongly among different realizations of climate change. However, the differentiation of the forecasts yields a guideline for selecting forecasts, used for further evaluation and analysis of mass movement hazard at the Rest and be Thankful pass.

The predominant source areas for mass movement were found between 300 and 500 metres altitude, based on the simulation of 10 mass movement events from the hydrological forecasts, which were selected by means of the previously defined threshold. The locations of the dominant source areas are a consequence of confinement of flow in gullies and subsurface drainage channels. Additionally, small concavity-convexity transitions in the bedrock shape, reducing slope angles around 400 metres can be seen as an extra contributor by causing slower drainage of the soil. The identification of potential source areas under various scenarios can contribute significantly to more efficient implementation of mitigation and adaptation strategies and could guide further research in effective analysis of the pass.

Different precipitation regimes have shown to activate different flow paths and source areas. The simulations of the mass movement events from the hydrological forecasts showed that peak precipitation in the first half of the the eight preceding days resulted mainly in the mobilization of material in the zone between 300 and 500 metres altitude. However, antecedent precipitation regimes with peak precipitation in the latter stages of the eight preceding days and APIs above 200 mm, seemed to result in the mobilization of additional material from higher altitudes, up to 800 metres, due the exceedance of the drainage capacity of the soil and subsequent accumulation of water.

From a temporal perspective it is possible to conclude that mass movement frequency will cease under most UKCP based hydrological forecasts. Nonetheless, conclusions regarding the severity of mass movement require some prudence as rainfall intensity is neglected but it can be argued that wetter forecasts will experience more severe mass movement, based on the correlation between mobilized mass and antecedent precipitation. Additionally, the aggravation between seasons and the

concentration of precipitation in less events might increase mass movement severity whilst reducing its frequency. From a spatial perspective, it is concluded that the main source areas are situated between 300 and 500 metres altitude and that late peaks in antecedent precipitation regimes enhance mobilization of material at higher altitudes, up to 800 metres. This leads to conclude that under wetter climate change scenarios, the dominant source areas might propagate upslope.

References

Adams, W. A. (1973). The effect of organic matter on the bulk and true densities of some uncultivated podzolic soils. *Journal of Soil Science*, 24(1):10–17.

Allen, R. G., Pereira, L. S., Raes, D., Smith, M., et al. (1998). Crop evapotranspiration-guidelines for computing crop water requirements-fao irrigation and drainage paper 56. *Fao, Rome*, 300(9):D05109.

Bainbridge, R., Dunning, S., and Lim, M. (2018). Low-cost optical and seismic monitoring of debris-flow hazards on the Rest and Be Thankful, Scotland. In *EGU General Assembly Conference Abstracts*, volume 20 of *EGU General Assembly Conference Abstracts*, page 15784.

Balland, V., Pollacco, J. A. P., and Arp, P. A. (2008). Modeling soil hydraulic properties for a wide range of soil conditions. *Ecological Modelling*, 219(3):300–316.

Ballantyne, C. K. (2002). Paraglacial geomorphology. *Quaternary Science Reviews*, 21(18):1935 – 2017.

Ballantyne, C. K. (2004). *Geomorphological changes and trends in Scotland: debris-flows*. Scottish Natural Heritage.

Ballantyne, C. K. (2008). After the ice: Holocene geomorphic activity in the scottish highlands. *Scottish Geographical Journal*, 124(1):8–52.

Ballantyne, C. K. (2018). After the ice: Lateglacial and Holocene landforms and landscape evolution in Scotland. *Earth and Environmental Science Transactions of the Royal Society of Edinburgh*, page 1–39.

Balzano, B., Tarantino, A., and Ridley, A. (2016). Analysis of a rainfall-triggered landslide at Rest and be Thankful in Scotland. *E3S Web Conf.*, 9:15009.

Barkwith, K. A. P., Hurst, M. D., Jackson, C. R., Wang, L., Ellis, M. A., and Coulthard, T. J. (2015). Simulating the influences of groundwater on regional geomorphology using a distributed, dynamic, landscape evolution modelling platform. *Environmental Modelling and Software*, 74:1 – 20.

Bates, P. D., Horritt, M. S., and Fewtrell, T. J. (2010). A simple inertial formulation of the shallow water equations for efficient two-dimensional flood inundation modelling. *Journal of Hydrology*, 387(1):33 – 45.

Bear, J. (2013). *Dynamics of fluids in porous media*. Courier Corporation.

Berti, M., Martina, M. L. V., Franceschini, S., Pignone, S., Simoni, A., and Pizziolo, M. (2012). Probabilistic rainfall thresholds for landslide occurrence using a Bayesian approach. *Journal of Geophysical Research: Earth Surface*, 117(F4).

Berti, M. and Simoni, A. (2005). Experimental evidences and numerical modelling of debris flow initiated by channel runoff. *Landslides*, 2(3):171–182.

Bertran, P. and Texier, J.-P. (1999). Facies and microfacies of slope deposits. *CATENA*, 35(2):99 – 121.

BGS Landslide Team (2018a). National landslide database. https://www.bgs.ac.uk/landslides/nld.html. accessed: 05-12-2018.

BGS Landslide Team (2018b). Rest and be thankful slope showing landslides from 2007, 2009, 2011 and 2012. https://www.bgs.ac.uk/landslides/RABTAug2012.html. accessed: 05-12-2018.

Bickerdike, H. L., Ó Cofaigh, C., Evans, D. J. A., and Stokes, C. R. (2018). Glacial landsystems, retreat dynamics and controls on Loch Lomond Stadial (Younger Dryas) glaciation in Britain. *Boreas*, 47(1):202–224.

Boorman, D., Hollis, J., and Lilly, A. (1995). *Hydrology of soil types: a hydrologically-based classification of the soils of United Kingdom.* Institute of Hydrology.

Boulton, G. S. (1996). Theory of glacial erosion, transport and deposition as a consequence of subglacial sediment deformation. *Journal of Glaciology*, 42(140):43–62.

Bown, C. J., Shipley, B. M., and Bibby, J. S. (1982). South-West Scotland: Soil and land capability for agriculture. *Soil Survey of Scotland*, 6:14–122.

Boyle, M., Frankenberger, W. T., and Stolzy, L. H. (1989). The influence of organic matter on soil aggregation and water infiltration. *Journal of Production Agriculture*, 2(4):290–299.

Brayshaw, D. and Hassan, M. A. (2009). Debris flow initiation and sediment recharge in gullies. *Geomorphology*, 109(3):122 – 131.

Bromley, G., Putnam, A., Borns, H., Lowell, T., Sandford, T., and Barrell, D. (2018). Interstadial rise and Younger Dryas demise of Scotland's last ice fields. *Paleoceanography and Paleoclimatology*, 33(4):412–429.

Brown, I., Poggio, L., Gimona, A., and Castellazzi, M. (2011). Climate change, drought risk and land capability for agriculture: implications for land use in scotland. *Regional Environmental Change*, 11(3):503–518.

Bruce, J. P. and Clark, R. H. (1966). *Introduction to Hydrometeorology: Pergamon International Library of Science, Technology, Engineering and Social Studies*. Elsevier Science.

Chan, S. C., Kahana, R., Kendon, E. J., and Fowler, H. J. (2018). Projected changes in extreme precipitation over Scotland and Northern England using a high-resolution regional climate model. *Climate Dynamics*.

Chen, C.-W., Oguchi, T., Chen, H., and Lin, G.-W. (2018). Estimation of the antecedent rainfall period for mass movements in taiwan. *Environmental Earth Sciences*, 77(5):184.

Chertkov, V. Y. (2002). Modelling cracking stages of saturated soils as they dry and shrink. *European Journal of Soil Science*, 53(1):105–118.

Christierson, B. V., Vidal, J., and Wade, S. D. (2012). Using UKCP09 probabilistic climate information for UK water resource planning. *Journal of Hydrology*, 424-425:48 – 67.

Claessens, L., Schoorl, J. M., and Veldkamp, A. (2007). Modelling the location of shallow landslides and their effects on landscape dynamics in large watersheds: An application for Northern New Zealand. *Geomorphology*, 87(1):16 – 27. Human Impact and Geomorphology in Tropical Mountain Areas.

Coe, J. A., Kinner, D. A., and Godt, J. W. (2008). Initiation conditions for debris flows generated by runoff at Chalk Cliffs, central Colorado. *Geomorphology*, 96(3):270 – 297. Debris flows initiated by runoff, erosion, and sediment entrainment in western North America.

Cosma, S., Richard, E., and Miniscloux, F. (2006). The role of small-scale orographic features in the spatial distribution of precipitation. *Quarterly Journal of the Royal Meteorological Society*, 128(579):75–92.

Coulthard, T. J., Neal, J. C., Bates, P. D., Ramirez, J., Almeida, G. A. M., and Hancock, G. R. (2013). Integrating the LISFLOOD-FP 2D hydrodynamic model with the CAESAR model: implications for modelling landscape evolution. *Earth Surface Processes and Landforms*, 38(15):1897–1906.

Coulthard, T. J. and Van de Wiel, M. J. (2006). A cellular model of river meandering. *Earth Surface Processes and Landforms*, 31(1):123–132.

Crosta, G. B. and Frattini, P. (2001). Rainfall thresholds for triggering soil slips and debris flow. In *Proc. of the 2nd EGS Plinius Conference on Mediterranean Storms: Publication CNR GNDCI*, volume 2547, pages 463–487.

Crozier, M. J. (1986). *Landslides: Causes, Consequences & Environment*. Croom Helm.

Cruden, D. M. and Varnes, D. J. (1996). Landslide types and processes, special report. *Transportation Research Board, National Academy of Sciences*, 247:36–75.

Dahal, R. K. and Hasegawa, S. (2008). Representative rainfall thresholds for landslides in the Nepal Himalaya. *Geomorphology*, 100(3):429 – 443.

D'Ambrosio, D., Di Gregorio, S., and Iovine, G. (2003). Simulating debris flows through a hexagonal cellular automata model: SCIDDICA S_{3-hex}. *Natural Hazards and Earth System Sciences*, 3(6):545–559.

Daniel, W. W. (1990). *Applied Nonparametric Statistics*. Duxbury advanced series in statistics and decision sciences. PWS-KENT.

Di Gregorio, S., Kongo, R., Siciliano, C., Sorriso-Valvo, M., and Spataro, W. (1999). Mount ontake landslide simulation by the cellular automata model sciddica-3. *Physics and Chemistry of the Earth, Part A: Solid Earth and Geodesy*, 24(2):131 – 137.

Di Gregorio, S. and Serra, R. (1999). An empirical method for modelling and simulating some complex macroscopic phenomena by cellular automata. *Future Generation Computer Systems*, 16(2):259 – 271.

Dilley, M., Chen, R. S., Deichmann, U., Lerner-Lam, A. L., and Arnold, M. (2005). *Natural disaster hotspots: a global risk analysis*. The World Bank.

Dowling, C. A. and Santi, P. M. (2014). Debris flows and their toll on human life: a global analysis of debris-flow fatalities from 1950 to 2011. *Natural hazards*, 71(1):203–227.

Easterbrook, D. J. (1982). Characteristic features of glacial sediments. *American Association of Petroleum Geologists Memoir*, 31:1–10.

Edwards, K. J. and Whittington, G. (2001). Lake sediments, erosion and landscape change during the Holocene in Britain and Ireland. *CATENA*, 42(2):143 – 173.

Evans, D. J. A., Phillips, E. R., Hiemstra, J. F., and Auton, C. A. (2006). Subglacial till: Formation, sedimentary characteristics and classification. *Earth-Science Reviews*, 78(1):115 – 176.

Eyles, N. (2006). The role of meltwater in glacial processes. *Sedimentary Geology*, 190(1):257 – 268. Sedimentology and Sequence Stratigraphy of Fluvial Deposits.

Fan, L., Lehmann, P., and Or, D. (2015). Effects of hydromechanical loading history and antecedent soil mechanical damage on shallow landslide triggering. *Journal of Geophysical Research: Earth Surface*, 120(10):1990–2015.

Fan, L., Lehmann, P., and Or, D. (2016). Load redistribution rules for progressive failure in shallow landslides: Threshold mechanical models. *Geophysical Research Letters*, 44(1):228–235.

Faurès, J.-M., Goodrich, D. C., Woolhiser, D. A., and Sorooshian, S. (1995). Impact of small-scale spatial rainfall variability on runoff modeling. *Journal of Hydrology*, 173(1):309 – 326.

Freer, J., McDonnell, J. J., Beven, K., Peters, N. E., Burns, D. A., Hooper, R., Aulenbach, B., and Kendall, C. (2002). The role of bedrock topography on subsurface storm flow. *Water Resources Research*, 38(12):5–1.

Glade, T., Crozier, M. J., and Smith, P. (2000). Applying probability determination to refine landslide-triggering rainfall thresholds using an empirical "antecedent daily rainfall model". *pure and applied geophysics*, 157(6):1059–1079.

Gupta, S. C. and Larson, W. E. (1979). Estimating soil water retention characteristics from particle size distribution, organic matter percent, and bulk density. *Water Resources Research*, 15(6):1633–1635.

Hadley Centre for Climate Prediction and Research (2008). UKCP 09: Met Office Hadley Centre Regional Climate Model HadRM3-PPE Data.

Hart, J. K. and Boulton, G. S. (1991). The interrelation of glaciotectonic and glaciodepositional processes within the glacial environment. *Quaternary Science Reviews*, 10(4):335 – 350.

Heath, R. C. (1983). Basic ground-water hydrology: Us geological survey water-supply paper 2220. *US Geological Survey, Washington, DC*.

Hedberg, H. D. (1936). Gravitational compaction of clays and shales. *American Journal of Science*, 1(184):241–287.

Heimsath, A. M., Dietrich, W. E., Nishiizumi, K., and Finkel, R. C. (1997). The soil production function and landscape equilibrium. *Nature*, 388(6640):358.

Heimsath, A. M., Dietrich, W. E., Nishiizumi, K., and Finkel, R. C. (1999). Cosmogenic nuclides, topography, and the spatial variation of soil depth. *Geomorphology*, 27(1-2):151–172.

Heimsath, A. M., Dietrich, W. E., Nishiizumi, K., and Finkel, R. C. (2001). Stochastic processes of soil production and transport: Erosion rates, topographic variation and cosmogenic nuclides in the Oregon Coast Range. *Earth Surface Processes and Landforms*, 26(5):531–552.

Istanbulluoglu, E., Bras, R. L., Flores-Cervantes, H., and Tucker, G. E. (2005). Implications of bank failures and fluvial erosion for gully development: Field observations and modeling. *Journal of Geophysical Research: Earth Surface*, 110(F1).

Iverson, R. M. (1997). The physics of debris flows. *Reviews of geophysics*, 35(3):245–296.

Iverson, R. M. (2000). Landslide triggering by rain infiltration. *Water Resour. Res.*, 36:1897–1910.

Iverson, R. M., Reid, M. E., Logan, M., LaHusen, R. G., Godt, J. W., and Griswold, J. P. (2011). Positive feedback and momentum growth during debris-flow entrainment of wet bed sediment. *Nature Geoscience*, 4(2):116.

James, H. (2017). Private Communication.

Kay, A. L. and Jones, R. G. (2012). Comparison of the use of alternative UKCP09 products for modelling the impacts of climate change on flood frequency. *Climatic Change*, 114(2):211–230.

Kean, J. W., McCoy, S. W., Tucker, G. E., Staley, D. M., and Coe, J. A. (2013). Runoff-generated debris flows: Observations and modeling of surge initiation, magnitude, and frequency. *Journal of Geophysical Research: Earth Surface*, 118(4):2190–2207.

Kessler, T. C. (2012). *Hydrogeological Characterization of Low-permeability Clayey Tills–the Role of Sand Lenses*. PhD thesis, Technical University of Denmark.

Kessler, T. C., Klint, K. E. S., Nilsson, B., and Bjerg, P. L. (2012). Characterization of sand lenses embedded in tills. *Quaternary Science Reviews*, 53:55 – 71.

Kirkby, M. J. (1967). Measurement and theory of soil creep. *The Journal of Geology*, 75(4):359–378.

Kjekstad, O. and Highland, L. (2009). Economic and social impacts of landslides. In *Landslides–disaster risk reduction*, pages 573–587. Springer.

Klaassen, B. and Pilgrim, D. H. (1975). Hydrograph recession constants for New South Wales streams. *Civil Engineering Transactions*, pages 43–49.

Korup, O., Densmore, A. L., and Schlunegger, F. (2010). The role of landslides in mountain range evolution. *Geomorphology*, 120(1):77 – 90. Landslide geomorphology in a changing environment.

Lambe, T. W. and Whitman, R. V. (2008). *Soil mechanics SI version*. John Wiley & Sons.

Lehmann, P. and Or, D. (2012). Hydromechanical triggering of landslides: From progressive local failures to mass release. *Water Resources Research*, 48(3).

Lowe, J. J. and Walker, M. J. C. (1997). *Reconstructing Quaternary Environments*. Longman.

Macklin, C. (2013). A83 trunk road route study. *Jacobs U.K. Ltd.*

Martin, Y. (2000). Modelling hillslope evolution: linear and nonlinear transport relations. *Geomorphology*, 34(1-2):1–21.

Marui, H. and International Research Society Interpraevent (2006). *Disaster mitigation of debris flows, slope failures and landslides : proceedings of the INTERPRAEVENT International Symposium Disaster Mitigation of Debris Flows, Slope Failures and Landslides held on September 25 - 27, 2006, in Niigata, Japan. 2*. Number v. 2 in Frontiers science series. Universal Acad. Press.

Mather, A. S. (2004). Forest transition theory and the reforesting of Scotland. *Scottish Geographical Journal*, 120(1-2):83–98.

McQuaker, G., Graeme Herd, J., and Johnston, K. (2014). Can we rest and be thankful yet? solutions and effective stakeholder engagement for the a83 trunk road route study. Technical report, Scotland Transport.

MetOffice (2018). Annual Average Precipitation Map. https://floodforecastingservice.net/2015/05/11/the-climatology-of-scotland-four-seasons-in-one-day/. accessed: 27-08-2018.

Morgan, R., Quinton, J., Smith, R., Govers, G., Poesen, J., Auerswald, K., Chisci, G., Torri, D., and Styczen, M. (1998). The european soil erosion model (eurosem): a dynamic approach for predicting sediment transport from fields and small catchments. *Earth Surface Processes and Landforms: The Journal of the British Geomorphological Group*, 23(6):527–544.

Morris, D. A. and Johnson, A. I. (1967). Summary of hydrologic and physical properties of rock and soil materials, as analyzed by the hydrologic laboratory of the us geological survey, 1948-60. Technical report, US Govt. Print. Off.,.

Morris, P. H., Graham, J., and Williams, D. J. (1992). Cracking in drying soils. *Canadian Geotechnical Journal*, 29(2):263–277.

Mulligan, M. and Wainwright, J. (2004). Modelling and model building. *Environmental modelling: Finding simplicity in complexity*, pages 7–73.

Murphy, J. M., Booth, B. B. B., Collins, M., Harris, G. R., Sexton, D. M. H., and Webb, M. J. (2007). A methodology for probabilistic predictions of regional climate change from perturbed physics ensembles. *Philosophical Transactions of the Royal Society of London A: Mathematical, Physical and Engineering Sciences*, 365(1857):1993–2028.

Murphy, J. M., Sexton, D. M., Jenkins, G. J., Booth, B. B. B., Brown, C. C., Clark, R. T., Collins, M., Harris, G. R., Kendon, E. J., Betts, R. A., Brown, S. J., Humphrey, K. A., McCarthy, M. P., McDonald, R. E., Stephens, A., Wallace, C., Warren, R., Wilby, R., and Wood, R. A. (2009). UK Climate Projections Science Report: Climate Change projections. Working paper, Exeter.

Ng, C. W., Wang, B., and Tung, Y.-K. (2001). Three-dimensional numerical investigations of groundwater responses in an unsaturated slope subjected to various rainfall patterns. *Canadian Geotechnical Journal*, 38(5):1049–1062.

Pelletier, J. D. and Rasmussen, C. (2009a). Geomorphically based predictive mapping of soil thickness in upland watersheds. *Water Resources Research*, 45(9).

Pelletier, J. D. and Rasmussen, C. (2009b). Quantifying the climatic and tectonic controls on hillslope steepness and erosion rate. *Lithosphere*, 1(2):73–80.

Pennington, C., Dijkstra, T. A., Lark, M., Dashwood, C., Harrison, A., and Freeborough, K. (2014). Antecedent precipitation as a potential proxy for landslide incidence in South West United Kingdom. In Sassa, K., Canuti, P., and Yin, Y., editors, *Landslide Science for a Safer Geoenvironment*, pages 253–259, Cham. Springer International Publishing.

Petley, D. (2012). Global patterns of loss of life from landslides. *Geology*, 40(10):927.

Pierson, T. C. and Costa, J. E. (1987). A rheologic classification of subaerial sediment-water flows. *Debris flows/avalanches: process, recognition, and mitigation. Reviews in Engineering Geology*, 7:1–12.

Prellwitz, R. W. (1981). *Transportation engineering handbook, Region 1.* Number 11 in Transportation engineering handbook. U.S. Department of Agriculture, Forest Service, Northern Region.

Prellwitz, R. W., Koler, T. E., Steward, J. E., Hall, D. E., Long, M. T., Remboldt, M. D., and United States. Forest Service. Engineering Staff (1994). *Slope Stability Reference Guide for National Forests in the United States.* Number v. 2 in Slope Stability Reference Guide for National Forests in the United States. U.S. Department of Agriculture, Forest Service, Engineering Staff.

Rayner, B. and Nicoll, B. (2012). Potential for woodland restoration above the a83 in glen croe to reduce the incidence of water erosion and debris flows. *Forest Research*, pages 1–24.

Roering, J. J. (2008). How well can hillslope evolution models "explain" topography? simulating soil transport and production with high-resolution topographic data. *GSA Bulletin*, 120(9-10):1248.

Sanderson, M. G. (2010). Changes in the frequency of extreme rainfall events for selected towns and cities. *Ofwat, UK*.

Sanderson, M. G., Wiltshire, A. J., and Betts, R. A. (2012). Projected changes in water availability in the United Kingdom. *Water Resources Research*, 48(8).

Sassa, K., Guzzetti, F., Yamagishi, H., Arbanas, Ž., Casagli, N., Tiwari, B., Liu, K.-F., Strom, A., McSaveney, M., McSaveney, E., Dang, K., and Setiawan, H. (2017).

Landslide dynamics: Isdr-icl landslide interactive teaching tools (litt). In Sassa, K., Mikoš, M., and Yin, Y., editors, *Advancing Culture of Living with Landslides*, pages 193–218, Cham. Springer International Publishing.

Schuster, R. L. (1996). *Landslides: Investigation and Mitigation. Chapter 2 Socioeconomic Significance of Landslides*. Number 247 in 1. National Research Council.

Selby, M. J. (1982). *Hillslope materials and processes*. Oxford University Press.

Shao, W. (2017). *Numerical modeling of the effect of preferential flow on hillslope hydrology and slope stability*. PhD thesis, Delft University of Technology.

Shroder, J. F., Owen, L. A., Seong, Y. B., Bishop, M. P., Bush, A., Caffee, M. W., Copland, L., Finkel, R. C., and Kamp, U. (2011). The role of mass movements on landscape evolution in the Central Karakoram: Discussion and speculation. *Quaternary International*, 236(1):34 – 47. Quaternary Paleoenvironmental Change and Landscape Development in Tibet and the Bordering Mountains.

Skempton, A. W. (1984). *Horizontal Stresses in an Over-Consolidated Eocene Clay*, pages 119–125. Thomas Telford Publishing.

Smakhtin, Y. V. and Masse, B. (2000). Continuous daily hydrograph simulation using duration curves of a precipitation index. *Hydrological Processes*, 14(6):1083–1100.

Sparkes, B., Dunning, S., Lim, M., and Winter, M. G. (2017). Characterisation of recent debris flow activity at the Rest and Be Thankful, Scotland. In *Advancing Culture of Living with Landslides*, pages 51–58, Cham. Springer International Publishing.

Stephenson, D. and Gould, D. E. (1995). *The Grampian Highlands*, volume 4. Bernan Assoc.

Sun, W.-J. and Cui, Y.-J. (2018). Investigating the microstructure changes for silty soil during drying. *Géotechnique*, 68(4):370–373.

Tanner, P. G., Thomas, C. W., Harris, A. L., Gould, D., Harte, B., Treagus, J. E., and Stephenson, D. (2013). The Dalradian rocks of the Highland Border region of Scotland. *Proceedings of the Geologists' Association*, 124(1):215 – 262. The Dalradian Rocks of Scotland.

Thompson, J. R. (2012). Modelling the impacts of climate change on upland catchments in southwest scotland using mike she and the ukcp09 probabilistic projections. *Hydrology Research*, 43(4):507.

Tsai, T.-L. (2008). The influence of rainstorm pattern on shallow landslide. *Environmental Geology*, 53(7):1563–1569.

United States Geological Survey (2004). Landslide types and processes. https://pubs.usgs.gov/fs/2004/3072/fs-2004-3072.html. accessed: 05-12-2018.

Van Asch, T. W. J., Buma, J., and Van Beek, L. P. H. (1999). A view on some hydrological triggering systems in landslides. *Geomorphology*, 30(1-2):25–32.

Van Asch, T. W. J., Van Beek, L. P. H., and Bogaard, T. A. (2009). The diversity in hydrological triggering systems of landslides. In *Proceedings of The First Italian Workshop on Landslides*, pages 8–10.

Varnes, D. J. (1978). Slope movement types and processes. *Special report*, 176:11–33.

Weisstein, E. W. (2018). Convex hull. http://mathworld.wolfram.com/ConvexHull.html. accessed: 05-12-2018.

Whipple, K. X. and Dunne, T. (1992). The influence of debris-flow rheology on fan morphology, Owens Valley, California. *GSA Bulletin*, 104(7):887.

Appendices

A Simulation Time Series

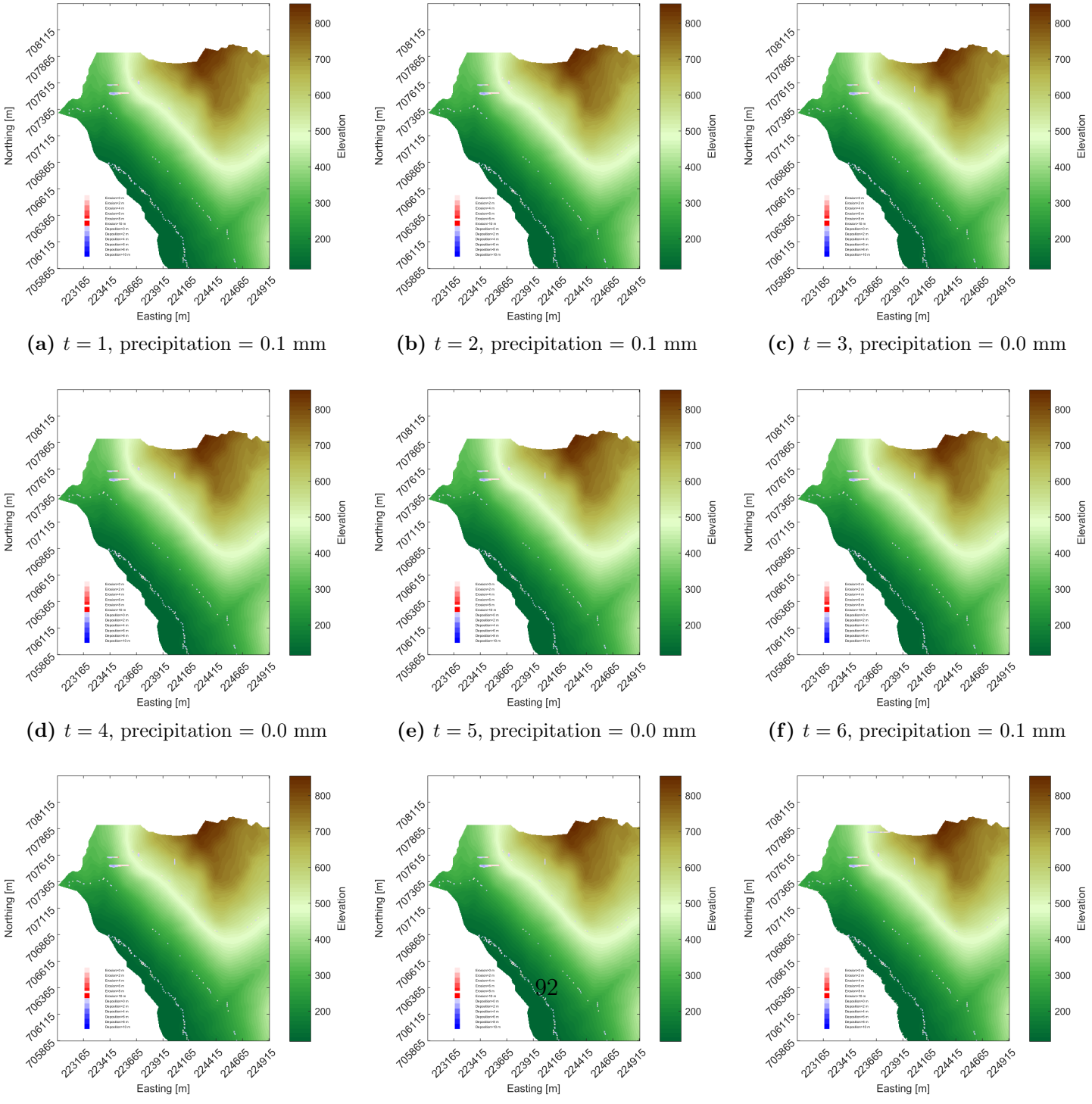

(a) $t = 1$, precipitation = 0.1 mm **(b)** $t = 2$, precipitation = 0.1 mm **(c)** $t = 3$, precipitation = 0.0 mm

(d) $t = 4$, precipitation = 0.0 mm **(e)** $t = 5$, precipitation = 0.0 mm **(f)** $t = 6$, precipitation = 0.1 mm

(g) $t = 7$, precipitation = 0.0 mm **(h)** $t = 8$, precipitation = 3.0 mm **(i)** $t = 9$, precipitation = 81.3 mm

Figure 39: Time series for 28-11-2019.

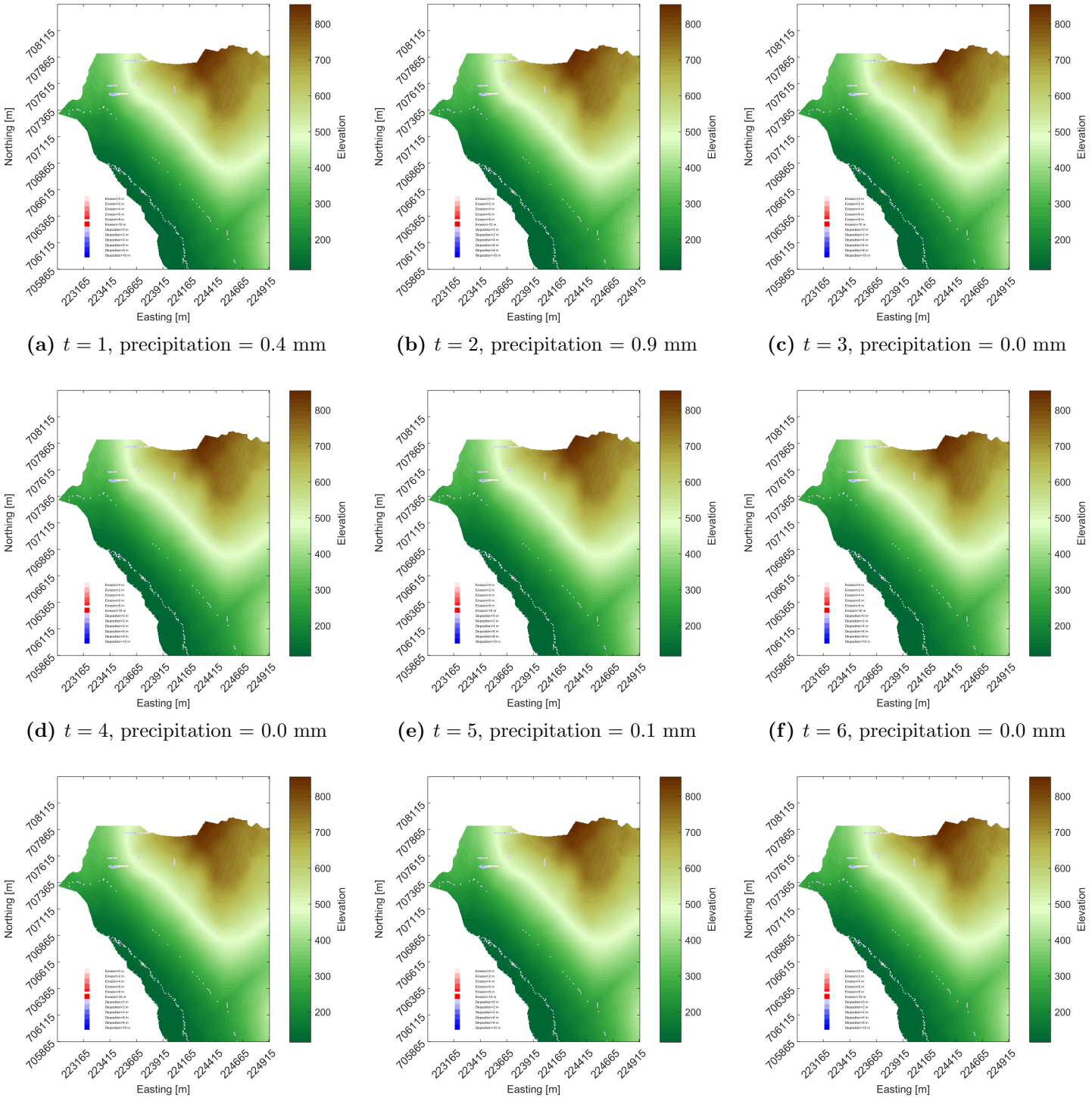

(a) $t = 1$, precipitation = 0.4 mm **(b)** $t = 2$, precipitation = 0.9 mm **(c)** $t = 3$, precipitation = 0.0 mm

(d) $t = 4$, precipitation = 0.0 mm **(e)** $t = 5$, precipitation = 0.1 mm **(f)** $t = 6$, precipitation = 0.0 mm

(g) $t = 7$, precipitation = 0.0 mm **(h)** $t = 8$, precipitation = 0.0 mm **(i)** $t = 9$, precipitation = 66.6 mm

Figure 40: Time series for 05-03-2022.

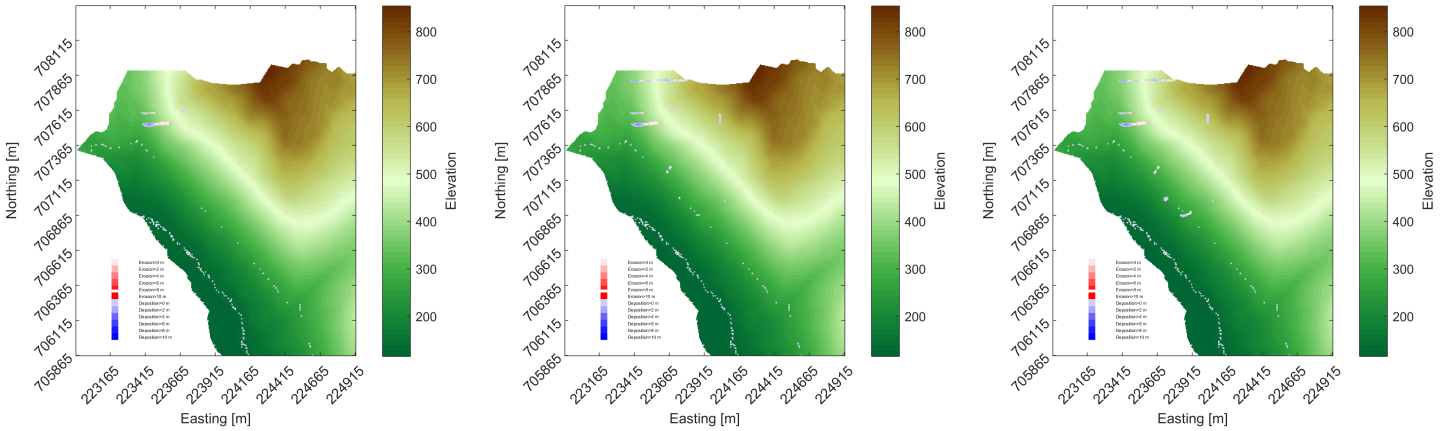

(a) $t = 1$, precipitation = 12.4 mm **(b)** $t = 2$, precipitation = 0.0 mm **(c)** $t = 3$, precipitation = 0.1 mm

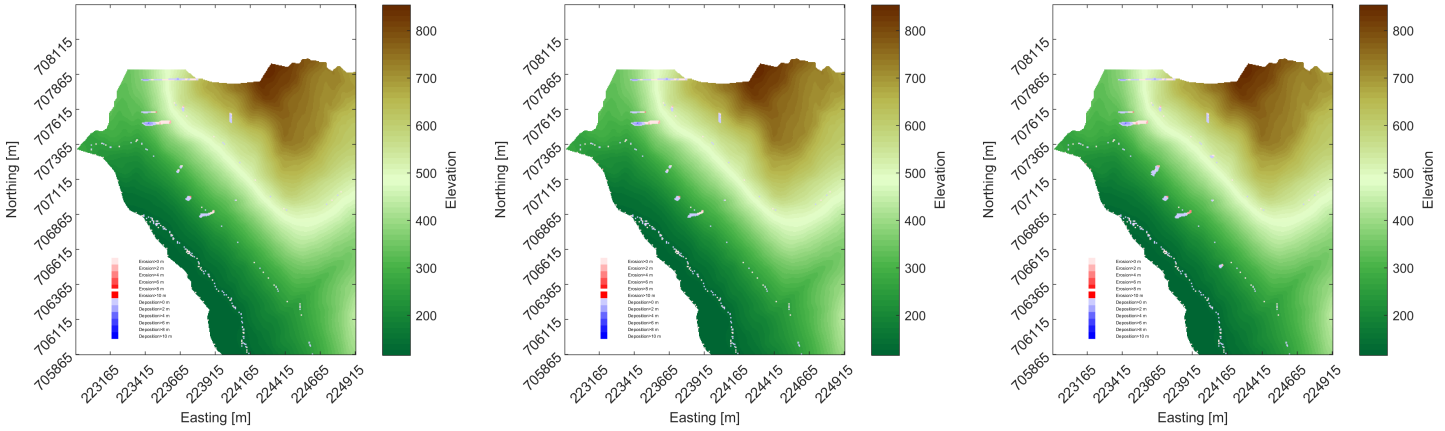

(d) $t = 4$, precipitation = 6.3 mm **(e)** $t = 5$, precipitation = 20.8 mm **(f)** $t = 6$, precipitation = 12.9 mm

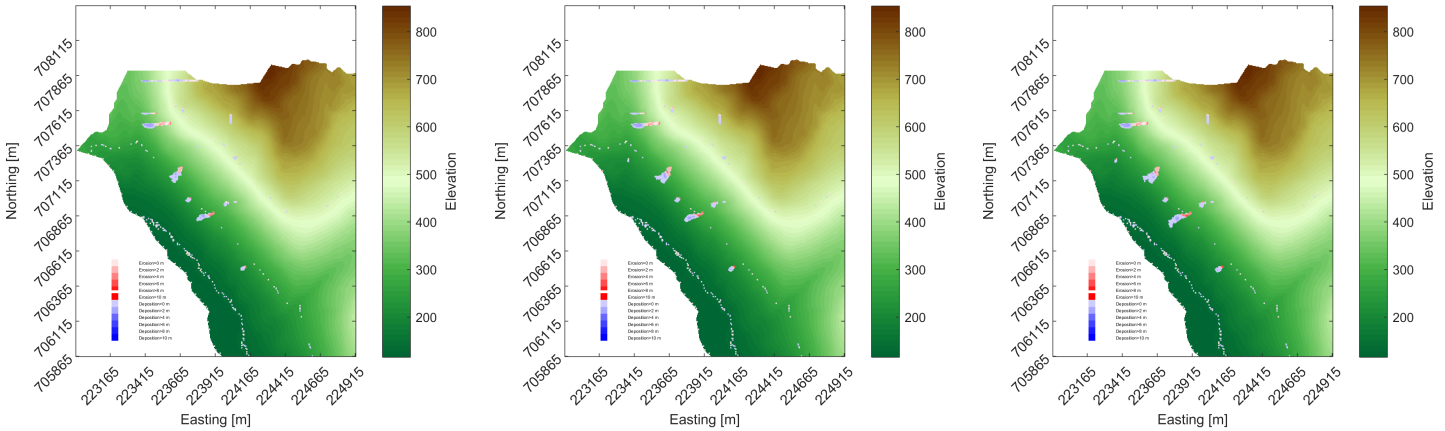

(g) $t = 7$, precipitation = 0.7 mm **(h)** $t = 8$, precipitation = 3.9 mm **(i)** $t = 9$, precipitation = 109.4 mm

Figure 41: Time series for 23-01-2024.

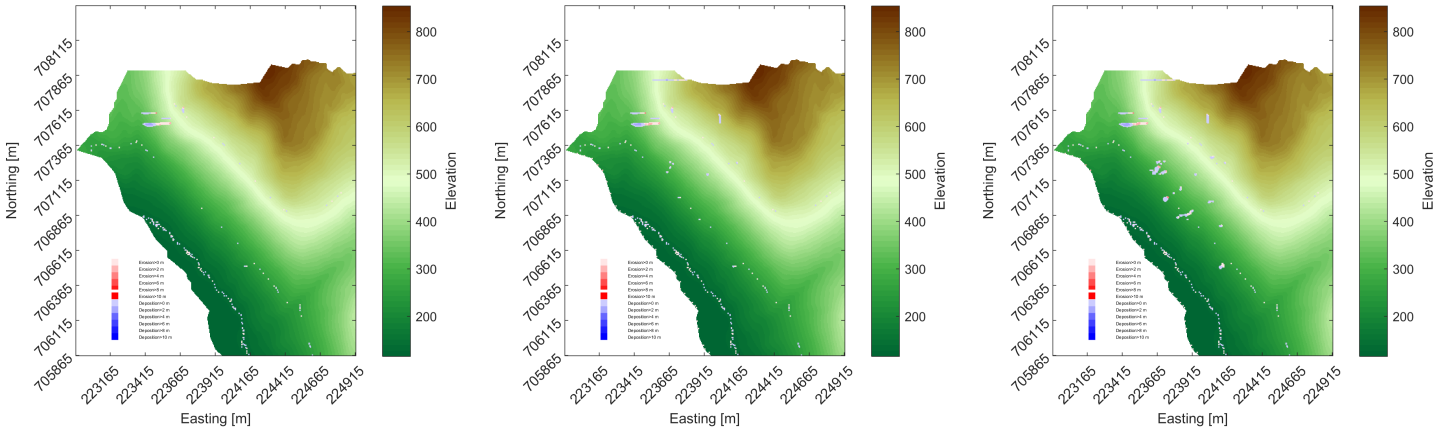

(a) $t = 1$, precipitation = 5.8 mm **(b)** $t = 2$, precipitation = 26.7 mm **(c)** $t = 3$, precipitation = 17.2 mm

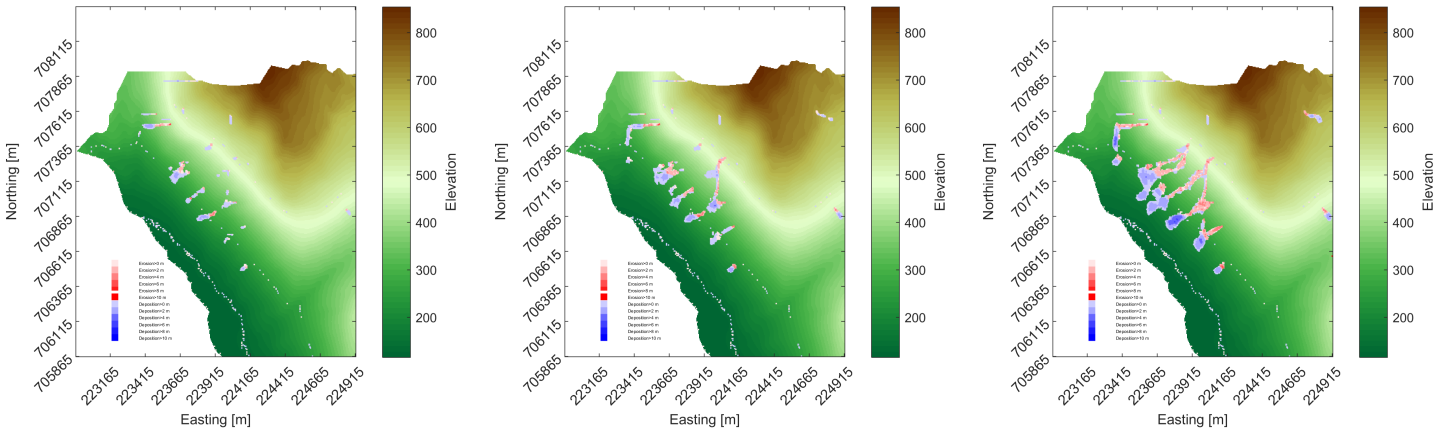

(d) $t = 4$, precipitation = 68.6 mm **(e)** $t = 5$, precipitation = 25.2 mm **(f)** $t = 6$, precipitation = 14.7 mm

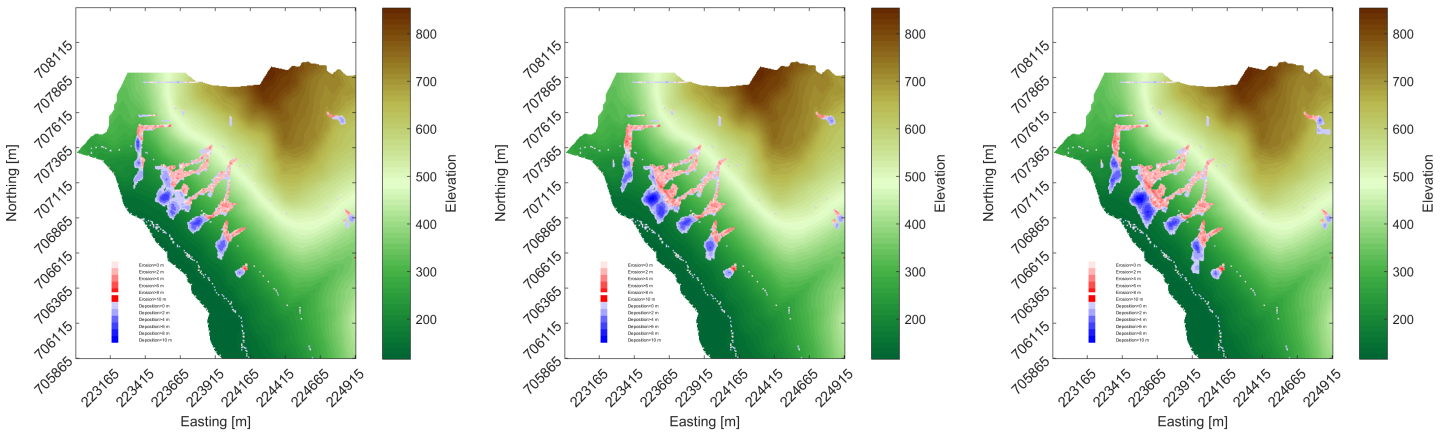

(g) $t = 7$, precipitation = 15.5 mm **(h)** $t = 8$, precipitation = 12.9 mm **(i)** $t = 9$, precipitation = 37.4 mm

Figure 42: Time series for 24-09-2028.

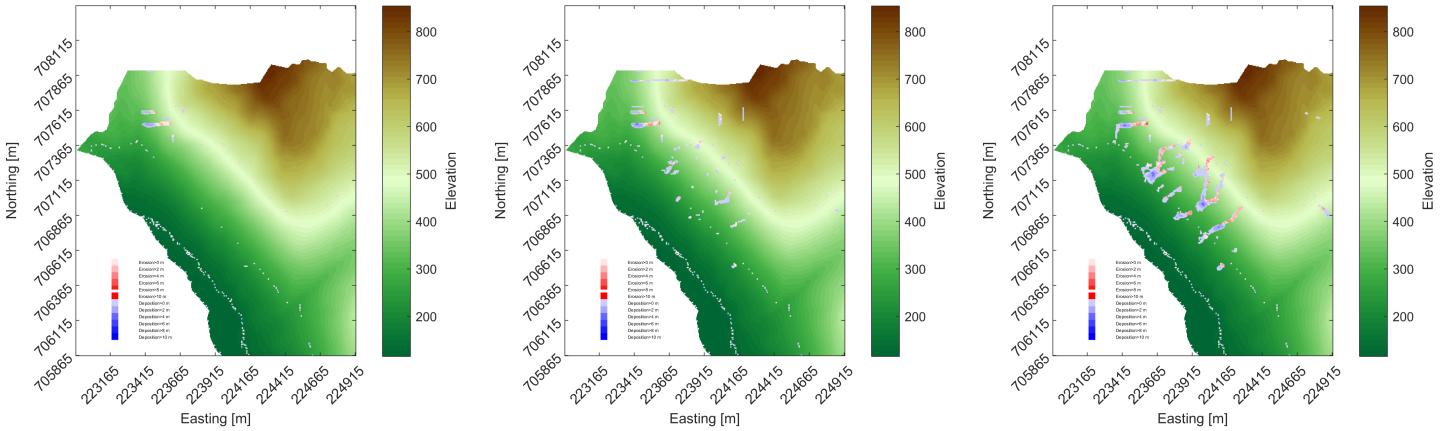

(a) $t = 1$, precipitation = 52.6 mm **(b)** $t = 2$, precipitation = 46.2 mm **(c)** $t = 3$, precipitation = 4.3 mm

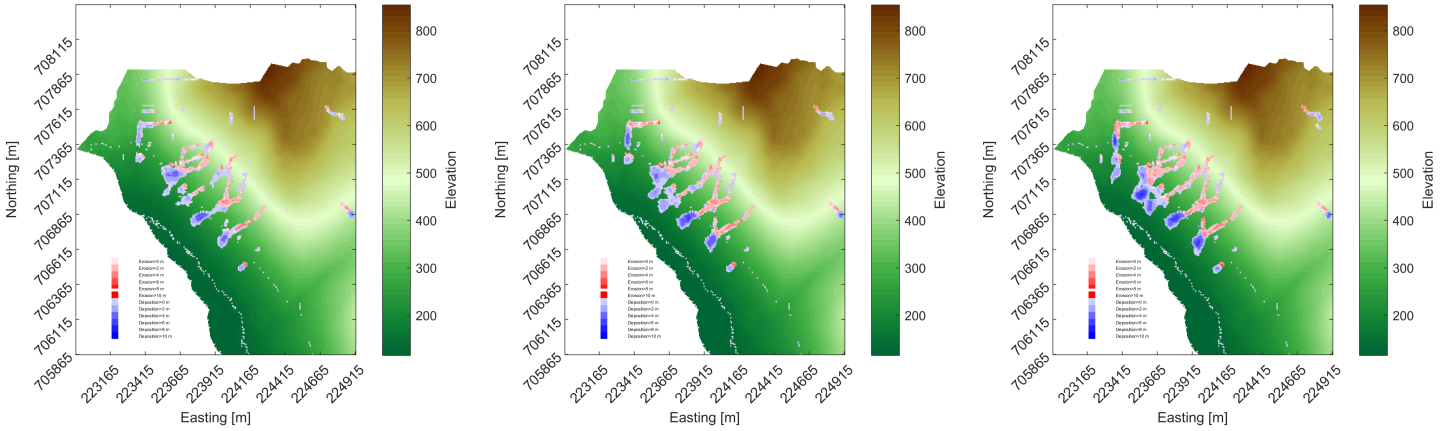

(d) $t = 4$, precipitation = 1.5 mm **(e)** $t = 5$, precipitation = 2.3 mm **(f)** $t = 6$, precipitation = 6.4 mm

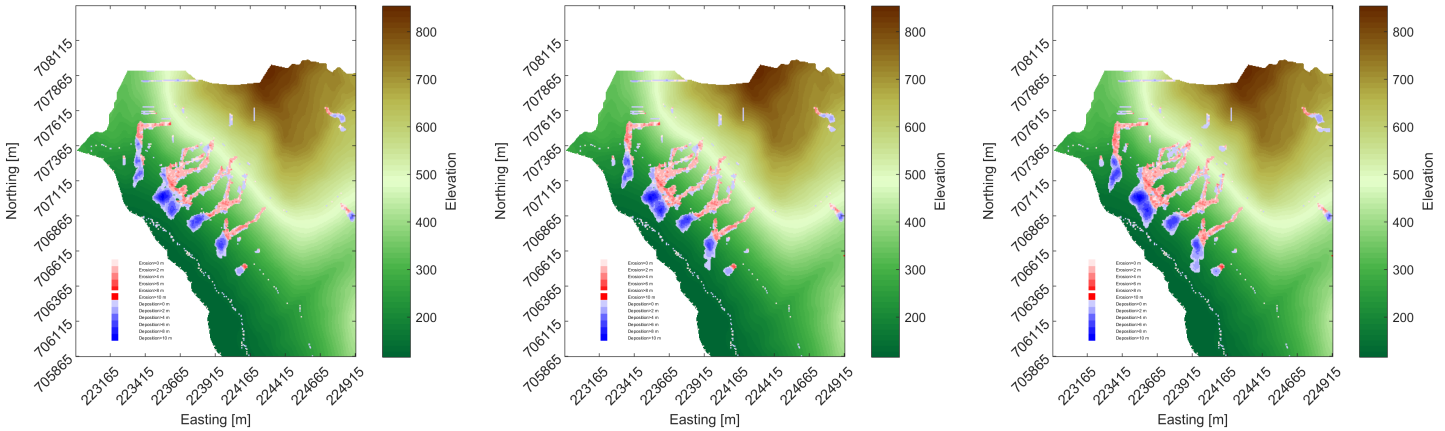

(g) $t = 7$, precipitation = 48.2 mm **(h)** $t = 8$, precipitation = 96.8 mm **(i)** $t = 9$, precipitation = 89.8 mm

Figure 43: Time series for 21-11-2032.

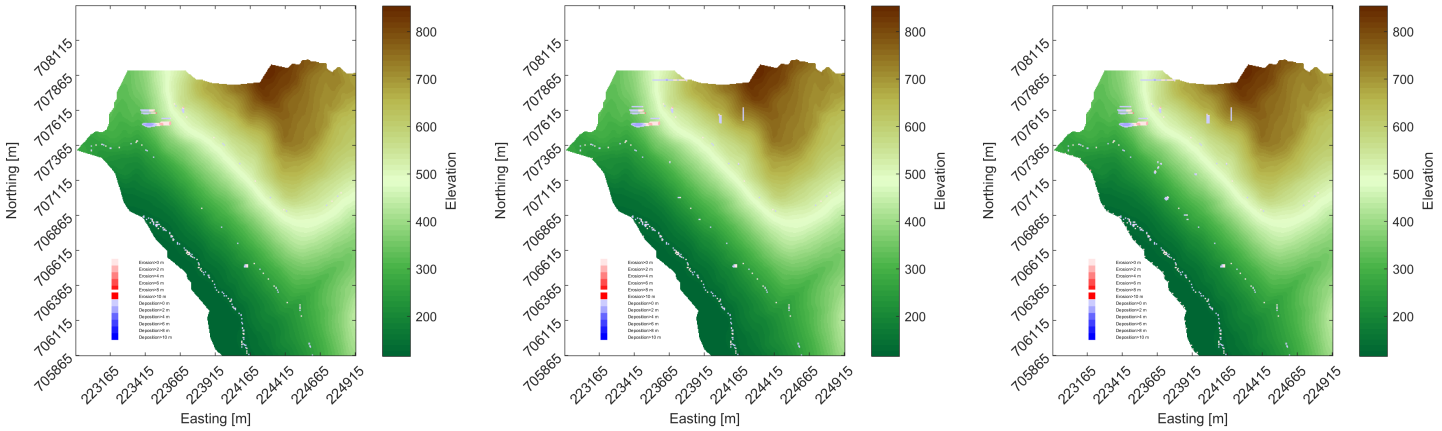

(a) $t = 1$, precipitation = 4.1 mm **(b)** $t = 2$, precipitation = 3.6 mm **(c)** $t = 3$, precipitation = 36.7 mm

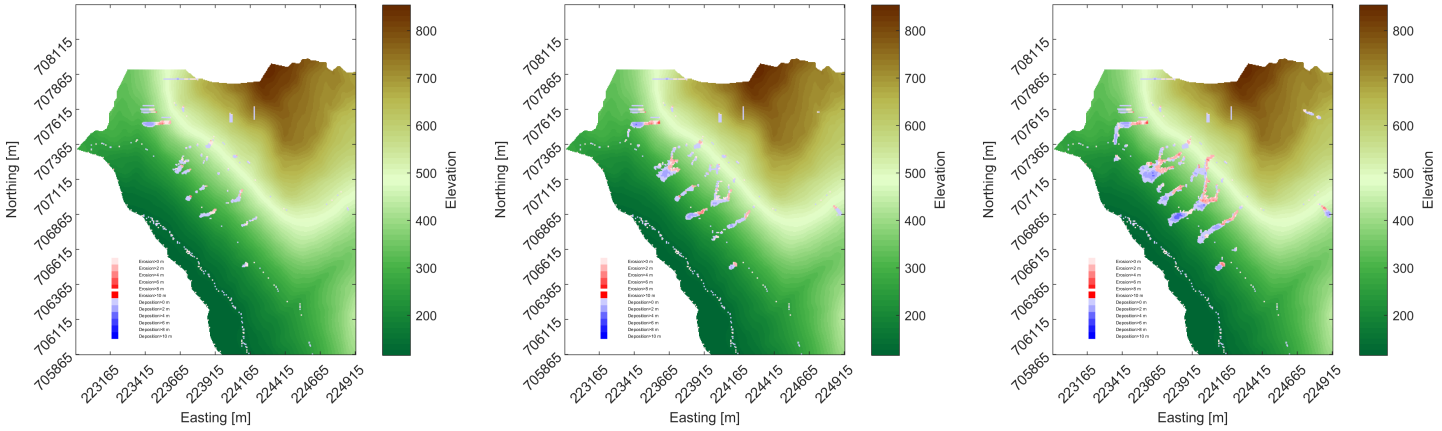

(d) $t = 4$, precipitation = 14.9 mm **(e)** $t = 5$, precipitation = 27.2 mm **(f)** $t = 6$, precipitation = 68.3 mm

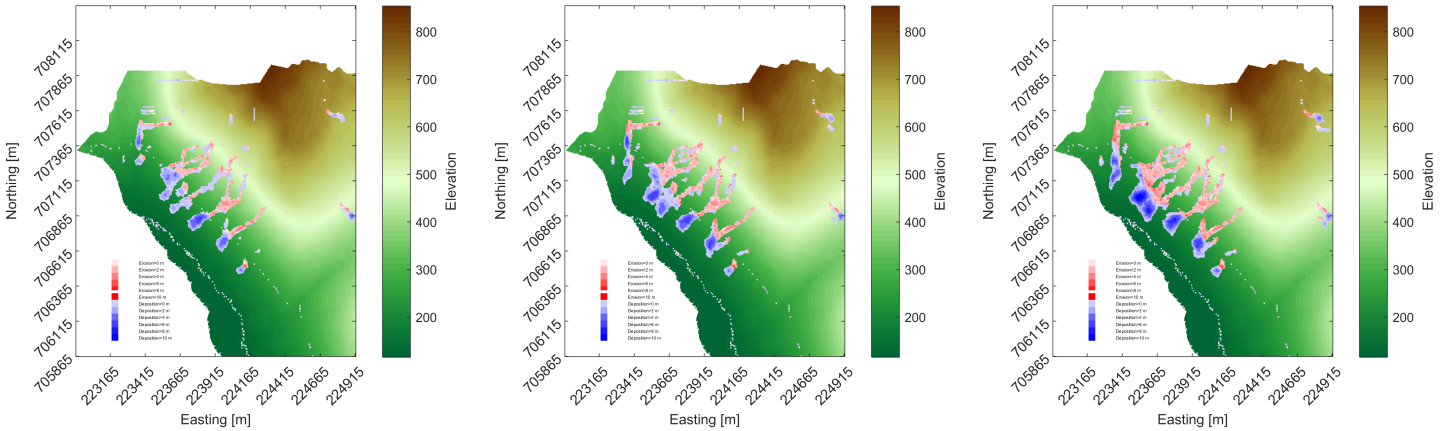

(g) $t = 7$, precipitation = 7.8 mm **(h)** $t = 8$, precipitation = 73.6 mm **(i)** $t = 9$, precipitation = 96.1 mm

Figure 44: Time series for 20-12-2036.

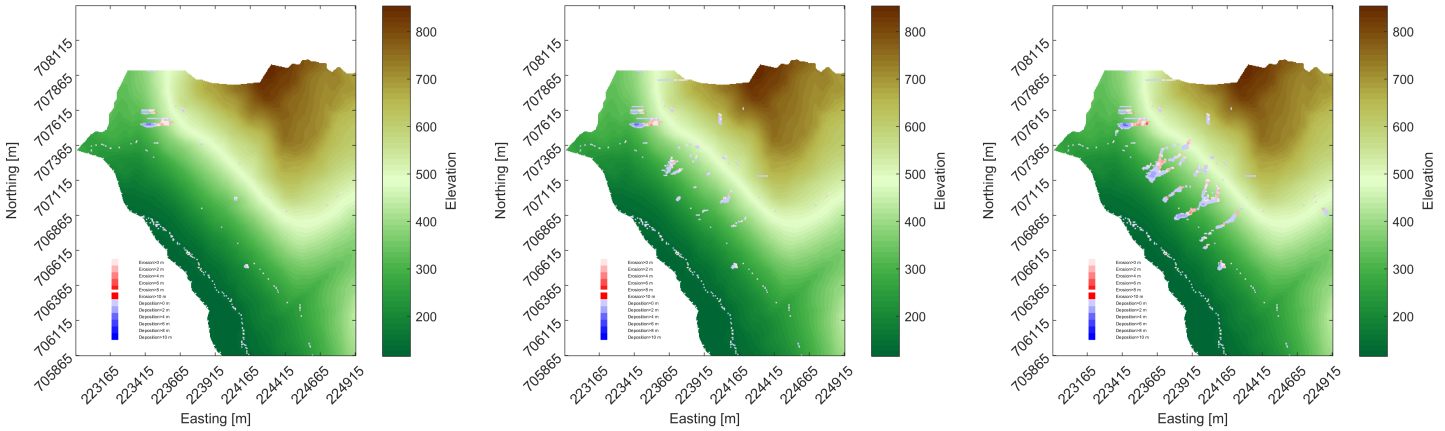

(a) $t = 1$, precipitation = 36.7 mm **(b)** $t = 2$, precipitation = 14.9 mm **(c)** $t = 3$, precipitation = 27.2 mm

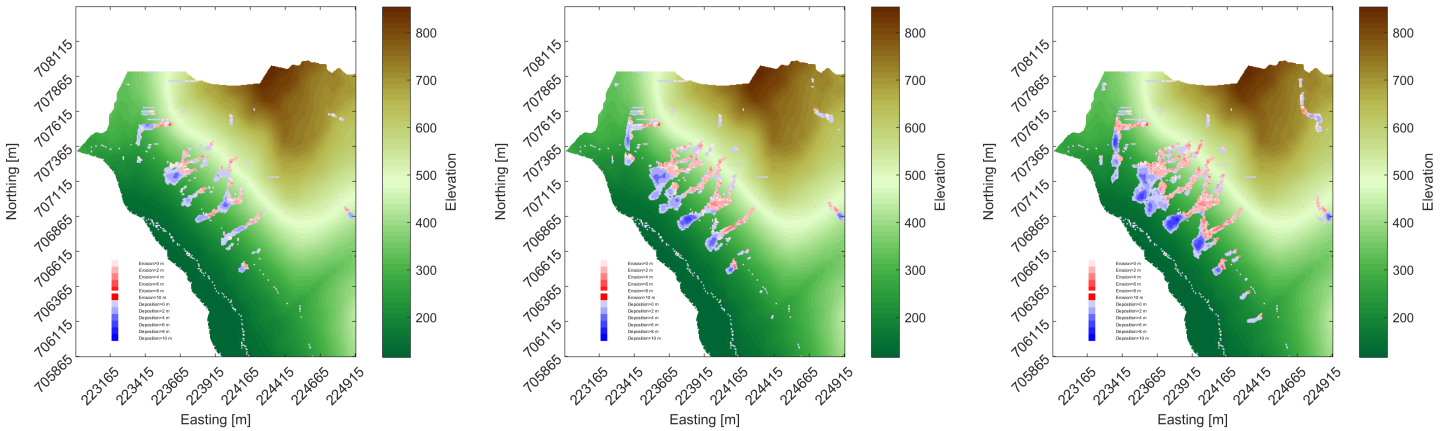

(d) $t = 4$, precipitation = 68.3 mm **(e)** $t = 5$, precipitation = 7.8 mm **(f)** $t = 6$, precipitation = 73.6 mm

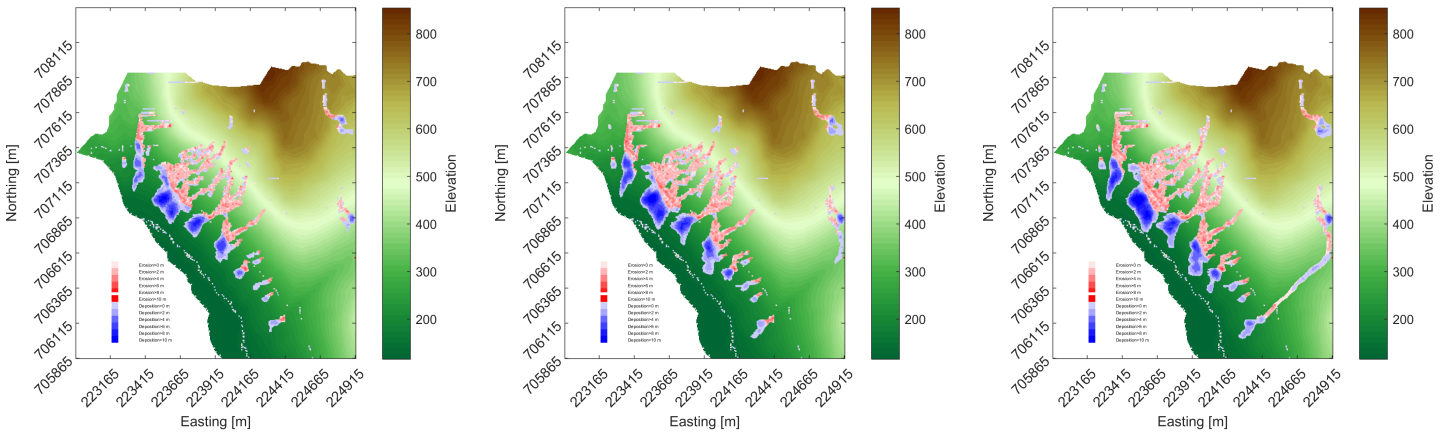

(g) $t = 7$, precipitation = 96.1 mm **(h)** $t = 8$, precipitation = 34.3 mm **(i)** $t = 9$, precipitation = 21.2 mm

Figure 45: Time series for 20-12-2036.

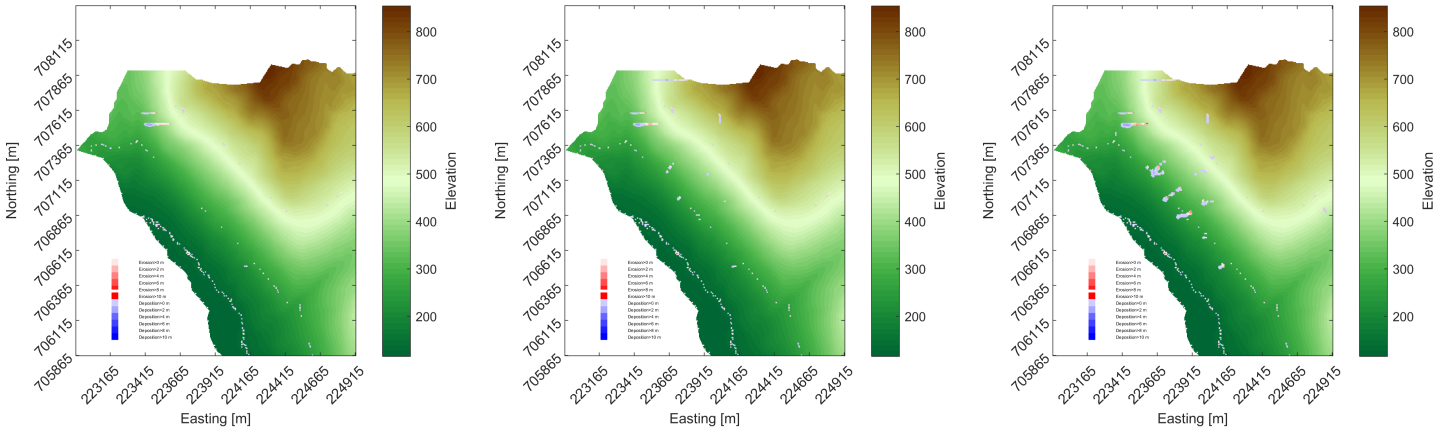

(a) $t = 1$, precipitation = 12.9 mm **(b)** $t = 2$, precipitation = 43.8 mm **(c)** $t = 3$, precipitation = 9.7 mm

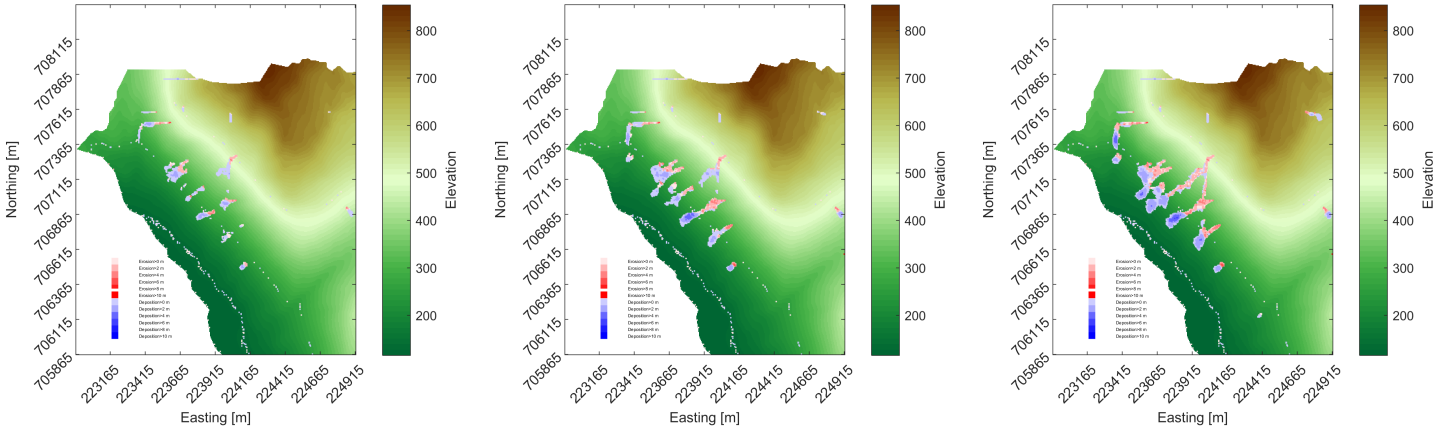

(d) $t = 4$, precipitation = 18.8 mm **(e)** $t = 5$, precipitation = 58.5 mm **(f)** $t = 6$, precipitation = 10.4 mm

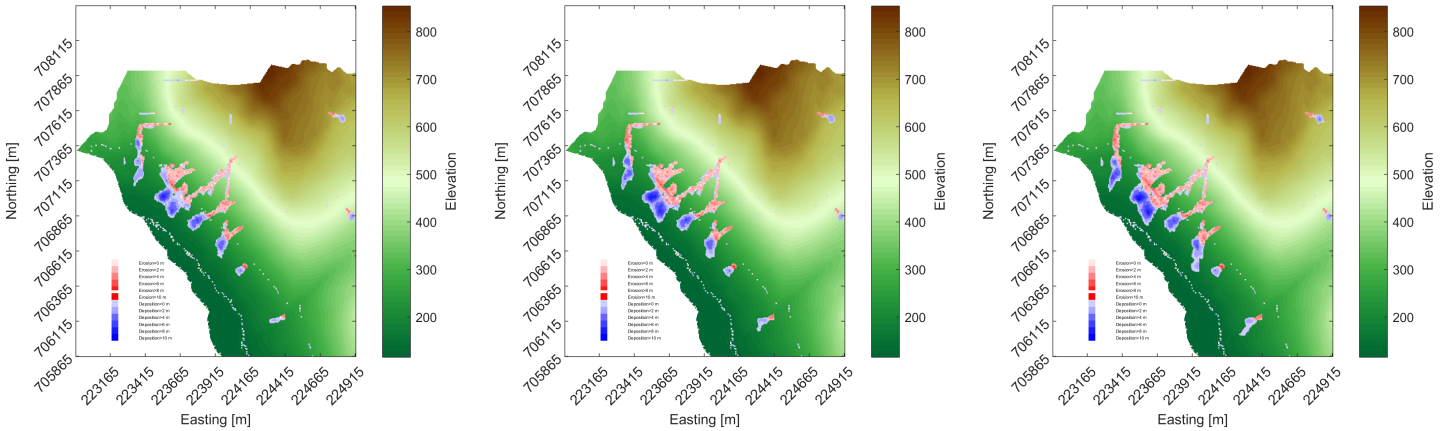

(g) $t = 7$, precipitation = 4.8 mm **(h)** $t = 8$, precipitation = 2.5 mm **(i)** $t = 9$, precipitation = 51.4 mm

Figure 46: Time series for 27-10-2037.

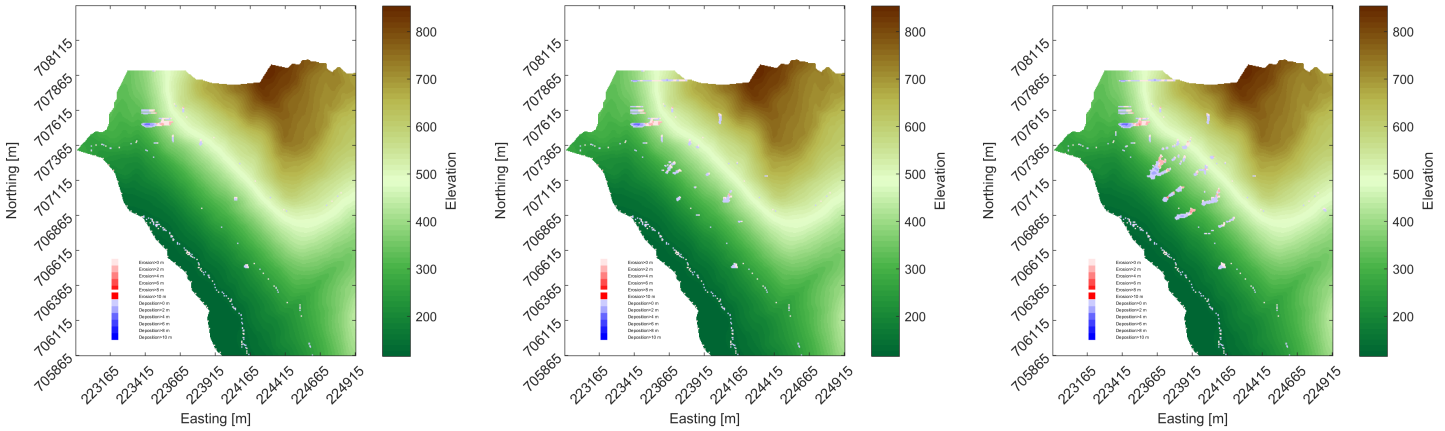

(a) $t = 1$, precipitation = 22.5 mm **(b)** $t = 2$, precipitation = 12.8 mm **(c)** $t = 3$, precipitation = 31.3 mm

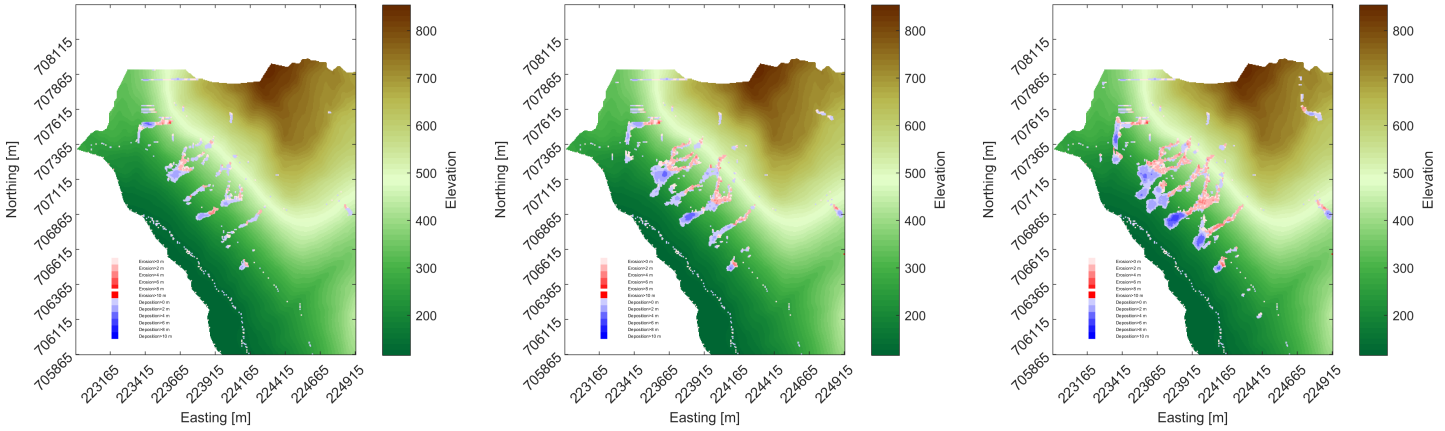

(d) $t = 4$, precipitation = 25.6 mm **(e)** $t = 5$, precipitation = 49.5 mm **(f)** $t = 6$, precipitation = 47.5 mm

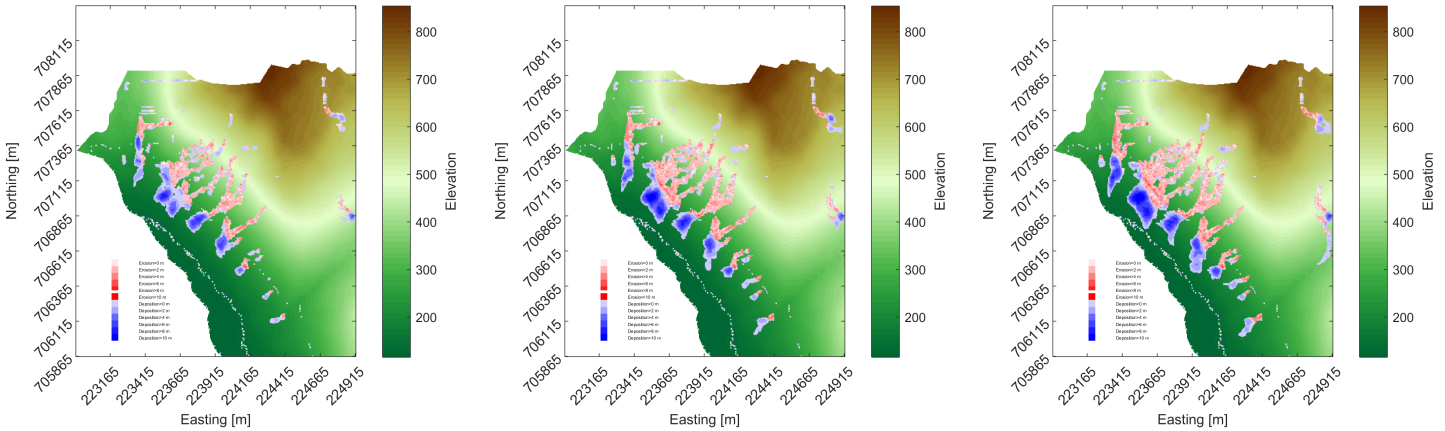

(g) $t = 7$, precipitation = 89.7.2 mm **(h)** $t = 8$, precipitation = 61.8 mm **(i)** $t = 9$, precipitation = 60.5 mm

Figure 47: Time series for 21-10-2038.

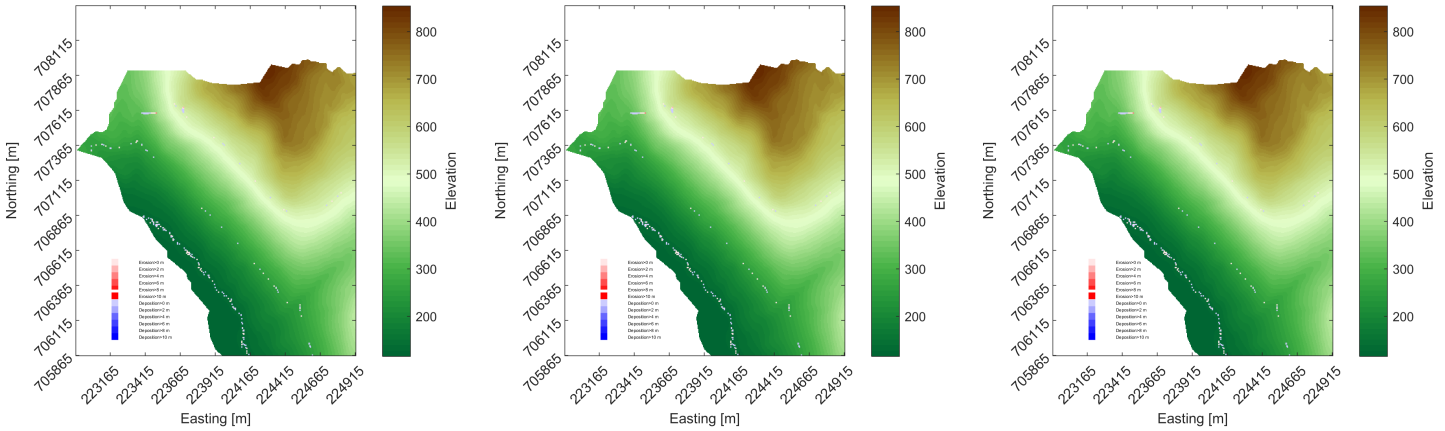

(a) $t = 1$, precipitation = 0.1 mm **(b)** $t = 2$, precipitation = 0.0 mm **(c)** $t = 3$, precipitation = 0.0 mm

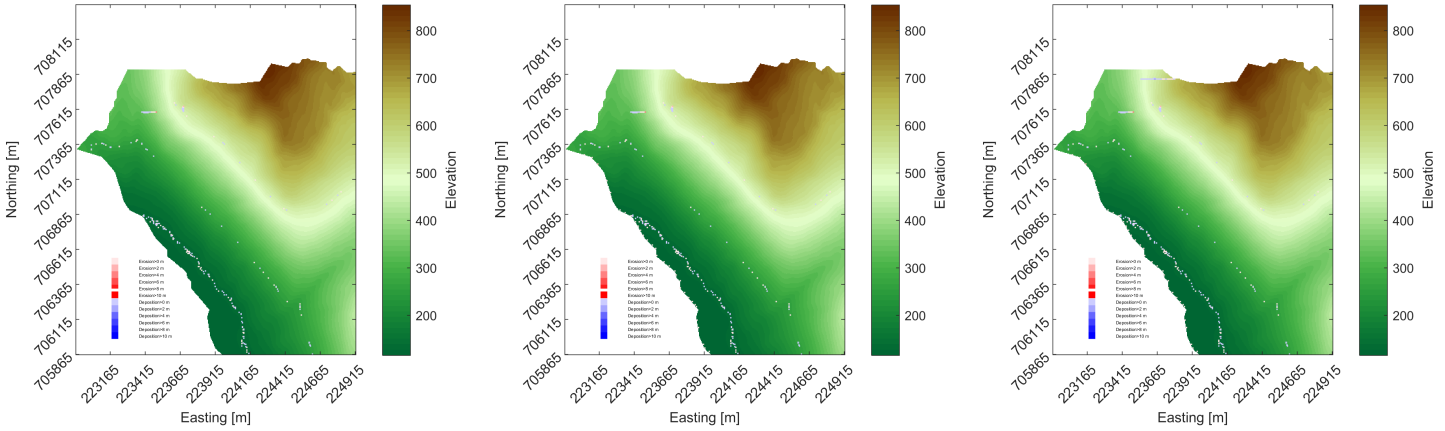

(d) $t = 4$, precipitation = 0.4 mm **(e)** $t = 5$, precipitation = 15.0 mm **(f)** $t = 6$, precipitation = 0.7 mm

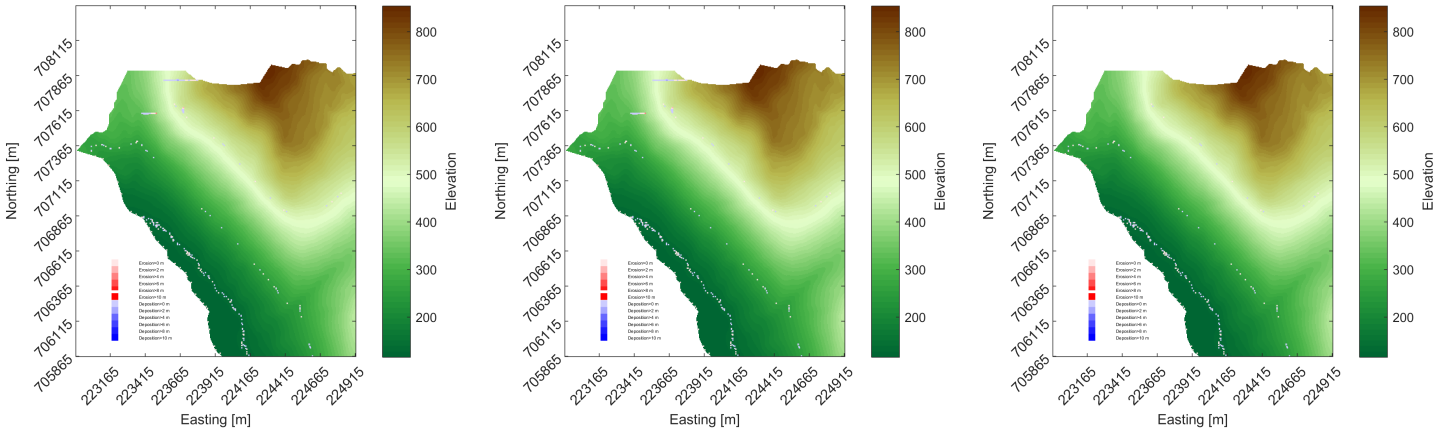

(g) $t = 7$, precipitation = 3.7 mm **(h)** $t = 8$, precipitation = 3.6 mm **(i)** $t = 9$, precipitation = 59.5 mm

Figure 48: Time series for 31-12-2044.

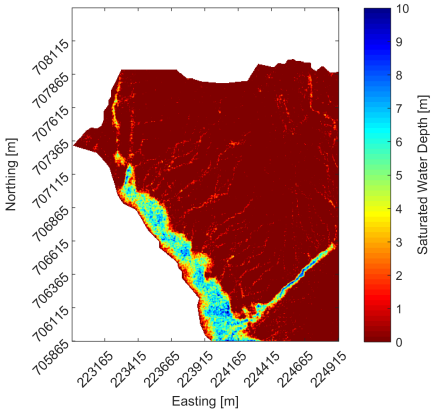

(a) 28-11-2019

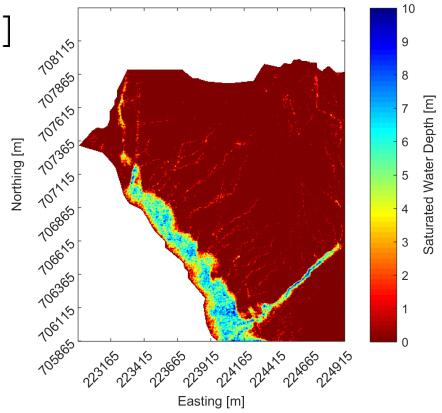

(b) 05-03-2022

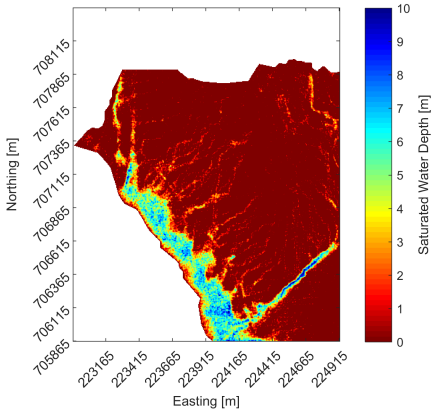

(c) 23-01-2024

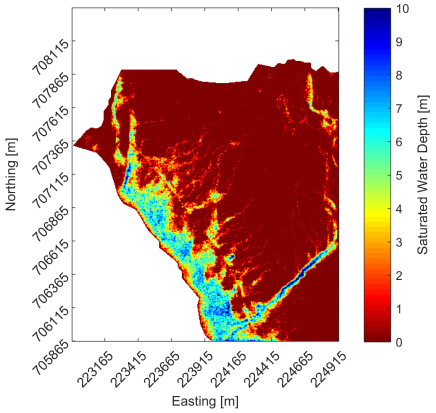

(d) 24-09-2028

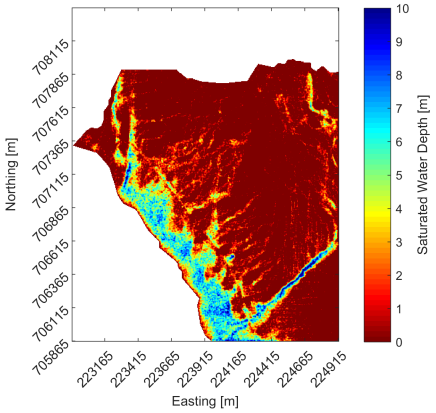

(e) 21-11-2032

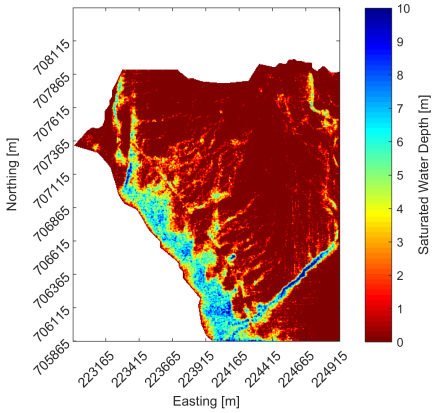

(f) 18-12-2036

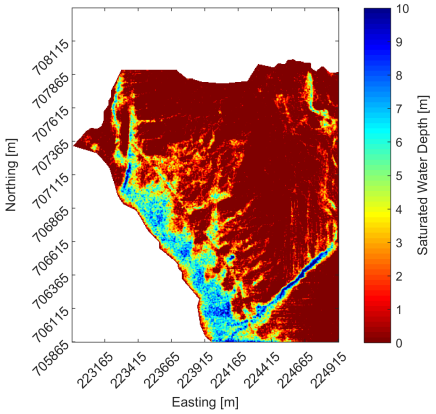

(g) 20-12-2036

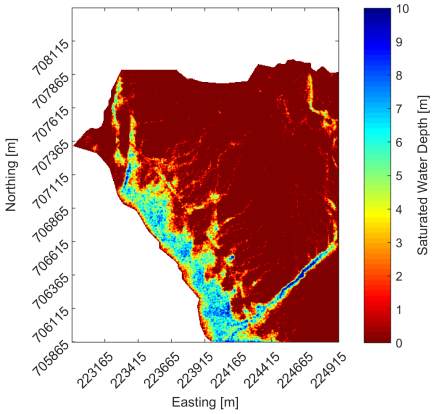

(h) 27-10-2037

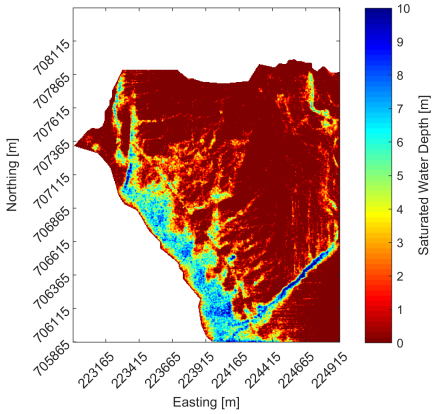

(i) 21-10-2038